Calibration of Heliostats Using a Drone

by

Jurgens Erik Gouws

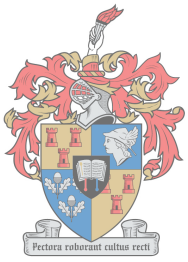

Thesis presented in partial fulfilment of the requirements for the degree of Master of Engineering Mechanical in the Faculty of Engineering at Stellenbosch University

The financial assistance of the National Research Foundation (NRF) towards this research is hereby acknowledged. Opinions expressed and conclusions arrived at, are those of the author and are not necessarily to be attributed to the NRF.

Supervisor: Dr. W.J. Smit

December 2018

Declaration

By submitting this thesis electronically, I declare that the entirety of the work contained therein is my own, original work, that I am the sole author thereof (save to the extent explicitly otherwise stated), that reproduction and publication thereof by Stellenbosch University will not infringe any third party rights and that I have not previously in its entirety or in part submitted it for obtaining any qualification.

Date: December 2018 J.E. Gouws

Plagiarism Declaration

1. Plagiarism is the use of ideas, material and other intellectual property of another's work and to present it as my own.
2. I agree that plagiarism is a punishable offence because it constitutes theft.
3. I also understand that direct translations are plagiarism.
4. Accordingly all quotations and contributions from any source whatsoever (including the internet) have been cited fully. I understand that the reproduction of text without quotation marks (even when the source is cited) is plagiarism.
5. I declare that the work contained in this assignment, except where otherwise stated, is my original work and that I have not previously (in its entirety or in part) submitted it for grading in this module/assignment or another module/assignment.

17637996 Student number	 Signature
J.E. Gouws Initials and surname	26/11/2018 Date

Abstract

The aim of this thesis was to investigate the theoretical feasibility of calibrating heliostats using a drone. Doing so would require the following: (1) First show that it is possible to identify heliostats using a camera. (2) Then prove and test the accuracy of a RTK-GPS. (3) Then assess the target that is used, and prove that it can be identified within the reflection of a heliostat's concave mirror.

The last step is to set up an adjusted calibration equation for the application of using a drone. Due to the number of parameters, a Monte Carlo simulation should be performed using multiple drone inputs to predict the performance of a drone-calibrated heliostat. If the predicted performance of a drone-calibrated heliostat is satisfactory, then it can be claimed that a heliostat could theoretically be calibrated using a drone.

A proof of concept established that it is possible to identify the reflection in the heliostat's concave mirror. It was also shown that it is possible to calculate a weighted average of the reflection, and to identify a feasible point in space for the drone. The RTK-GPS also performed as expected and showed steady results during the tests. Nine parameters were used to describe the mathematical model of the heliostat, and an additional parameter was used to describe the drone offset. The simulation could predict the resulting milliradian error on the target to be less than one milliradian for drone calibration using at least 10 points in space that is further than 32 metres from the pylon.

It was concluded that the resulting milliradian error was dependent on the specific noise in the drone position, combined with the drone position chosen, as well as the drone distance from the pylon.

Uittreksel

Die doel van hierdie tesis is om die teoretiese uitvoerbaarheid van kalibrasie van heliostate met behulp van 'n hommeltuig te ondersoek. Om dit te kan doen sal die volgende vereis word: (1) Toon eers aan dat dit moontlik is om heliostate met behulp van 'n kamera te identifiseer. (2) Bepaal dan die akkuraatheid van 'n RTK-GPS. (3) Beoordeel dan die teiken wat gebruik word, en bewys dat dit geïdentifiseer kan word binne die weerkaatsing van 'n heliostaat se konkawe spieël.

Die laaste stap is om 'n aangepaste kalibrasievergelyking op te stel vir die toepassing van 'n hommeltuig. As gevolg van die aantal parameters, moet 'n Monte Carlo simulasie uitgevoer word met die insette van verskeie drone om die werking van 'n hommeltuig-gekalibreerde heliostaat te voorspel. As die voorspelde werking van 'n hommeltuig-gekalibreerde heliostaat bevredigend is, dan kan daar beweer word dat 'n heliostaat teoreties gekalibreer kan word metbehulp van 'n hommeltuig.

'n Bewys van konsep het vasgestel dat dit moontlik is om die refleksie in die heliostaat se konkawe spieël te identifiseer. Daar is ook getoon dat dit moontlik is om 'n geweegde gemiddelde van die refleksie te bereken, en om 'n bruikbare punt in die ruimte vir die hommeltuig te identifiseer. Die RTK-GPS het na verwagting presteer, en het tydens die toetse konstante resultate getoon. Nege parameters is gebruik om die wiskundige model van die heliostaat te beskryf, en 'n addisionele parameter is gebruik om die hommeltuig-verplasing te beskryf. Die simulasie kan die gevolglike milliradiale fout op die teiken voorspel om minder as een milliradiaal te wees vir hommeltuig-kalibrasie deur minstens 10 punte in die ruimte te gebruik wat verder as 32 meter van die spantoring is.

Daar kan tot die gevolgtrekking gekom word dat die gevolglike milliradiale fout afhanklik was van die spesifieke geraas in die hommeltuig-posisie, gekombineer met die gekose hommeltuig-posisie, asook die hommeltuig se afstand van die spantoring.

Acknowledgements

I would like to thank Dr W.J. Smit for his guidance and assistance during the period of my masters and all the support he has provided. I would also like to use this chance to thank you all my friends for their support and lending an ear to talk to when I was stuck, many times I spoke to them and I figured out what was wrong in my code by just talking about it. Thus to Leon, Antonio and Michen I would like to say a special thank you. I also would like to say thank you to Hein for lending me equipment and his help with the heliostat in the structures lab. I would also like to say a special thank you Kimberley for her motivation during the writing period and the final year of my thesis, your unending support was sincerely appreciated. Then to my mother I would love to say thank you for allowing this opportunity in my life and her support. To my brother I also would like to say it is great to have you by my side, thank you for all the talks and excitement about my masters.

Contents

List of Figures

List of Tables

Nomenclature

Variables

C	Concavity	[deg]
D	Distance	[mm]
d	Day number	[ ]
H_z	Distance from the mirror pivot to the mirror surface center	[mm]
h	Solar hour angle	[deg]
L_P	Pylon length	[mm]
L_T	Relative target y-distance multiplier	[ ]
n	number of points	[ ]
PD	Point down	[mm]
PE	Point east	[mm]
PN	Point north	[mm]
S	Size	[mm]
t^*	Confidence constant	[ ]
s	Slack variable	[ ]
W	Width	[mm]
z	Zoom on target	[mm]
α	Elevation	[deg]
γ	Azimuth	[deg]
δ	Solar declination angle	[deg]
ϵ_α	Elevation angle bias	[deg]
ϵ_γ	Azimuth angle bias	[deg]
η	Standard deviation of a sample	[ ]
θ	Normal incident angle	[deg]
ζ	Mechanical arm length	[mm]
ζ_a	Mechanical arm angle	[deg]
ζ_r	Mechanical arm radius	[mm]
θ	Angle between concave mirror tip and target tip	[deg]
μ_N	Tilt around Northern axis	[deg]

μ_E	Tilt around Eastern axis	[deg]
σ	Angle between camera and concave mirror tip	[deg]
τ	Incident angle for mirror-pivot offset	[deg]
τ_1	Dual-axis non-orthogonal angle	[deg]
ψ	Local latitude	[deg]
ω	Angle between camera and normal of concave mirror tip	[deg]

Vectors

$\underline{a}$	Normal projected vector
$\underline{b}$	Plane projected vector
$\underline{h}$	Heliostat vector
$\underline{n}$	Normal mirror vector
$\underline{R}$	Reflected vector
$\underline{s}$	Solar vector
$\underline{T}$	Target vector
$\underline{\delta}$	Displacement vector
$\underline{\upsilon}$	Variation vector
$\underline{\psi}$	Pylon shift vector

Matrices

$\mathbf{H}$	Householder matrix
$\mathbf{I}$	Identity matrix
$\mathbf{P}$	Projection matrix
$\mathbf{R}_E$	Rotational matrix around Eastern axis
$\mathbf{R}_N$	Rotational matrix around Northern axis
$\mathbf{\Phi}$	Final rotational matrix

Superscripts

T	Transposed
$'$	Adjusted
$*$	Estimated

Subscripts

E	East
i	Entry number
N	North
n	normal

o	Origin
s	Solar
t	Target
x	x-direction
y	y-direction
z	z-direction
1	One
2	Two
3	Three

Abbreviations

BCS	Beam characterisation system
CAD	Computer-aided design
CSP	Concentrated solar power
DGPS	Differential Global Positioning Systems
DRMS	Distance root mean square
EoT	Equation of time
GMT	Greenwich mean time
GNSS	Global Navigation Satellite System
GPS	Global positioning system
IMU	Inertial measurement unit
LED	Light-emitting diode
LFR	Linear Fresnel reflectors
LONG	Longitude
LST	Local solar time
LSTM	Local standard time meridian
LT	Local time
MRSE	Mean radial spherical error
PTC	Parabolic trough collectors
PVC	Polyvinyl chloride
RTK	Real-time kinematic
SPD	Solar parabolic dishes
SPT	Solar power tower
STDev	Standard deviation
TC	Time correction factor
2D	Two-dimensional
3D	Three-dimensional

Chapter 1

Introduction

The development of novel technologies to improve the concentration, utilisation, and storage of solar energy has been emphasised for the advancement of sustainable energy in recent years. Concentrated solar power (CSP) is one of the renewable energy industries that has drawn the attention of many research development programmes. (Singh, Hussien, Al-Ansari, Saoud and McKay, 2018)

1.1 Background

CSP has significant potential to ensure the provision of the ever-growing demand for power. These solar power plants use focused sunlight to heat up fluids. There are many different technologies used to focus sunlight as seen in Figure 1.1, such as solar parabolic dishes (SPD) or linear Fresnel reflectors (LFR). Each method utilises a different strategy for collecting solar energy. Some technologies such as the parabolic trough collectors (PTC) focuses the sunlight onto a linear tube, while solar power tower (SPT) systems use tracking mirrors, called heliostats, to reflect sunlight onto a central receiver located on a tower. The concentrated thermal energy is then used to produce steam to drive conventional turbines that generate electricity by using a typical steam Rankine cycle, or other similar methods.

Solar power tower systems can be more efficient than parabolic trough systems, although parabolic trough technology is currently more commonly used. The reason for this is that SPT technology is relatively new, according to Ravelli, Franchini and Perdichizzi (2018). Although SPT have a higher cost per unit area they can reach higher temperatures that makes them perform more efficiently than a PTC systems. Therefore SPT requires a lower aperture area as well as lower investment costs to generate the same amount of power due to the total field size required. (Ravelli *et al.*, 2018)

(a) Solar parabolic-dish (SPD) (Maricopa solar, 2018)

(b) Linear Fresnel reflectors (LFR) (FLT, 2018)

(c) Parabolic trough collectors (PTC) (Llamas, 2018)

(d) Solar power tower (SPT) (Richter, Frank and Abrahám, 2014)

Figure 1.1: Four concentrated solar power (CSP) technologies

Any new, or currently running, CSP plant using central receiver technologies involves high costs. An example of the cost distribution for a SPT system can be seen in Figure 1.2. Researchers have investigated each component of the heliostats and the central receiver in order to try and reduce the high initial costs per unit area. The reason they focus so much on the heliostat is that there are sometimes thousands of heliostats on a single plant contributing to the biggest percentage of the total cost. Therefore, saving some costs on the design or implementation of one heliostat ends up saving thousands on the whole plant. (CSP Summary Charts, 2018)

1.2 The specific dilemma

Many researchers have improved the efficiency of plants by tightening the design tolerances of the concave mirrors and the control system. This would certainly increase the initial cost of implementing a new CSP plant, but would ensure a higher efficiency of the plant. Most likely the current implemented SPT systems do not require frequent calibration since performance parts was

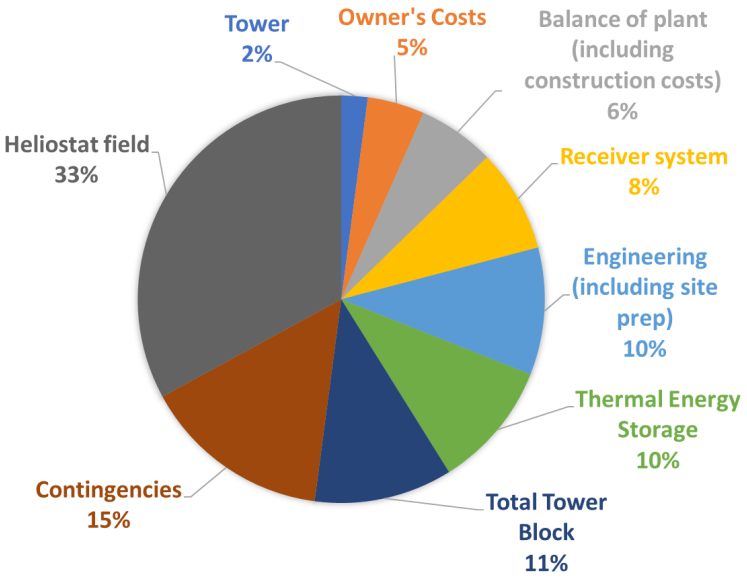

Figure 1.2: An indication of the cost breakdown for a solar power tower in South Africa with 15 hours of storage in 2014. Adapted from CSP Summary Charts (2018)

used. However any system would benefit from frequent calibration and thus improve the efficiency of the field.

On the other hand, future plants could reduce their costs by relaxing the design tolerances during manufacturing and building in order to reduce initial costs. As a result of equipment of a lower quality, each heliostat requires regular calibration to improve the efficiency again.

Unfortunately, calibration cannot be only done once, and then be expected to perform throughout the year with only minor increases in errors, but calibration has to be done regularly to every single heliostat. For a small-scale heliostat plant this might be possible, but in such a plant every heliostat contributes to the total heat energy generated, and the aim of the heliostat should not be removed from the heat collector for too long in order to calibrate it. However, in larger heliostat plants removing several heliostats from the heat collector in order to calibrate them on the target would not influence the total heat energy generated. But these plants could have thousands of heliostats that require calibration that can possibly take months to calibrate all the heliostats. The calibration process will start with one and after some time, then the first heliostat will not be performing perfectly anymore. Thus an endless cycle of calibration takes place.

One calibration point is created when the sun at coordinates (S_x, S_y, S_z) reflects from a heliostat with a known fixed origin towards a target. When the

sun's reflection is deemed to be on the centre of the target, then the resulting elevation and azimuth (α, γ) angles used for the specific heliostat are stored with the current position of the sun. The locations and angles can be seen in the representation in Figure 1.3. This procedure would be done multiple times to obtain a sufficient number of data points in order to estimate all of the parameters of a mathematical representation of the heliostat. When all the parameters of the heliostat are estimated, then that heliostat would be calibrated. Due to the fact that these calibration points are generated with the help of the sun means that one has to wait for the sun to move to a new position before a new set of calibration points can be collected.

This means that the time it takes to calibrate one heliostat is too long, and calibrating a whole field could potentially take months. It is also very difficult to calibrate more than one heliostat at a time due to the complexity of identifying the separate reflections of each heliostat. Over time the accuracy of a heliostat decreases, and this leads to the plant producing less power. Any plant that does not have all its heliostats calibrated at the same time would be running inefficiently.

Therefore, if it is possible to decrease the calibration time, then it is also

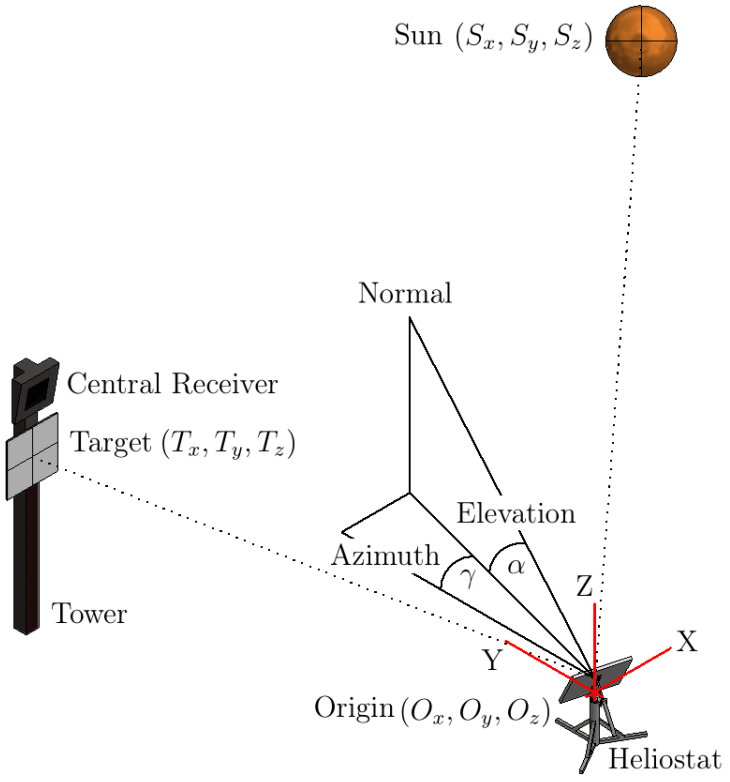

Figure 1.3: Representation of calibration for heliostats

possible to increase the efficiency of the plant significantly, due to more heliostats being accurately calibrated at the same time. This is beneficial to both current and future SPT plants. Even more important if calibration time is decreased then the requirement for tight design tolerances would not be needed as calibration can be implemented on a regular basis. This would drastically reduce initial costs of SPT systems for the future making way for low cost, frequently calibrated SPT plants.

1.3 Why this is still unresolved

Following the number of SPT technology-related patents and papers, as seen in Figure 1.4, it is clear that in the in the past decade many researchers at universities and other major research institutions have attempted to analyse and improve on the efficiency of SPT technology. Since the year 2000, 359 number of papers have been published, and 18 number of patents have been registered in the field of solar power tower. More specifically, on the topic of heliostat counting, the numbers are as follows: 502 papers have been published, and 92 patents have been registered.

One of these researchers, Zavodny, Slack, Huibregtse and Sonn (2015), has attempted to speed up the calibration process of the heliostats by using tower-based artificial light calibration systems that uses cameras and targets lit up by LEDs. This concept involves multiple towers with targets placed on each tower. Each tower also has a camera looking down on the field of heliostats. During the night these heliostats are aimed in such a way that it reflects an LED target from one tower to one of the cameras of the towers. As there are fixed known locations for the cameras, the image of the field can be used to create a calibration point. When the number of towers and variations of re-

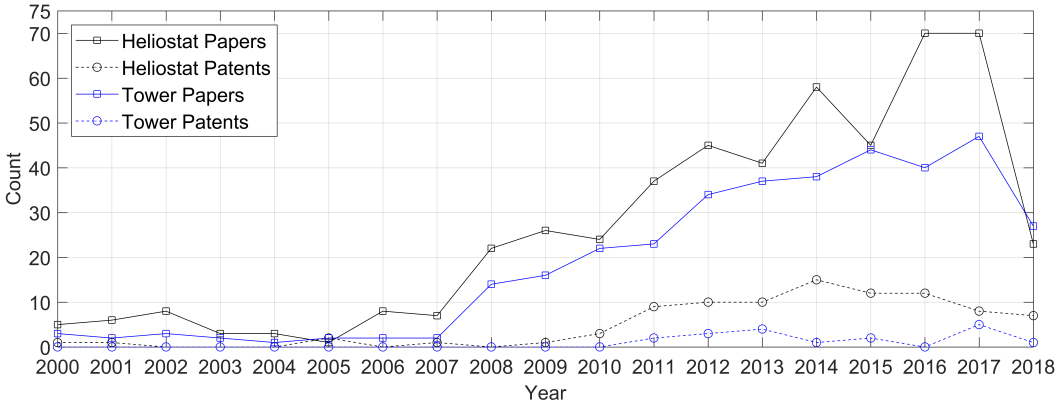

Figure 1.4: Number of CSP technology-related patents and papers retrieved from the Google Scholar database with the search term "Heliostat" or "Solar Power Tower" in the title.

flecting targets onto different cameras are combined, then enough calibration points can be set up to calibrate the heliostats with a resulting pointing error of less than 1.5 milliradians. Added benefits to the system were the rapid detection of broken or misaligned heliostats. The downfall of this proposed solution is not only the cost of implementing multiple towers on a built system, but also the shadows that will be created on the field from the new towers.

Other general solutions to the calibration process focused on adding multiple targets on the tower. Most of these systems are automated to calibrate one heliostat at a time. Other researchers, for example Andreas *et al.* (2013), have also used drones to detect defects of heliostat surfaces by using deflectometry. Drone applications have already been patented in the field of CSP such as cleaning the heliostats mirrors to improve the efficiency of the field. This was done by Pardell (2017).

1.4 The possible solution

The use of drone technology is on the increase (Newman, 2016). So what are the strengths of this technology? The application of drones to calibrate heliostats has not yet been explored. If it is possible to use a drone to calibrate heliostats, then the calibration process would speed up and thus increase the efficiency of a CSP plant. The limitations of using a drone lie in the uncertainty of its exact position, and how one would acquire a correct calibration point.

The idea is to use a quadcopter drone as seen in Figure 1.5. To solve the uncertainty of the position of the drone, a real-time kinematic global positioning system (RTK-GPS) could be used. Furthermore, identifying a target in the reflections of a heliostat would implement the same solution as Zavodny *et al.* (2015), and implement a camera.

1.5 The aim

The aim is to investigate the theoretical feasibility of calibrating heliostats with drones. The last step is to set up an adjusted calibration equation for the application of using a drone. The appropriate heliostat parameters should be selected to represent a physical model. The high accuracy of the sun's positions could be used to verify the accuracy of the simulation code. Due to the number of parameters, a Monte Carlo simulation should be performed with multiple drone inputs to predict the performance of a drone-calibrated heliostat. If the predicted performance of a drone- calibrated heliostat is satisfactory, then it can be claimed that a heliostat could theoretically be calibrated using a drone.

Figure 1.5: Drone at the Helio100 field

To do so the following prerequisites must be achieved:

- First show that it is possible to identify heliostats with a camera.
- Then prove and test the accuracy of a RTK-GPS.
- Then assess the target that is used, and prove that it can be identified within the reflection of a heliostat's concave mirror.

If these conditions are met then it can be assumed that a theoretical calibration point could be obtained.

Chapter 2

Literature review

2.1 Drone technology

There is a wide variety of types of drones. The military has long-range surveillance drones that are categorised as UAVs, and these are mostly controlled via a computer system and a pilot that are located at a control station. Then there are the commercial drones, which can range from as small as palm-sized to the size of a human body: these are mostly controlled via mobile phones or tablets. (Floreano and Wood, 2015)

Then there are drones specifically designed for hobbyists. These drones include racing drones which are controlled using a controller and a receiver on the drone. They are designed to be fast and mobile, but they cannot carry excessive weight other than their own framework, their flight-controller, and battery. (Floreano and Wood, 2015)

Finally, there is the custom market of drones that offer functionality which the commercial and racing drones might not have. These drones have the ability to carry additional weight, and can also be controlled from a ground station. This type of drone will be used for this project as it can be controlled from a ground station while carrying weight, in this case, a camera. (Floreano and Wood, 2015)

Drones are a relatively new type of technology, and therefore its possibilities are not yet fully explored. Daily people find new and innovative ways of using drones for numerous applications. This project aims to prove the usefulness and effectiveness of using drones for a new application.(Floreano and Wood, 2015)

There are two quantifiable accuracies when it comes to drones. One is the control accuracy and the other is measurement accuracy. Control accuracy

refers to how efficiently the drone responds to movement commands, or to commands to be stationary. The drone makes use of an on-board control system, 3DR Pixhawk (flight controller), to take all the readings from the sensors and to use that as feedback for the control accuracy. Measurement accuracy refers to how well the current position is known for the drone. For the purpose of this thesis the positional accuracy is of greater importance than the control accuracy, and will therefore be the main focus. The equipment used to log or estimate a drone's position is a GPS, of which there are many variations with different levels of accuracy.

2.2 Real-time kinematic global positioning system

The navigation system is one of the key components of a drone. This system is built using an inertial measurement unit (IMU) and a Global Navigation Satellite System (GNSS) receiver. Position error is always present when using a GNSS receiver. To minimise the position error in the GNSS solution in order to attain a high level of precision and accuracy requires specialised systems. One such system is a real-time kinematic (RTK) solution. Real-time kinematic global positioning systems (RTK-GPS) are a subset of Differential Global Positioning Systems (DGPS). The system pushes error corrections from a base station to a rover station instead of statically producing position outputs as seen in Figure 2.1. This method provides centimetre-level real-time accurate positioning relative to a base station.

According to McCollum (2017), the error sources that are attributed to GPS systems' positional inaccuracies can be grouped using the following criteria:

- Ephemeris data - The GPS message does not transmit to the correct satellite location. This error increases over time.
- Satellite clock - GPS satellites have extremely accurate atomic clocks, but clock drifts are inevitable and small errors cause significant errors in the receiver on the ground. The error is in the range of 100 metres.
- Ionosphere - The modulation of signal delay is proportional to the number of free electrons in the ionosphere due to the GPS signals not travelling at the vacuum speed of light. The error is in the range of 10 metres.
- Troposphere - The speed of light of radio waves is influenced by the variations in temperature, humidity and pressure. The error is in the range of 1 metre.
- Multipath - Reflected signals from reflection surfaces entering the antenna of the receiver. The error is in the range of 0.5 metres.

- Receiver - Software accuracy, thermal noise and biases between receiver channels can cause errors.

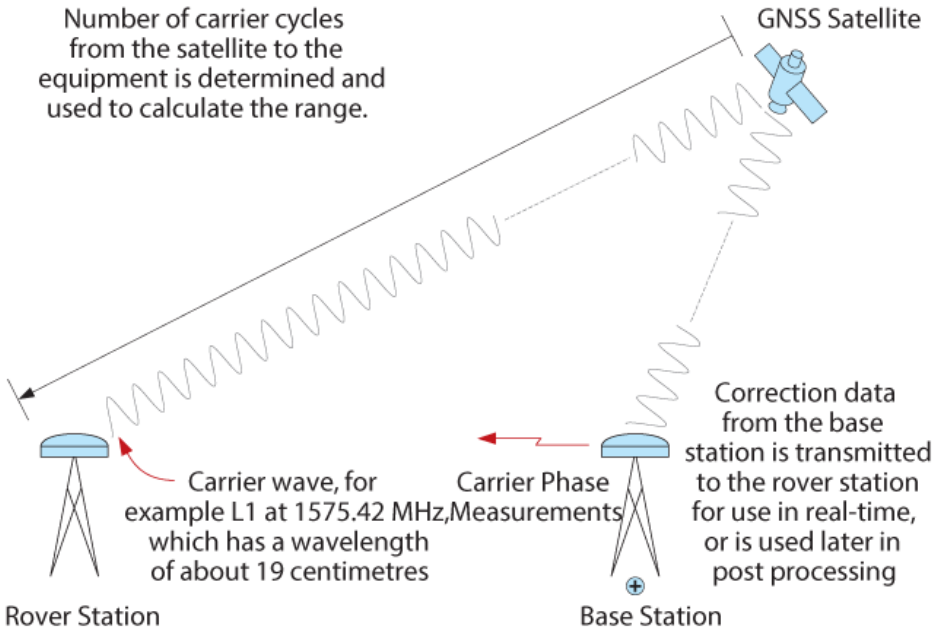

Figure 2.1: Illistation of RTK-GPS setup (Real-Time Kinematic (RTK), 2018). A GNSS satellite communicating with both the rover and base stations, and the base stations sending corrections to the rover station.

One of the RTK-GPS systems that is commercially available for the hobbyist is Swift Navigation's Piksi. This device consists of a ground station as well as another antenna and receiver on the drone itself. The ground station picks up between 8 and 16 satellites (the same as the drone's GPS), but because the ground station is at a stationary point during the flight, the ground station is more accurate. Furthermore, the ground station also communicates with the drone's GPS and calculates their relative position to each other. The ground station requires approximately 10 min before the system is accurate in determining the correlation between the ground and the drone, and only thereafter does the system go into a floating-point mode. Knowing relative distances, the RTK-GPS could confirm the drone's position accurately to within 3 centimetres during floating point mode.

2.3 Drone control mechanics

Drones have 4 actuators that are used to rotate and turn. On a drone that uses four motors, one pair of the motors turns clockwise, and the other pair turns anti-clockwise. When one pair increases thrust and the other pair decreases

thrust, it effectively rotates the drone while it holds its current position. This is a very useful ability in a drone when it is being used for photography. A drone also moves in a specific direction by leaning in that particular direction seen in Figure 2.2. When a fixed camera mount is used with the drone it will influence where that camera is aimed. However, influence of the drone's movements on the aim of the camera can be solved by using gimbals. These devices are used to stabilise equipment that is attached to it, such as a camera when its mounting point (the drone) is not fixed relative to some other fixed coordinate system such as the person flying it from the ground. Gimbals can change the direction and aim of a camera with ease during the flight to aim it at a target while the drone is moving in all directions or rotating in any axis.

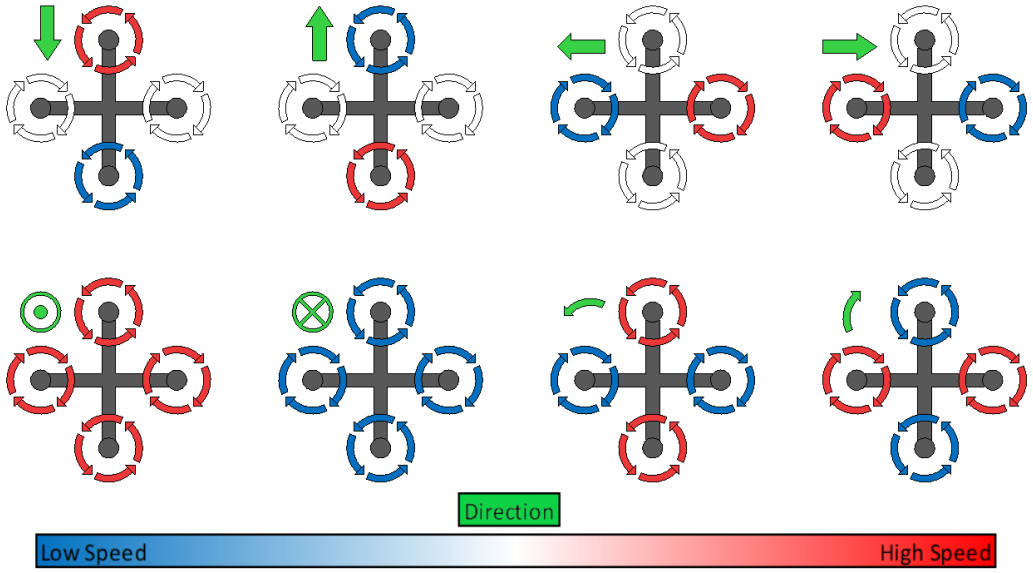

Figure 2.2: Drone direction indication for + configuration, adapted from Gheorghiţă, Vîntu, Mirea and Brăescu (2015). This representation shows the direction of each blade's rotation as well as the speed at which it is rotating. The speed required of each propeller is illustrated with the corresponding colour to move the drone in a direction or rotation as indicated at the top left of each drone.

2.4 Computer vision

The way the world is interpreted by a computer by means of cameras is generally described by the term 'computer vision'. This concept involves the way images are described in computer language. An image is stored in a 3-level deep matrix format where each specific row and column entry represents the colour intensity of a specific pixel. These entries have a maximum value of 255 and a minimum value of 0. Each level represents a specific colour's intensity

- first red, then green, and then blue. By using these properties of images each picture can be used to identify objects by searching for a change in colour intensity. (Sonka, Hlavac and Boyle, 2014)

It should also be noted that to create a black pixel the intensities of all 3 colour bands should be 0. And to create a pure white pixel, all three these colour bands should have an intensity of 255. For example, when taking a picture of the blue sky with bright white clouds, if you isolate the blue colour band, the whole blue image would be about the same intensity, and you would not be able to distinguish between the cloud and the sky. However, when the red band is isolated, then only the white clouds would be identified in the image, while the blue sky would be replaced with close to 0 red intensity.

Programmes such as Matlab have built-in computer vision toolboxes that have the ability to identify blobs, corners, and edges. These can also change the intensity of the image or threshold of a certain colour's ranges. Combining these functions can help identify a complex object using a camera. Thresholding describes the identification of the intensities of a grey -scale image, and then converts it into a black-and-white image, or multi-coloured ranges. The creation of this black-and-white image is done by selecting the intensity value that separates light grey from dark grey, or by manually selecting an intensity threshold. Then all values above that threshold are turned to the maximum value of 255, and everything below is turned to an intensity of 0.

Videos are in fact consecutive images being refreshed at a specific frame per second. The same functionality can be used with videos when a specific frame is selected. This frame also has a specific time-stamp connected to it.

2.5 Calculation sun position

Researchers and scientists have been creating algorithms to calculate the position of the sun from as early as 1969 by Cooper. Table 2.1 displays the improvements made over the years by other authors with their corresponding uncertainty of their algorithm. This has been improved over time, and now, the most accurate algorithm is the Solar Position Algorithm by Reda and Andreas (2004). This algorithm has a maximum tracking uncertainty of +-0.0003 degrees from 2000 BC to 6000 AD. For the purpose of this research, this algorithm will be used to calculate the position of the sun.

Table 2.1: Improvement of solar position algorithms over the years

Author(s)	Year	Algorithm Uncertainty (degree)
Spencer	1971	0.25
Pitman and Vant-Hull	1979	0.02
Walraven	1979	0.013
Michalsky	1988	0.011
Blanco-Muriel et al.	2001	0.008
Grena	2007	0.0027
Reda and Andreas	2008	0.0003

For demonstration purposes the solar position algorithm of Rizvi, Addoweesh, El-Leathy and Al-Ansary (2014) will be followed.

Local Standard Time Meridian (LSTM) calculated using the Local Time (LT) and the Greenwich mean time (GMT):

$$LSTM = 15|LT - GMT| \tag{2.1}$$

Equation of Time (EoT) gives the difference between clock time and local solar time where the d represents the day number:

$$B = \frac{360(d-81)}{365} \tag{2.2}$$

$$EOT = 9.87\sin(2B) - 7.52\cos(B) - 1.5\sin(B) \tag{2.3}$$

Time Correction Factor (TC) calculated using the longitude (LONG) and local standard time meridian (LSTM):

$$TC = 4(LONG - LSTM) + EOT \tag{2.4}$$

Local Solar Time (LST):

$$LST = LT + \frac{TC}{60} \tag{2.5}$$

Solar Hour Angle, h:

$$h = 15^0(LST - 12) \tag{2.6}$$

Solar Declination Angle, δ:

$$\delta = 23.45\sin\left(\frac{360(d-81)}{365}\right) \tag{2.7}$$

Solar Elevation Angle, α_s, calculated with the local latitude, ψ:

$$\alpha_s = \arcsin(\sin(\delta)\sin(\psi) + \cos(\delta)\cos(\psi)\cos(h)) \tag{2.8}$$

Solar Azimuth Angle, γ_s:

$$\gamma_s = \arccos\left(\frac{\sin(\delta)\cos(\psi) + \cos(\delta)\sin(\psi)\cos(h)}{\cos(\alpha_s)}\right) \tag{2.9}$$

2.6 Concentrated solar power plants

Mankind has grown more aware of the effects that they have on the eco-system, and have therefore, during the last decade started concentrating to increase the use of renewable energy. This includes using the wind, water, air and sun as a source of energy. This project considers the sun as a renewable source of energy and focuses specifically on concentrated solar power as the method of obtaining energy.

CSP uses a more indirect method by converting the sunlight into thermal energy by means of focusing the sunlight, and then harvesting that energy using more conventional methods.

Heliostats are one of the methods used to generate thermal energy by reflecting the sun onto a focus point on a central receiver tower. This increases the heat that can then be used within an electrical generating cycle.

In Figure 2.3 the heliostats can be identified as marked 1. The purpose of the heliostats is to reflect sunlight towards the receiver located at the tower, marked 3. The cold tank, marked 2, contains molten salts at 290^0C. This is pumped towards the receiver, marked 3. The purpose of the tower is to absorb the heat from the sunlight to heat the salts to temperatures around 565^0C before it is sent to the hot tank, marked 4. The hot tank keeps the energy accumulated in the form of high temperature liquid salt for later or current demand of heat energy. A steam generator, marked 5, uses the molten salt to heat up water for the steam-generation system. The cooled molten salt is then returned for reuse to the cold tank, marked 2. The heated water turns into high pressure steam that rotates the turbine, marked 6. The turbine in turns powers the electrical generator, marked 7, to generate electrical energy. The final stage uses an electrical transformer, marked 8, to inject the electricity into a distribution grid.

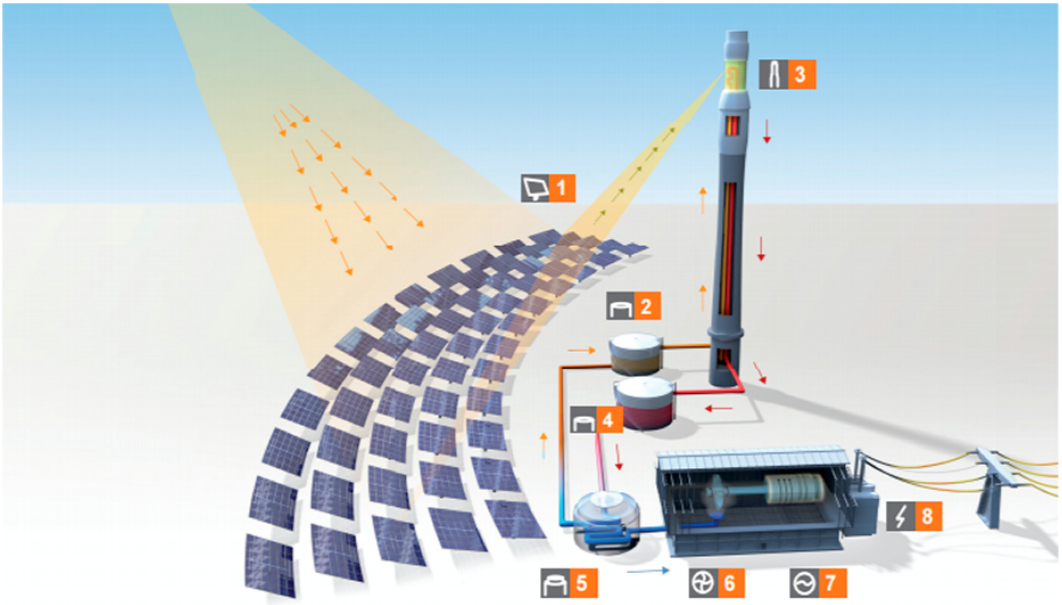

Figure 2.3: Illustration of a solar power tower system with all the indicated steps to generate power (Central Tower Technology, 2018).

2.7 Heliostats

A heliostat is a device that tracks the position of the sun and reflects it towards a target by means of a concave mirror. A facet is the combination of a concave mirror and frame. The concaveness of the mirror is formed during the manufacturing process, and the frame is used to connect the mirror to the pylon. The pylon is normally inserted into a foundation. With the help of computers and motors, the facet is capable of changing its elevation and aim.

2.7.1 Mechanisms to track the sun

The mechanisms of heliostats need to be precise and strong. Some heliostats have multiple mirrors attached to them and can become very heavy. Luckily these devices do not move at high speeds due to the fact that they only have to track the sun. Thus, low speed and high torque are required. One of the devices that meets these requirements is a linear actuator. A linear actuator consists of a threaded bar and a stepper motor. The motor rotates the bar and the thread transfers the force in a linear direction. A linear actuator is a favourable device to be used to change the elevation of the heliostat. Another device that is used for this is a rotary actuator, or slew drive. A big enough stepper motor could provide accurate increments in a radial direction which can rotate the heliostat to track the movement of the sun during the day. It should be noted that when computing the required angle of the heliostat that the mechanical increments will be bigger than the provided increment

of computer calculated value. This is because the mechanics is limited to the tolerances that it was made for while a computer can work with computer error increments. Due to this equipment that is required between the fixed pylon and moving facet, there normally is some distance between the two that, in effect, creates an arm.

2.7.2 Heliostat calibration

The calibration process of a heliostat determines a mathematical model that describes the heliostat. For periodic calibration and alignment of an individual heliostat, a target is usually used. This target can be clearly identified upon most central receiver towers just below the focus point. These are the beam characterisation system (BCS) targets.

These targets are not designed to withstand the same heat as the central receiver, but rather the reflected sunlight of maybe one or two heliostats, which is why they are coated with white paint that scatters the incoming light. A camera system or other instrumentation is used to determine the weighted centre of the reflection from a selected heliostat. If the weighted centre of reflection of the heliostat is not within the expected position then, the estimated parameters are adapted (Monterreal, 2013).

Usually the sun would be used as the reflected light source, but it is also possible to use artificial light sources. With these methods, the reflection of the light from the heliostat is aimed at the centre of the target. When this is achieved, the angles of the heliostat are logged alongside the exact time. This in turn provides the heliostat with a matching data point to be used for calibration. As time passes, the same process is repeated and a new data point is created. The number of data points collected is dependent on the number of variables that is required to be solved to calibrate the heliostat successfully.

To place the calibration of a heliostat in perspective the calibration done by Sun, Guo, Wang, Liang, Xu, Yang and Yu (2015) was adapted. The math for calculating reflection using his parameters can be seen below with the illustration showing the corresponding values of the positions in figures 2.4 and 2.5.

The heliostat's reflection point is set to T_0. From there the azimuth angle, γ, and the elevation angle, α, are calculated by the set of formulas from equation 2.10 to equation 2.19.

Unit solar vector, $\underline{s}$, can be calculated using the solar azimuth angle, γ_s, and the solar altitude angle, α_s:

$$\underline{s} = (s_1, s_2, s_3) = (\cos\alpha_s \cos\gamma_s, \cos\alpha_s \sin\gamma_s, \sin\alpha_s) \tag{2.10}$$

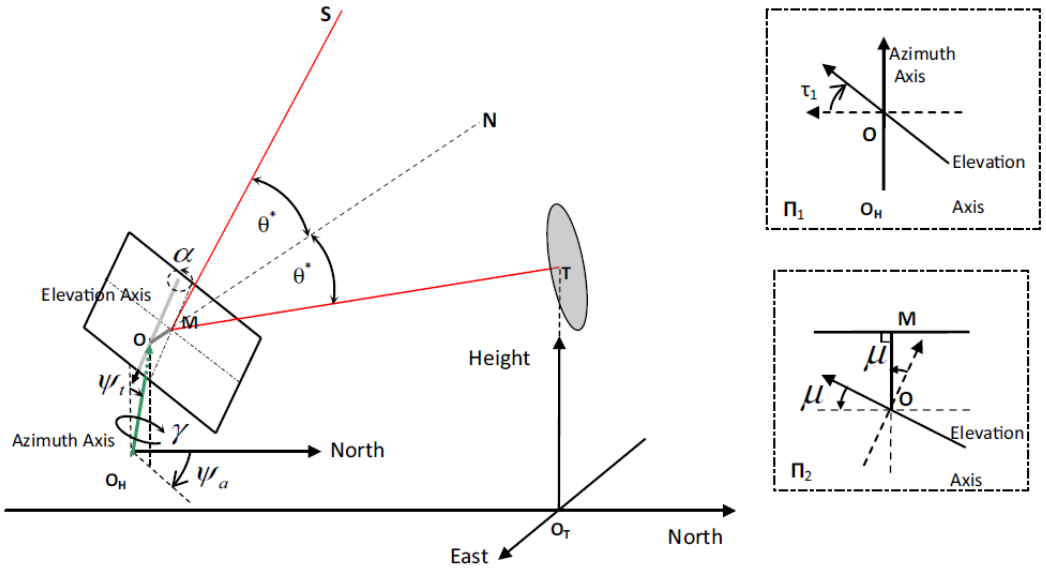

Figure 2.4: Calibration example from Sun *et al.* (2015). Here each calibration parameter can be identified with the components which affect it.

Aim point vector OT_0 can be calculated using the mirror pivot point, (x_0, y_0, z_0), and the target centre, (x_t, y_t, z_t):

$$OT_0 = (t_x, t_y, t_z) = (x_t - x_0, y_t - y_0, z_t - z_0) \tag{2.11}$$

Slant aim-point distance:

$$L = ||OT_0|| = ||(t_x, t_y, t_z)|| = \sqrt{t_x^2 + t_y^2 + t_z^2} \tag{2.12}$$

Calculating the incident angle calibration for mirror-pivot offset τ, where H_z is the distance from the mirror pivot to the mirror surface center and θ is the nominal incident angle relative to the heliostat pivot:

$$\tau = \arcsin\left(\frac{H_z sin(\theta)}{2L - H_z cos(\theta)}\right) \tag{2.13}$$

How to calculate the unit mirror-surface-centre normal, $\underline{n}$, where τ is unit aim point vector:

$$\underline{n} = (n_1, n_2, n_3) = \left(\frac{cos(\tau)}{cos(\theta)}\right)\left(\frac{\underline{s} + \underline{t}}{2}\right)\left(\frac{H_z}{2L - H_z cos(\theta)}\right)\left(\frac{\underline{t} - \underline{s}}{2}\right) \tag{2.14}$$

Calculating the estimated change in the azimuth angle, α^*, where all of the constants c_1, c_2, c_3, d_1, d_2 are complex combinations of the the tilt angle of the azimuth axis and the tilt azimuth angle of the azimuth axis. And τ_1 is the dual-axis non-orthogonal angle:

$$\alpha^* = \arcsin\left(\frac{c_3 - \sin(\tau_1)\sin(\mu)}{\cos(\tau_1)\cos(\mu)}\right) \tag{2.15}$$

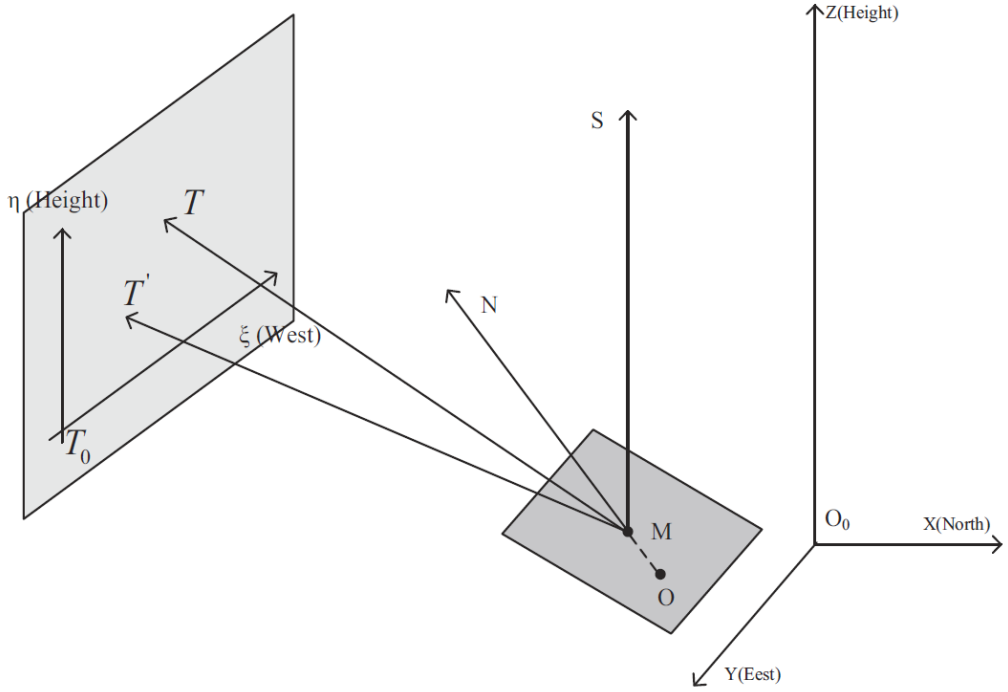

Figure 2.5: This calibration example from Sun *et al.* (2015) indicates how the reflection on the target is compared to the ideal reflection on the target.

The estimated change in the azimuth angle, γ^*, is calculated depending on the resulting value of the combination of the constants:

$$\gamma^* = \arccos\left(\frac{c_1 d_1 + c_2 d_2}{c_1^2 + c_2^2}\right), \text{ if } (c_1 d_1 + c_2 d_2) \geq 0 \tag{2.16}$$

$$\gamma^* = 360^0 - \arccos\left(\frac{c_1 d_1 + c_2 d_2}{c_1^2 + c_2^2}\right), \text{ if } (c_1 d_1 + c_2 d_2) < 0 \tag{2.17}$$

How to calculate the azimuth angle, γ, with the initial azimuth tracking angle, γ_0:

$$\gamma = \gamma^* + \gamma_0 \tag{2.18}$$

Calculating the elevation angle, α, with the initial elevation tracking angle α_0:

$$\alpha = \alpha^* + \alpha_0 \tag{2.19}$$

2.8 2D householder matrix

The heliostats reflect the vectors coming from the sun and therefore it is essential to know how to calculate the reflection in a 3D space. However, before that equation can be derived the 2D reflection matrix should be understood.

The Householder matrix is a mathematical method of creating a matrix that can reflect any vector by which it is multiplied. The following work was based on Sebold and Lacerda (2016), but was derived from principles. For demonstration purposes Figure 2.6 was generated. Using the mirror line, $\underline{h}$, the 2D householder matrix can easily be calculated as follows:

$$\mathbf{H} = \mathbf{I} - 2\ \underline{h}\ \underline{h}^T \tag{2.20}$$

This is then implemented by multiplying an incoming vector with the corresponding Householder matrix that describes the reflective line. The incoming vector, $\underline{s}$, can be described by two components in the 2D plane, the line of reflection, $\underline{n}$, and the mirror line, $\underline{h}$:

$$\underline{s} = \beta\underline{n} + \kappa\underline{h} \tag{2.21}$$

The final result would be the reflection of the incoming vector on $\underline{h}$.

$$\mathbf{H}\underline{s} = (I - 2\ \underline{h}\ \underline{h}^T)(\beta\underline{n} + \kappa\underline{h}) = \beta\underline{n} - \kappa\underline{h} = \underline{t} \tag{2.22}$$

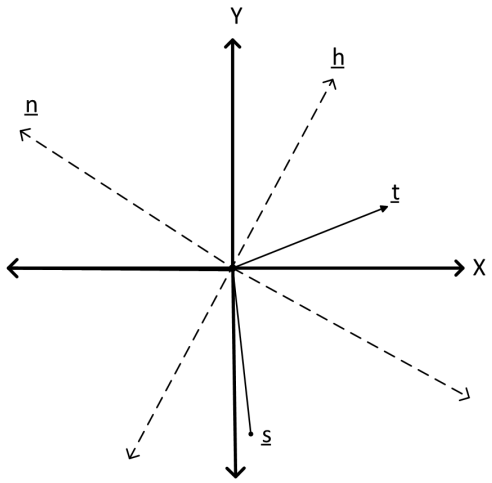

Figure 2.6: Reflection in 2D indicating the normal, $\underline{n}$, the mirror line, $\underline{h}$, an incoming vector, $\underline{s}$, and the resulting reflected vector, $\underline{t}$.

2.9 3D projection

To apply the householder matrix in 3D it is required to first understand projection as well. The following work was based on Kendall (2017), but was derived from principles. Figure 2.7 displays the concept of projecting a vector onto a plane. This plane can be described by giving two non-paralleled vectors from the same origin. If those vectors are orthogonal then you can also calculate the normal of the plane by taking the cross product of the two vectors. The

math can be followed from equation 2.23 to equation 2.41.

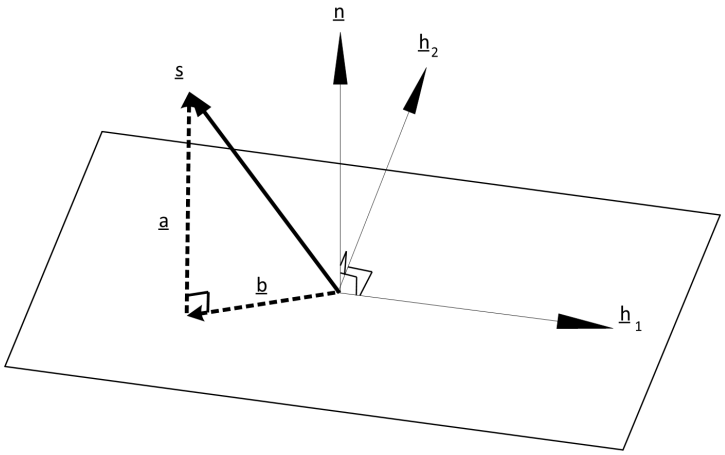

Figure 2.7: Projection in 3D. Indicating a plane defined by two vectors, $\underline{h}_1$ and $\underline{h}_2$. The normal of the plane $\underline{n}$ as well as a vector with its normal projection and plane projection components, $\underline{a}$ and $\underline{b}$.

$$\underline{b} = \underline{h_1}\gamma + \underline{h_2}\kappa \tag{2.23}$$

$$\underline{b} = \begin{bmatrix} h_{1x} & h_{2x} \\ h_{1y} & h_{2y} \\ h_{1z} & h_{2z} \end{bmatrix} \begin{bmatrix} \kappa \\ \lambda \end{bmatrix} \tag{2.24}$$

$$\underline{b} = \mathbf{A}\underline{x} \tag{2.25}$$

$$\underline{a} = \underline{s} - \underline{b} = \underline{s} - \mathbf{A}\underline{x} \tag{2.26}$$

The $\underline{a}$ vector is perpendicular to the plane. Therefore equation 2.27 and 2.28 holds true.

$$\underline{h}_1^T \underline{a} = 0 \tag{2.27}$$

$$\underline{h}_2^T \underline{a} = 0 \tag{2.28}$$

Due to the fact that these two equations work, the equation 2.29 can also be noted.

$$\mathbf{A}^T \underline{a} = 0 \tag{2.29}$$

Substituting $\underline{a}$ with equation 2.26.

$$\mathbf{A}^T(\underline{s} - \mathbf{A}\underline{x}) = 0 \tag{2.30}$$

This can be simplified to solve $\underline{x}$ in equation 2.33.

$$\mathbf{A}^T \underline{s} - \mathbf{A}^T \mathbf{A}\underline{x} = 0 \tag{2.31}$$

$$\mathbf{A}^T\mathbf{A}\underline{x} = \mathbf{A}^T\underline{s} \tag{2.32}$$

$$\underline{x} = (\mathbf{A}^T\mathbf{A})^{-1}\mathbf{A}^T\underline{s} \tag{2.33}$$

Therefore $\underline{x}$ can be substituted in equation 2.25 to form the projection matrix $\mathbf{P}$ seen in equation 2.35.

$$\underline{b} = \mathbf{A}(\mathbf{A}^T\mathbf{A})^{-1}\mathbf{A}^T\underline{s} \tag{2.34}$$

$$\mathbf{P} = \mathbf{A}(\mathbf{A}^T\mathbf{A})^{-1}\mathbf{A}^T \tag{2.35}$$

$$\underline{b} = \mathbf{P}\underline{s} \tag{2.36}$$

It should be noted that $\mathbf{P}$ is the projection onto the plane and that $\mathbf{I}-\mathbf{P}$ is the projection onto the normal. Also, that $\underline{a}$ can be described as seen in equation 2.39.

$$\underline{a} = \underline{s} - \underline{b} \tag{2.37}$$

$$\underline{a} = \underline{s} - \mathbf{P}\underline{s} \tag{2.38}$$

$$\underline{a} = (\mathbf{I} - \mathbf{P})\underline{s} \tag{2.39}$$

$$\mathbf{P}_n = \mathbf{I} - \mathbf{P} \tag{2.40}$$

$$\underline{a} = \mathbf{P}_n\underline{s} \tag{2.41}$$

2.10 Optimization concept

The fundamentals of optimisation requires the use of cost functions. A cost function describes the problem in a mathematical format that is conceivable and calculable. The cost function incorporates all the variables of the problem within it, and assigns penalties to the equation if non-ideal variables are chosen for the problem. During optimisation, the most effective variables would result in the cost function being a minimum.

There is the possibility that there are multiple solutions as seen in Figure 2.8. This can, however, be solved by using multiple starting points for the variables. Therefore, the programme has to figure out the correct combination of variables to minimise this cost function to optimise a given equation.

$$\min_x f(x), \text{ subject to } h(x) = 0 \text{ and } g(x) \leq 0 \tag{2.42}$$

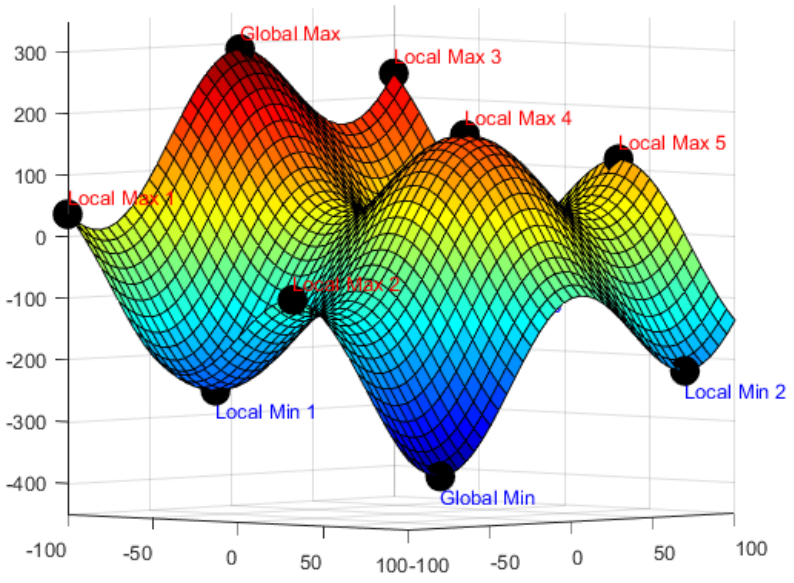

Figure 2.8: 3D function displaying all the possible local minima and maxima of a constrained case. The purpose of this illustration is to indicate all the possible solutions when searching from different starting points. $f(x, y) = 100 \sin\left(\frac{x}{75}\pi\right) + 100cos(\frac{y}{75}\pi) - x + y$

2.11 Interior-point algorithm

Matlab has built-in functions that are capable of solving multi-variable equations. One of these functions is fmincon. Fmincon is a specific minimisation function that uses the interior-point algorithm, with the added functionality of being able to add constraints to the minimisation problem. During optimisation, these variables will be changed by the function and a solution that will minimise the cost function within the set borders would be selected.

$$\min_{x,s} f_\mu(x) = \min_{x,s} f(x) - \mu \sum_i \ln(s_i), \text{ subject to } h(x) = 0 \text{ and } g(x) + s = 0 \tag{2.43}$$

The number of slack variables s_i are the same as the number of inequality constraints. The s_i are positive to ensure that the barrier function $\ln(s_i)$ are bounded. As μ decreases the value of f_μ should approximate the minimum of f. (Constrained Nonlinear Optimization Algorithms, 2018)

2.12 Statistical data analysis

When analysing complex data, it is normal practice to select the mean of the data. This method will be used in this research as the results cannot be described from case to case. Note that the Monte Carlo method will be used.

This method makes use of random sampling to obtain numerical results. Furthermore, it can be used to generate a confidence level figure.

Confidence level figures can be generated when enough sampling is used. It makes use of the mean of the data, $\bar{x}$, combined with the standard deviation of the sample η and the size of the sample k. From there the lower and upper boundaries can be calculated as follows:

$$(\bar{x} - t^* \frac{\eta}{\sqrt{k}}, \bar{x} + t^* \frac{\eta}{\sqrt{k}}) \tag{2.44}$$

The value of confidence constant, t^*, is dependent on the selected sample size and required confidence level as seen in Table 2.2. Choosing a t^* that is as small as possible while maintaining a realistically big sample size and high confidence level will minimize the range of the upper and lower boundaries.

Table 2.2: The t^* table was adapted from t-Table (2018).

Sample Size	**Confidence level**			
	50 %	**80 %**	**95 %**	**99.9 %**
10	0.700	1.372	2.228	4.587
100	0.677	1.290	1.984	3.390
1000	0.675	1.282	1.962	3.300
∞	0.674	1.282	1.960	3.291

Chapter 3

Drones

The objective was stated that a drone must be used to calibrate a heliostat. The concept of calibrating a heliostat has been investigated numerous times, and mostly the method varies around using the sun. Sometimes the only changes made to the standard calibration is to use multiple towers with a target or multiple targets on the towers. Another method that has been explored is using a fixed number of towers with targets made from artificial light sources, such as light-emitting diodes, and a camera on each tower. The fixed positions of the cameras and targets are known. Then, by aiming the heliostat to reflect the light of tower one onto the camera of tower two, a corresponding data point can then be created. This is repeated with all combinations between the towers to achieve the correct number of data points for calibration.

It is clear that the key to calibration is to know from where your light source is coming, and what its relative spatial co-ordinate is. With a drone that can be achieved using a RTK-GPS, so the problem does not lie there. Another requirement is to save the correct data point. The heliostat should be reflecting the sun or the artificial light to the centre of the target and not just anywhere on the target. This reflection is complex and cannot be simplified as an ellipse or a sphere. This is due to the concavity of the reflective surface. So, there should be another way to characterise the reflection in order to assign a centroid to that reflection. When a camera is used to view the heliostat and to search for the reflection of the target, then the light-receiving target becomes a light-emitting source. Therefore, the centre of the target should be identified within the heliostat's concave mirror.

3.1 Camera

The camera that was used during testing is a Nikon D5100. The drone is more than capable of carrying this equipment due to its carrying capacity of 3 kg. However, in practice, it would be standard to use something such as a Hory-

zonHD4 that is both smaller and more compact, with a 14-megapixel camera. The HoryzonHD4 was also tested due to its wireless feed capabilities.

When the drone is in flight, it can position itself anywhere on the field. Therefore, it can search for the reflection of the target in the heliostats. The question is how to keep the drone stationary when it has found a point in space. However, this will not be a concern if a video was taken instead of just photographic images. When a video's time is synchronised with that of the RTK-GPS, then it can be used in post-processing to identify correct positions in space for the calibration data. The only requirement is that the video should not be blurred, as it could influence the centre calculation model and save incorrect RTK-GPS points. However, this is not an extreme concern as drones have been used for photography. The image quality of an image taken by a drone can be observed in Figure 3.1.

Figure 3.1: Example of a photo taken by a drone of a small-scale concentrating solar power plant viewed from the top looking down on the heliostats that are reflecting the sky. Take note of the big drone in the image and the smaller drone in the reflection of one of the heliostats. Courtesy: The TIA Helio100 project.

Another use of images from drones is to show how easily the heliostats can be identified by isolating the reflected blue sky. This in turn will generate a border for future target identification in the heliostat. A small programme on Simulink can achieve this by taking the input image and first separating its colour bands. Thereafter the red colour band is subtracted from the blue

one, and then that image is thresholded. Much noise in the image can still be present from the thresholded image. To erase such noise, a simple filter can be applied on the image. This would change every pixel to the mean of the area around it, and in this way any white speckles would be removed. Then a blob analysis can be done. This will identify big groups of pixels with the same intensities. This can also identify the centre of such a blob as well as its borders that can later be used to identify the target in the heliostat. To visualise the structure of the programme, see Figure 3.2.

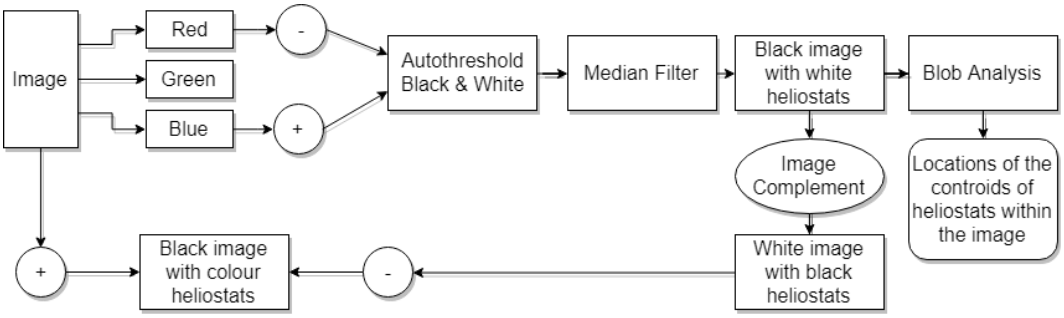

Figure 3.2: Image-processing steps taken to identify the heliostats in Figure 3.1

To demonstrate the effect this programme was applied to Figure 3.1. One method to visualise what the programme is doing, is to investigate what the images look like after processing, as seen in Figure 3.3.

The blob analysis can give valuable information, such as the locations of each mirror in the image, as well as the centre of that blob. This can be seen in Figure 3.4.

The RTK-GPS information would be useless unless it can be calculated mathematically as well. Normal reflection can be done with tedious triangles, but for a model that would incorporate multiple reflection calculations, it was seen as beneficial to use the Householder matrix, also known as the reflection matrix.

3.2 3D householder matrix

The reflection matrix works in such a way that it reflects a vector through a plane. To compensate for that, a simple translation can be made through the origin as seen in Figure 3.5.

$$\underline{s}' = -\underline{s} \tag{3.1}$$

A reflection of a vector in a plane requires only the normal of that plane. Knowing the normal of the mirror plane, the normal projection matrix ($\mathbf{P}_n$)

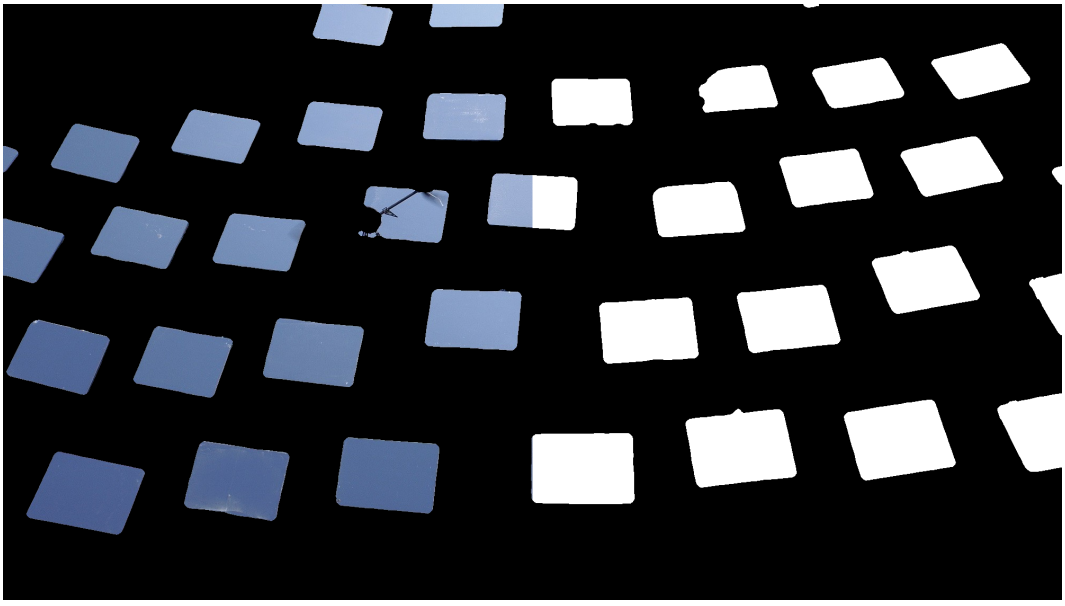

Figure 3.3: What a computer sees when trying to identify heliostats with subtraction, thresholding and filtering is applied in Figure 3.1

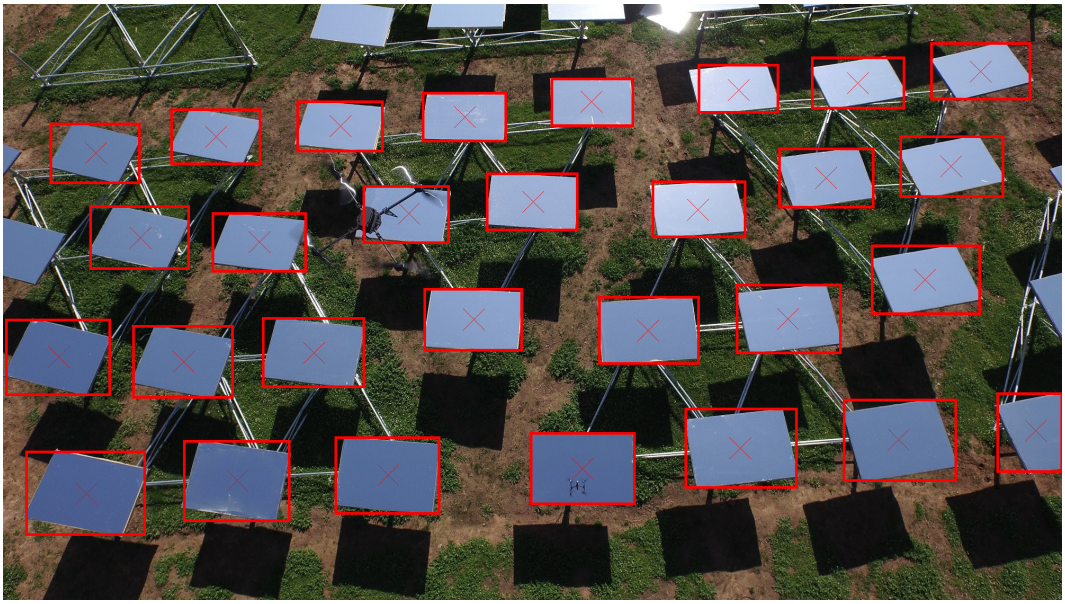

Figure 3.4: Blob analysis applied on Figure 3.3

can be created as seen in equation 3.2.

$$\mathbf{P}_n = \frac{\underline{n}\,\underline{n}^T}{\underline{n}^T\underline{n}} = \underline{n}(\underline{n}^T\underline{n})^{-1}\underline{n}^T \tag{3.2}$$

$$\underline{a} = \mathbf{P}_n\underline{s} \tag{3.3}$$

$$\underline{a} = -\mathbf{P}_n\underline{s}' \tag{3.4}$$

$$\underline{b} = \mathbf{P}\underline{s} = (\mathbf{I} - \mathbf{P}_n)\underline{s} \tag{3.5}$$

$$\underline{b} = -(\mathbf{I} - \mathbf{P}_n)\underline{s}' \tag{3.6}$$

$$\underline{s}' = -\underline{a} - \underline{b} \tag{3.7}$$

$$\underline{t} = \underline{a} - \underline{b} \tag{3.8}$$

$$\underline{t} = -\mathbf{P}_n\underline{s}' + (\mathbf{I} - \mathbf{P}_n)\underline{s}' \tag{3.9}$$

$$\underline{t} = (\mathbf{I} - 2\ \mathbf{P}_n)\underline{s}' \tag{3.10}$$

$$\mathbf{H} = (\mathbf{I} - 2\ \mathbf{P}_n) \tag{3.11}$$

$$\underline{t} = \mathbf{H}\underline{s}' \tag{3.12}$$

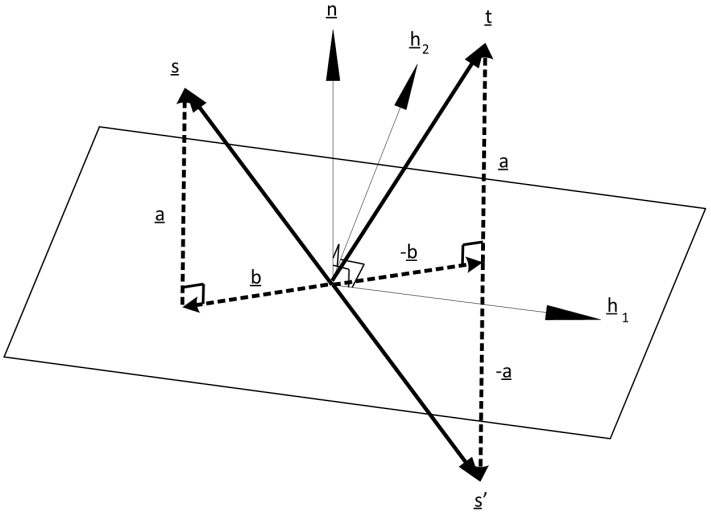

Figure 3.5: Reflection in 3D

3.3 RTK-GPS accuracy test

The RTK-GPS is used for the acquisition of the calibration points. It cannot be assumed that equipment would always perform as advertised, and therefore it was devised to test the accuracy of the system using a simple, yet effective, test.

The concept underlying this accuracy testing is that if both the ground station and drones GPS are placed at a fixed distance from each other, then the corresponding log should show that the drone is stationary. AN expected noise of 30 millimetres will be present. This will be logged and investigated. The drone GPS was placed at a distance of approximately 3300 millimetres away with 8 satellites connected and a logging speed of 10 logs per second. It can also be noted that the RTK-GPS synchronises time with the satellites with

which it connects. This would make synchronising the time of the video much easier and more accurate. The setup is shown in Figure 3.6.

Figure 3.6: Setup of real-time RTK-GPS $33^o55'38''$ S $18^o51'55''$ E at 3:00 PM on the 30th of April 2018

The real-time log was collected for 150 seconds as seen in Figure 3.7. This figure shows how stable each of the directions was during the entire 150 seconds of testing.

The distance root mean square (DRMS) has a 65 % probability that the position solution lies within the 2-dimensional (2D) circle. For mean radial spherical error (MRSE), there is a 61 % probability that the position solution lies within the 3-dimensional (3D) sphere. DRMS and MRSE can give an indication of the accuracy for 2D and 3D, respectively. (McCollum, 2017)

$$DMRS = \sqrt{\frac{\sum_{i=1}^{n}[PN_i^2 + PE_i^2]}{n}} \tag{3.13}$$

$$MRSE = \sqrt{\frac{\sum_{i=1}^{n}[PN_i^2 + PE_i^2 + PD_i^2]}{n}} \tag{3.14}$$

The logged results can be seen in Table 3.1. When comparing to the claimed 30 millimetre accuracy, there is a 143.33 % increase in range in the northern direction and a 203.33 % increase in the downward direction. Therefore

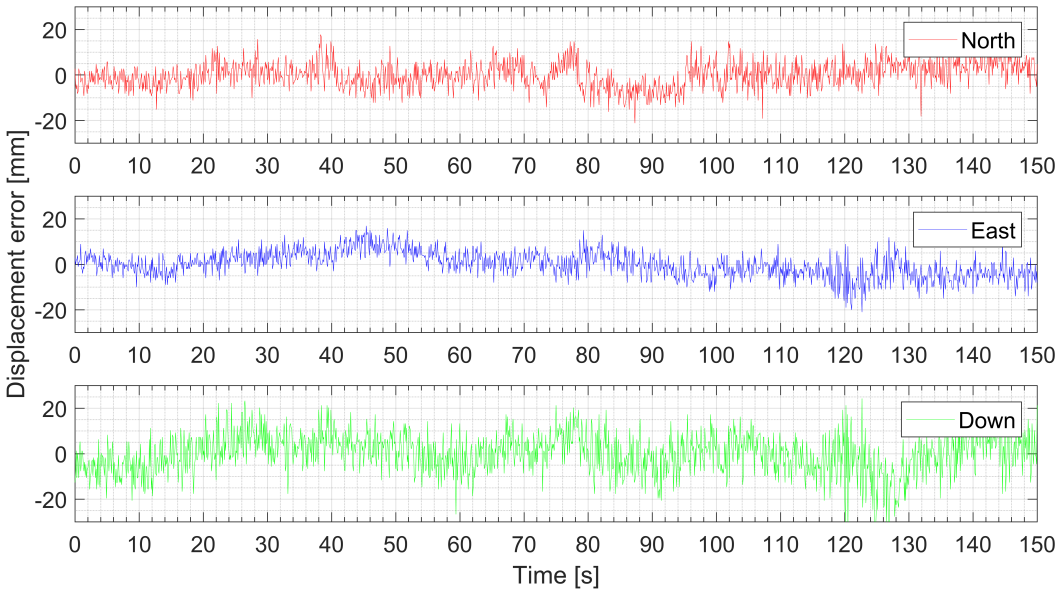

Figure 3.7: Log of realtime RTK-GPS data, RTK Fixed Mode Only. The means from Table 3.1 was subtracted and the resulting noise for 150 seconds was logged.

it cannot be assumed that the drone will have a 30 millimetre accuracy, but that each component will have a different behaviour pattern. It should also be noted that although the range of the results is greater, compared to the claimed 30 millimetres, the standard deviation shows that most values are within 5.781 millimetres from the mean with the northern direction, while in the downward direction it is more spread with a standard deviation of 8.866 millimetres. Therefore, most points will be located within 3 standard deviations, which are a maximum of 26.568 millimetres, which is under the claimed 30 millimetre accuracy.

The standard deviation values collected from the real-time data in table 3.1 were then used to generate an error in the artificial data created in Matlab. This was done to simulate real-world conditions due to the fact that these errors were normally distributed, and not random. Each direction used the same standard deviation values as seen in the Table 3.1.

Table 3.1: Results from RTK-GPS real-time log: the standard deviation of each direction was used for generating virtual noise data. It can also be noted that the MRSE value is higher due to the added dimension, but it is higher than the predicted value of 9.856 due to the error in the downward direction being greater.

	North [mm]	**East [mm]**	**Down [mm]**
Mean	-2108.755	2531.074	135.710
Range	43.000	38.000	61.000
Standard Deviation	5.781	5.602	8.866
DRMS	8.048		
MRSE	11.972		

Chapter 4

Heliostats

Heliostats can be mathematically described, but in order to do so, its purpose, and how it works must be understood. Only then can the real model be converted into a more simplified mathematical model.

4.1 Sun

As the sun is normally used for the calibration process, it is questionable to use anything else, yet there is great motivation to do so. The sun follows a fixed path relative to a fixed point on earth during any specific day. When the calibration of a heliostat is done, then only those options are available to the heliostat's calibration model. But reflecting these points from day to night do not always make use of the full mechanical range of the heliostat. This could influence the performance of the heliostat during the next day, therefore re-calibration is so often needed. This is not a problem for the drone due to the fact that it can fly in a space that the sun would never reach. This forces the heliostat to make use of the mechanical limits of the heliostat.

The process is also limited by the speed at which the sun moves from sunrise to sunset. These do change from summer to winter due to the days being shorter in the winter. If consecutive points were taken every second they would seem to be at the same point in space. Whereas a drone can quickly and easily acquire a new position every second after a calibration point has been found. The only limiting factor to the drone finding a new point would be the speed at which the heliostat can rotate. However, if the possible points for drone calibration can be known beforehand with the estimated heliostat angles, then the process can be optimised in such a manner that the heliostat's total movement is shortened rather than taking a random point approach.

Using the sun also limits the number of heliostats that can be calibrated simul-

taneously. This is due to the fact that the reflection is shone onto a target, and distinguishing between two complex reflections of the sun is already difficult. But when a drone with a camera setup is used, then it is possible to use that same video to identify multiple heliostats and multiple calibration points at one position. It is also possible to illuminate the target, so that calibration can be done in the night and is not limited to the time-span between sunrise and sunset. It should also be noted that one calibration point of any heliostat can be acquired by means of the drone without ever removing the heliostat's sun reflection from the heat collector.

Theoretically due to the fact that multiple points in a wider range will be used to calibrate the heliostat, it could possibly mean that the drone's calibration could be better than using that of the sun as an end result.

4.2 Physical model

For the purpose of this project, a singular heliostat was manufactured and assembled from parts that are currently used at the Helio100 project. Furthermore, it was deemed unnecessary to physically test the calibration on the field with the tower, but it was necessary to prove that the target could be identified. The two main components of a CSP plant are the tower and the heliostats.

4.2.1 Tower

The central receiver, commonly known as the tower, is a combination of the target and a heat collector. Due to the fact that the project was focused on the calibration of the heliostat, a heat collector was not needed, although a target was needed for calibration. These objects can be identified in Figure 4.1.

4.2.1.1 Heat collector

A central receiver for a small-scale heliostat field has the same properties as seen in Figure 4.1. The purpose of the tower is to receive all the heat generated from the reflections of the sun on a concentrated location. This in turn heats a substance such as liquid salt that can be used for more traditional power-generation systems. The heat collector has a non-reflective surface to maximise absorption of sunlight. The target on the tower can be identified as the white target below the heat collector.

Figure 4.1: Helio100 central receiver

4.2.1.2 Target

The traditional reflective white target would unfortunately not be sufficient when trying to identify the centre of reflection from a heliostat's concave mirror. This is due to the design of the target, which does not indicate where the centre is, or how far from the centre the reflection is. A target with a size of 2 x 2 m, similar to a small-scale heliostat field target, such as seen in Figure 4.1 was created with the intention of being identified using computer vision. As such it was important to understand the limitations of a camera. Therefore a simple, yet effective, design for a target was selected, as seen in Figure 4.2a.

The colours chosen are the main colours of any image. Therefore separating each spectrum could be easily done. When a camera is pointed earthwards, the most unlikely colour it would see in a heliostat field would be red. Therefore red was chosen as the outer perimeter. Blue would not have been a logical choice due to the fact that most heliostats would reflect the blue sky in the image, and then it could never have been established when the target has come into view. There is also green grass on many fields, and this could disturb the image recognition if the programme was searching for green from the very beginning, before at first isolating the heliostats.

The target was printed on PVC plastic and mounted on a mild steel frame

using double-sided tape, as seen in Figure 4.2b. A heliostat in a controlled environment was then aimed at the target to observe if the change predicted in the zoom of the target was true at different distances. A more complex image could have been chosen, but because of the uncertainties in this field, a safer approach was decided on, which could also provide as much information as possible.

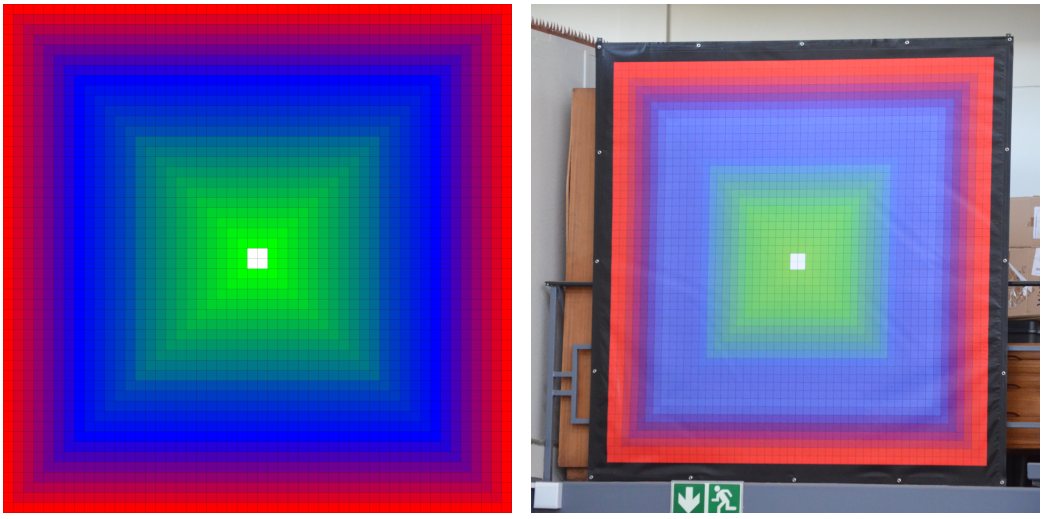

(a) Chosen target design

(b) Actual target mounted in structures laboratory

Figure 4.2: Designed target

To identify the centre of the target is a matter of computing a quadratic polynomial curve to fit the interpretation of the computer's image. If values are assigned to red, green and blue, then an image of the target can be manipulated to represent a concave data set with a centre. Due to the complexity of the raw data, and the noise that will be seen in each pixel, a quadratic polynomial curve would be fitted onto the data. With this in place a minimisation function can then find the centre of the curve and in this way identify the centre of the image as seen in Figure 4.3.

Then test cases were created and the centres of the images of real reflections were then given to the programme to see how it performed as seen in Figure 4.4. These figures shows the weighted centre of the reflection being near the center of the mirror.

To test the programme, a series of images were taken using a camera at different distances from the reflection within the heliostat. These images were then used to confirm the programme's performance. To visualise the effect of

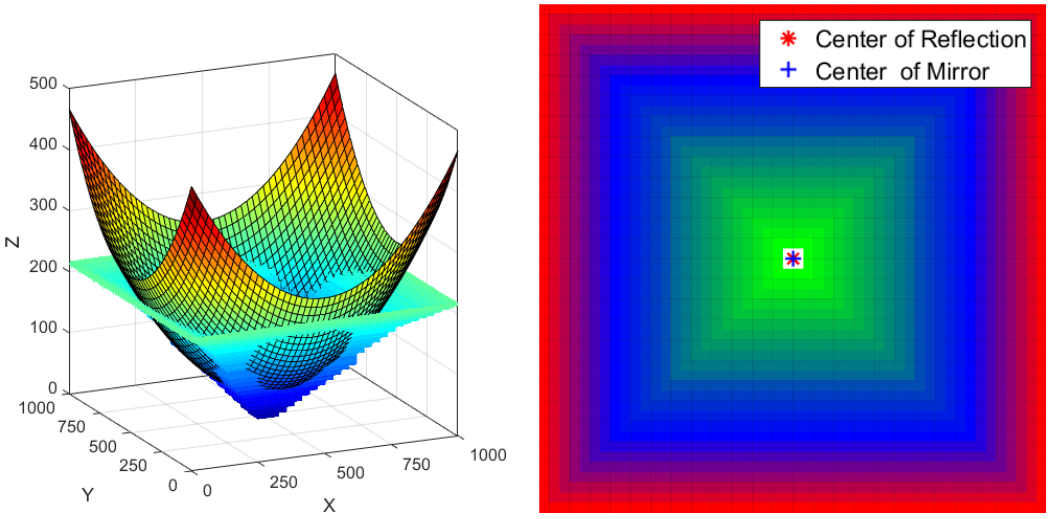

(a) Ideal target representation with a mesh of the quadratic polynomial curve and the raw data.

(b) Ideal target confirming centre of image, that will be the centre of the mirror, and the centre of the target is on the same spot.

Figure 4.3: Theoretical target centre identification

moving left and right when taking a photo of the reflection of the target within the concave mirror two images were taken at approximately 55 metres as seen in Figure 4.5. With the human eye the centre can already be estimated and see what figure is more favourable to be used as a data point. However, when using a video to select the perfect image that has the centre of the heliostat and the weighted centre of image lines up can be done using a program. When that image is found within the video then the timestamp of the image can be used to find the RTK-GPS position at that time.

The performance of the program during extreme conditions was also tested by creating an artificial problem where the weighted centre is in the corner of the heliostat's reflection. It was observed that the program does not find it difficult to fit a quadratic function on the data that represents an accurate answer as seen in Figure 4.6.

Due to the selection of the target design, the function selected to fit it would not be preferable. But it does prove that the centre of the reflection can be identified within a reflection of a concave mirror. A circular contoured target would be efficient at identifying the centre, but the weighted centre should always be considered. The target identification and target selection for concave mirrors can be optimised, but this is unfortunately beyond the scope of this paper.

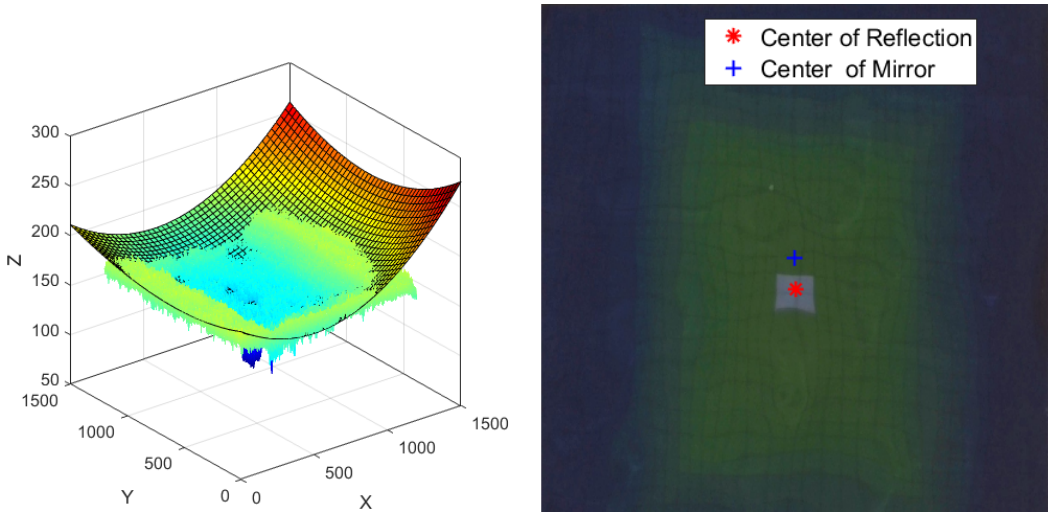

(a) A realistic target reflection with a mesh of the quadratic polynomial curve and the raw data. The noise between pixels can easily be observed with the data points.

(b) The calculated centre of the target and the centre of the mirror which show that the reflection is not yet in the correct position to be used as a calibration point.

Figure 4.4: Realistic target centre identification, Test 1. Showing expected weighted target centre not aligned with the mirror centre.

4.2.2 Heliostat

This model has various variables that describe it as accurately as possible. The heliostat can firstly be described as a device with a specific location in space relative to the target. It was also noted that the facet is rotating and elevating. For the purpose of this research, the following model in Figure 4.7 will be used as a reference to describe the setup.

4.2.2.1 Concave mirror

The mirror is concave, so it will react differently to the way a flat mirror would react. When you decrease the distance from the camera to the mirror it zooms in on its reflection. A simple demonstration can show the effect of moving further away from the mirror as can be seen in figures 4.8 and 4.9. Depending on the amount of concavity of the mirror, the relationship between distance and zoom changes.

If the concave mirror is simplified to a straight surface with an inclination at the end, then the amount of zoom can be calculated as seen in Figure 4.10. The math then shows how it is calculated from equation 4.1 to 4.5.

Calculating the angle between the camera and concave mirror tip, σ, using the

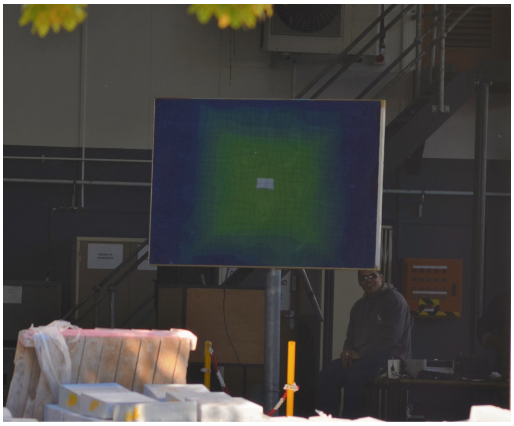

(a) Photo taken with the approximated centre of heliostat and weighted centre of the reflection lined up. This photo was taken with the heliostat and target in the laboratory while the camera was across the street 55 metres away.

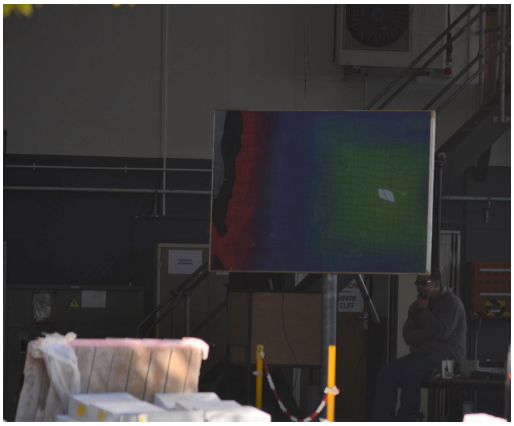

(b) Photo taken with a distance of 55 metres from the target and 1 metre to the right. It can be observed that relative small changes in position displaces weighted reflection centre with an observable distance from mirror centre.

Figure 4.5: Realistic target centre identification, Test 2. This test shows the effect of moving towards the right with 1 metre has on the weighted centre of reflection. The weighted centre of reflection can be approximated as the centre of the target within the reflection.

ratio between the distance from the camera to the concave mirror tip, D_{Camera}, and the size of the mirror S_{Mirror}:

$$\sigma = \arctan\left(\frac{S_{\text{Mirror}}}{2\ D_{\text{Camera}}}\right) \tag{4.1}$$

The angle between the camera and normal of concave mirror tip, ω, using the concavity of the mirror, C_{Mirror}:

$$\omega = \sigma - C_{\text{Mirror}} \tag{4.2}$$

And the angle between concave mirror tip and target tip θ

$$\theta = \omega - C_{\text{Mirror}} \tag{4.3}$$

Calculating the zoom on target, z:

$$z = D_{\text{Target}} \tan(\theta) \tag{4.4}$$

Resulting in the required width of the target, W_{Target}:

$$W_{\text{Target}} = S_{\text{Mirror}} + 2{\times}z \tag{4.5}$$

Applying equation 4.5 to a fixed target distance of 27 metres and a mirror size of 1.9 metres and a target size of 2 metres with real-world distances measured

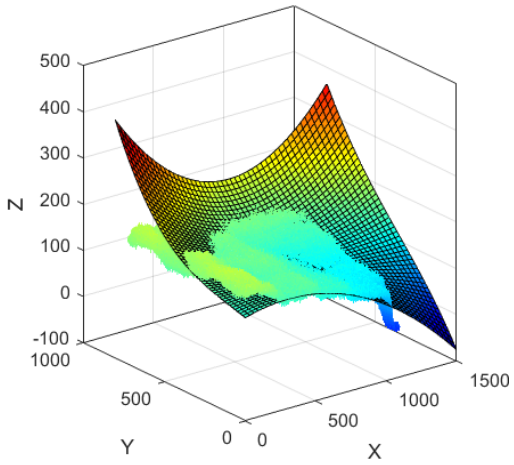

(a) A realistic target reflection with a mesh of the quadratic polynomial curve and the raw data. Note that with images the top-right corner is $[1052, 0]$.

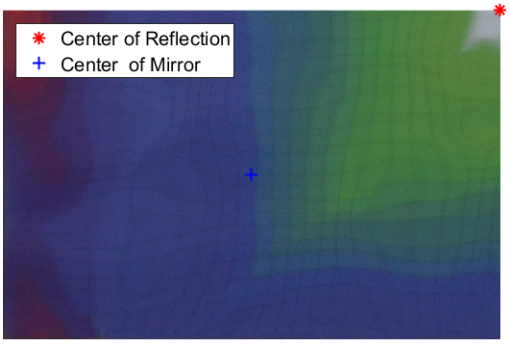

(b) The calculated centre of the target and the centre of the mirror show that the reflection is not yet in the correct position to be used as a calibration point.

Figure 4.6: Realistic target centre identification, Test 3. Showing code performance with extreme cases.

with a laser, the maximum concavity on the edge of the mirror was calculated to be 0.797 degrees for the specific heliostat. Figure 4.11 therefore can predict the required target size that will be needed when the mirror-centre-to-camera distance is changed as well as the mirror-centre-to-target distance.

It should be noted that in a heliostat field most of these mirrors have approximately the same concavity if they are equidistant from the target. Heliostats with different distances from the target require different concavity in order to focus the sunlight. This can be visualised by analysing Figure 4.11: the plotted target of 7 000 mm shows much less decline in recommended target width compared to the tested 27 000 mm case. This would mean that when the sun is reflecting onto that specific heliostat, then the reflection size on the target would be approximately 380 % bigger if the same concavity is used for both the 27 000 mm and 7 000 mm mirror-centre-to-target distance heliostats. This concludes that the concavity would not be the same from heliostats in the field with different distances from the target, because it would cause great inefficiency in the plant.

At a camera distance of 32 000 mm for our test case the designed 2000 mm target would be identified as predicted in Figure 4.11. Therefore, the red perimeter of the target could be used to identify the borders of the target when it enters the edges of the facet. When this knowledge is established, those corners would then create the borders on which the camera should focus during the rest of the test. As the distance of the drone towards the target

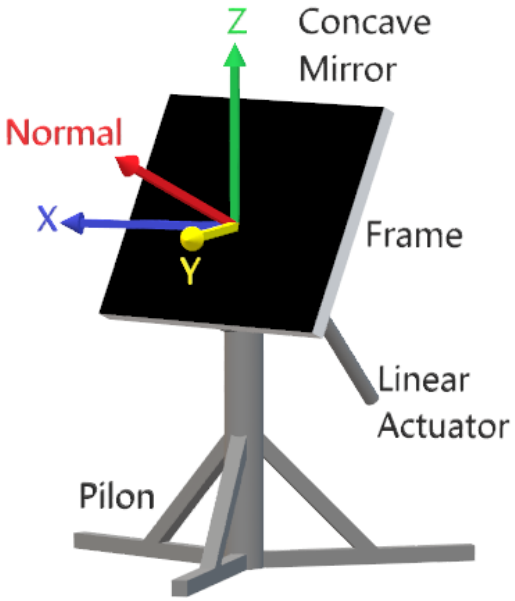

Figure 4.7: A 3D CAD model of the Heliostat used in research

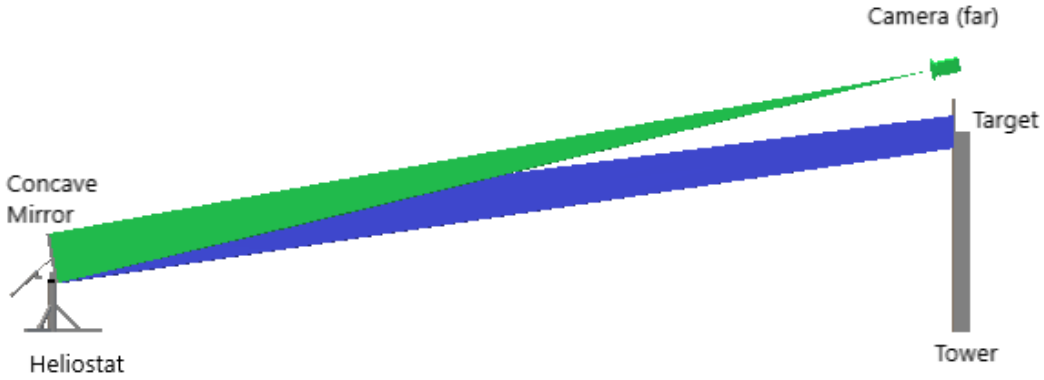

Figure 4.8: This figure shows a heliostat positioned in a field and a target. If the camera is placed in the correct position away from the concave mirror, the image that it would see on the reflection would be focused rather than spread out as would be the case if a flat mirror were used. Also note the size of focus on the target as the effect of placing the camera far from the concave mirror.

increases, the red borders of the target will disappear and only the blue borders will be left at a camera distance of approximately 45 metres away from the heliostat. Only at a distance greater than 70 metres will the green start to disappear.

Therefore at a distance greater than or equal to 32 metres, when the full target is in view, then the target's centre will be identified. When the weighted target's centre corresponds with the centre of the mirror then that position in

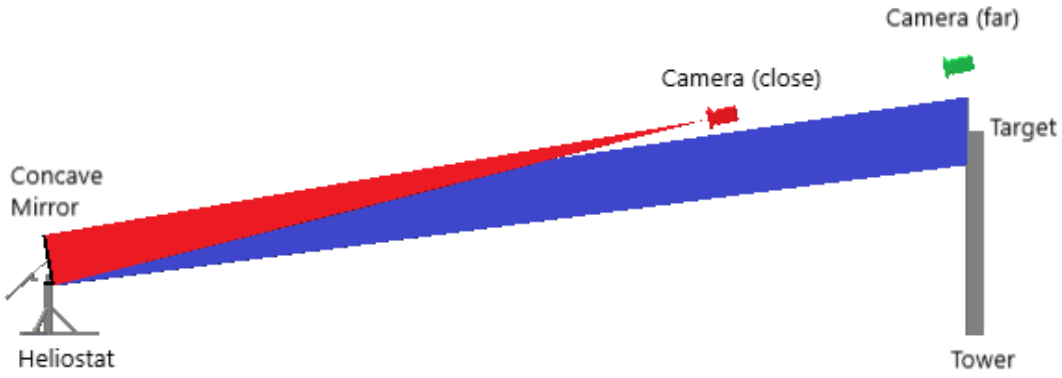

Figure 4.9: This figure shows the effect of reducing camera distance to the concave mirror. It shows that the focused area on the target is much bigger and spread out when compared to the previous camera position that was further away. This CAD model is just for demonstration purposes and the real distances are dependent on the heliostat's concavity.

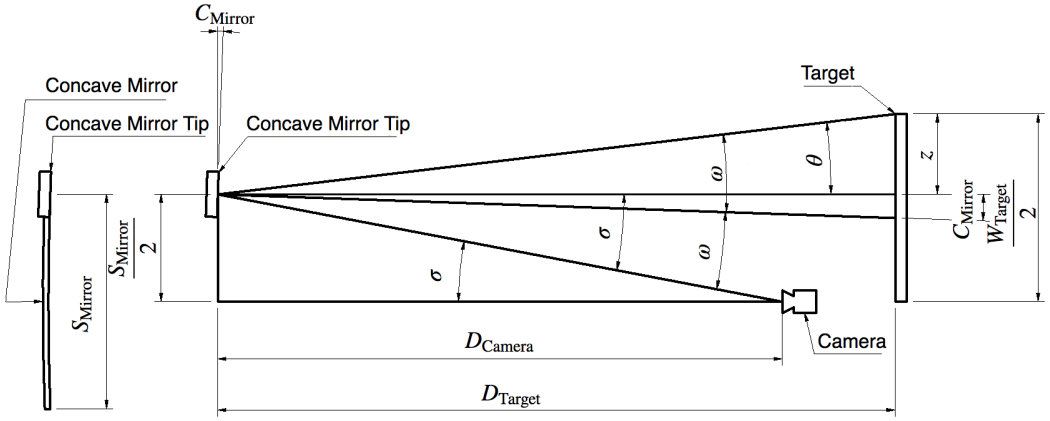

Figure 4.10: Illustration of calculating the zoom on a target. The concave mirror is placed on one side and represents the zoomed-in side of the concave mirror that can be approximated by a straight mirror. On the other hand, the target is a representation of half of the width of the real target. This would demonstrate the concept of the size of the target's width reflected for a specific heliostat in the field. The distances and angles are all dependent on the heliostat's concavity and therefore is not in proportion. It only demonstrates the calculations procedure.

space can be used for the calibration process.

It was noted that in Figure 4.11 the predictions crossed a camera distance of 34130.774 mm and gave a resulting target width of 1900 mm. Thus, it was concluded that for heliostats close to 27 000 mm from the target the amount of gain received from increasing the camera distance is not beneficial enough

in all cases at a distance of past 34 metres.

One of the biggest factors in selecting the camera distance was also the camera's image quality. If the distance is increased to 70 metres, the number of pixels available to do the analysis would be a concern. However, the use of a high-quality camera would resolve this issue.

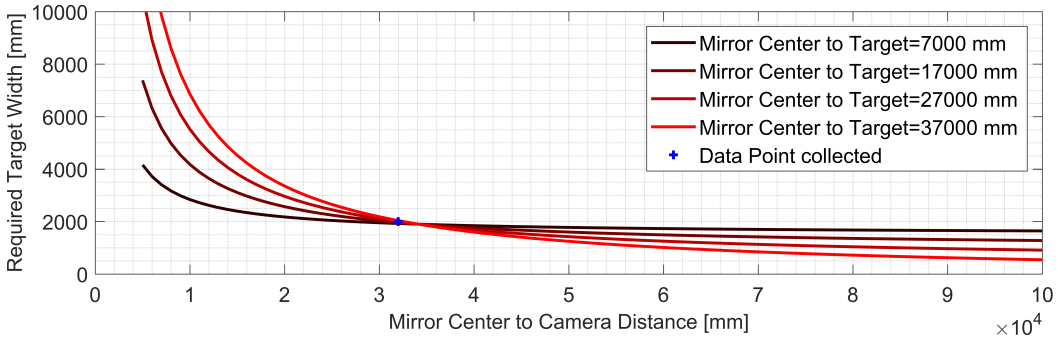

Figure 4.11: Predicting the target's zoom for different distances of a tested heliostat. The collected data point was on 27 000 mm and if the same concave mirror were observed at different distances with the camera, then a required target width could be tracked on the figure. If the same mirror with that specific concavity is then moved in the field closer or further away from the target, then its performance could be estimated using the figure.

Figure 4.12 shows the estimated heliostat's reflection behaviour of a real field. Each heliostat in the field has different concavities. Thus required camera distance can be seen increasing as the target distance increases.

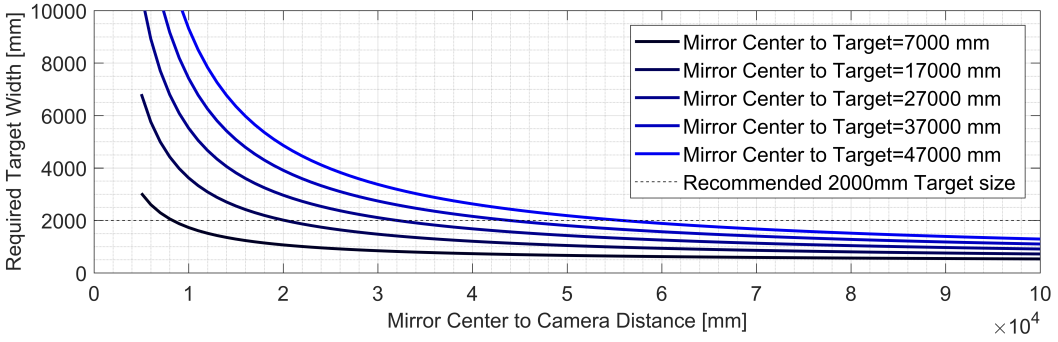

Figure 4.12: Using the test case as reference, the reflection size of the sun on the target was calculated. From there the concavity was calculated for heliostats with different distances from the target, and their estimated predicted behaviour was generated.

4.2.2.2 Frame

This specific heliostat's frame is designed to keep the concavity of the mirror fixed. In order to do so it has a setting paste in the frame and a flat mirror was placed onto the paste. Thereafter the mirror was manually made concave by applying force to the centre. This does not produce the finest quality and to keep the concavity the same throughout the set of these facets, is extremely difficult. It should not be assumed that all mirrors have the same concavity. These frames limit the concavity and might cause defects during the manufacturing process. This was noted when different facets' reflections of the same target had a measurable difference in the concavity. Other mirrors also displayed defects that would make the facet unfit for use in a field.

4.3 Virtual model

Setting up a virtual model would be the most efficient method of testing the possibility of calibrating the heliostat using a drone. However, this requires a calibration equation that would work for both the drone and the sun as a baseline. For the calibration of a heliostat, knowledge is required of data points that can be used with a corresponding heliostat. Therefore, a heliostat must be created in a virtual space.

As mentioned before, the increments of the mechanical equipment to change the heliostat could be much bigger than the provided increments of the calculated angle of the heliostat when tracking the sun. The increments of the linear actuator and rotary actuator were not enforced onto the system, due to the fact that they could cause both to perform just as well in some specific cases. They could also make the subcases perform better than they were actually calculated to be, due to rounding up the required or calculated angle to its nearest increment.

Although the calculated theoretical accuracy of the rotary actuator used is 0.440 milliradians per pulse, the backlash on the motor is measured to be 1.5 milliradians. While, if the azimuth angle of a heliostat was calculated every second, then it could achieve a typical accuracy of 0.040 milliradians per second for a heliostat at 10 am. The elevation angle would typically change then for that heliostat with a value of 0.022 milliradians per second. The linear actuator has a better calculated theoretical accuracy of 0.111 milliradians per pulse, but in both these cases, it does not meet the calculated milliradians required per second.

4.3.1 Virtual heliostat properties

If a heliostat was built it would be built from the ground up. Therefore the heliostat must have a pylon similar to that seen in Figure 4.13a with a specific height connected to it. Next is the rotary actuator, a device which allows radial translations of the facet. Due to the facet being the rotating object, and the pylon not changing position during this rotation, it was found that assigning a spatial co-ordinate of $[0, 0, 0]$ to the pylon's top would ensure a fixed co-ordinate system that can be measured in the real world with a longitude, altitude, and azimuth. This point is stationary relative to earth, while the centre of the mirror moves. The next component is the linear actuator, which is a device that allows the facet to change its elevation.

These two devices move the mechanical arm, but the mechanical arm translates the centre point of the mirror's co-ordinate system for this specific heliostat setup. In most heliostats, this effect is present. In some cases where the heliostats are enormous, the centre of rotation and the centre of the mirror are always at the same point by design. However, with a mechanical arm the centre of the mirror changes as the angle of the facet changes. This change might seem minor when using the sun as a calibration mechanism, but due to the drone's distance of 32 000 mm this effect of changing the centre of the mirror will influence the calibration, and therefore has to be kept in mind.

There must be a target in this virtual world: therefore a target with a certain distance in the x, y, and z-direction relative to the pylons $[0, 0, 0]$ was created. This can be calculated in the real world using the co-ordinate system. However, the mirror's centre must be recalculated each time the elevation, or azimuth, of the facet changes, but due to the fact that it is mechanically constrained, as the mechanical arm has a fixed length, this will not be difficult to calculate.

4.3.2 Virtual heliostat calibration parameters

Some parameters that must be analysed are the relative distance from the pylon to the target. It would be possible that the pylon has shifted position during the last time the co-ordinates of the heliostat were taken. Also note that these co-ordinates will be retrieved using the RTK-GPS that is also only accurate to 30.5 millimetres in the worst cases, as seen in Table 3.1. The measured distances used for calibration parameters is visualised in Figure 4.14 with an orthographic view of a pylon with a target.

It is possible that the pylon is not perfectly perpendicular to the ground, and has some tilt. This will cause a displacement in the pylon's $[0, 0, 0]$ co-ordinates, as well as influence the elevation and azimuth of the facet. The effect of tilting

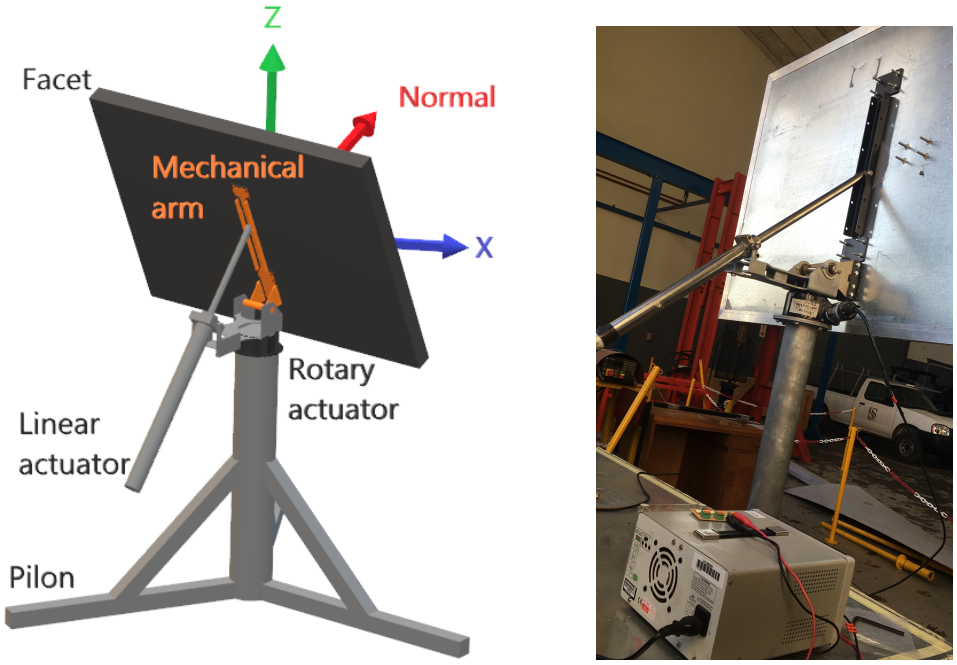

(a) Heliostat 3D model from behind

(b) Heliostat in laboratory displaying the real components

Figure 4.13: Heliostat viewed from behind

the pylon is visualised in Figure 4.15 with an orthographic view of a heliostat with reference to the ground.

The measured elevation and azimuth of the facet could also be incorrectly zeroed, or there could be a difference between the measured angle and the digital output of that angle. This could cause a fixed bias in the readings. Also, a different angle would translate the mirror's centre from the expected centre due to the mechanical arm. The mechanical arm can be described by two lengths towards the centre of the mirror from the reference point taken on the pylon, as seen in Figure 4.16.

The mechanical arm influences the distance from the pylon to the centre of the mirror. This has an influence on the reflection. Therefore, if the properties of the mechanical arm are not manufactured correctly, or are assembled higher or lower against the facet frame than expected, then these properties will change the reflection. It is also possible that the expected centre of the mirror, when the concavity of the mirror is created, is not at the centre of the mirror. It was also noted when assembling a heliostat that there was a bulge present at the back of the frame that would cause displacement in the normal direction of the facet, tightening the nuts forced this bulge to give way.

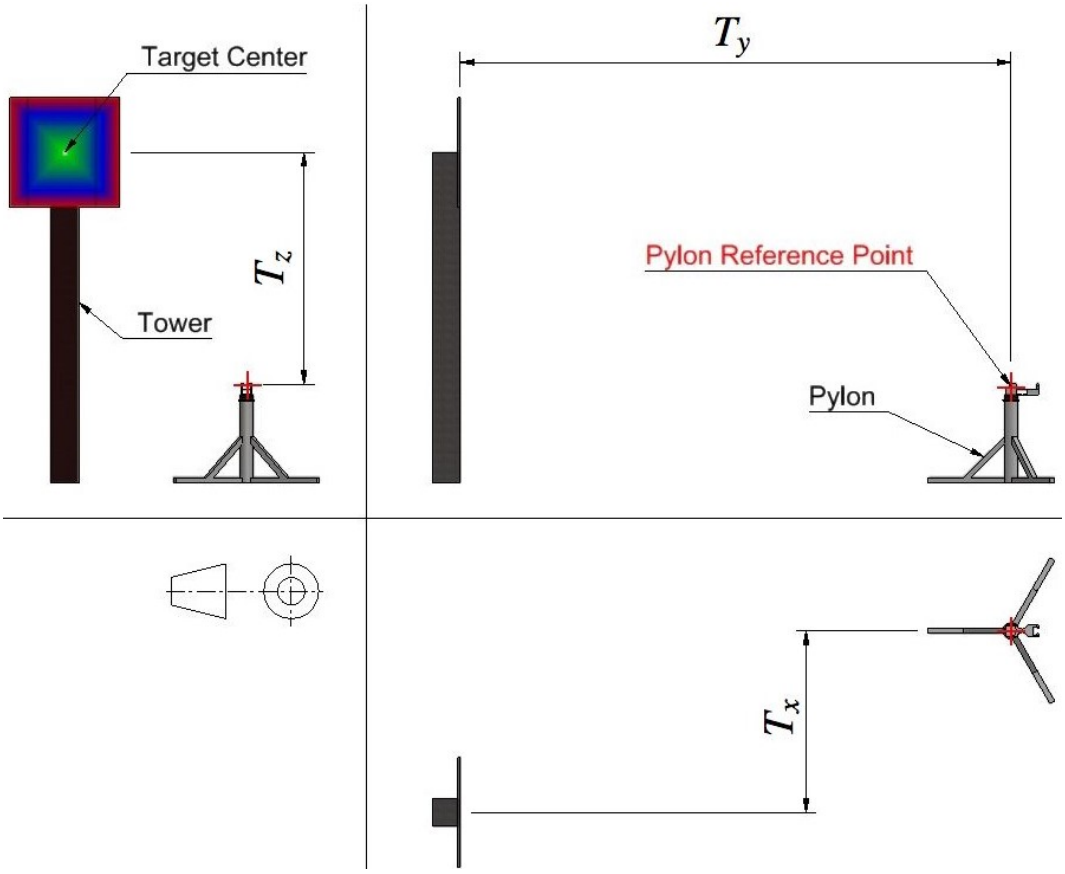

Figure 4.14: The target vector, $\underline{T} = [T_x, T_y, T_z]$, calculated from the pylon reference point to the target centre.

It is also calculated that the drone should be a distance of 32 metres away from the pylon's centre. However, the mechanical arm of the heliostat affects the distance from the mirror centre to the drone, while the drone's position is also uncertain due to the accuracy of the RTK-GPS. The absolute distance to the mirror's centre can be calculated if all the other information regarding the heliostat is known. Therefore, using the mathematical connection between the mechanical arm and the angles of the facet, the distance to the drone can be incorporated into the optimisation solution.

The factor of the GPS would be difficult to compensate for due to the fact that it is unlikely to have a fixed error received from the drone's RTK-GPS. For example that it is always off by 3 millimetres in the northern direction. The non-bias behaviour was observed from the logged data, therefore trying to compensate for this factor may only increase the error.

But there is also the possibility that the distance between the mounted camera and the drone's RTK-GPS is not what is measured or shifted due to vibrations

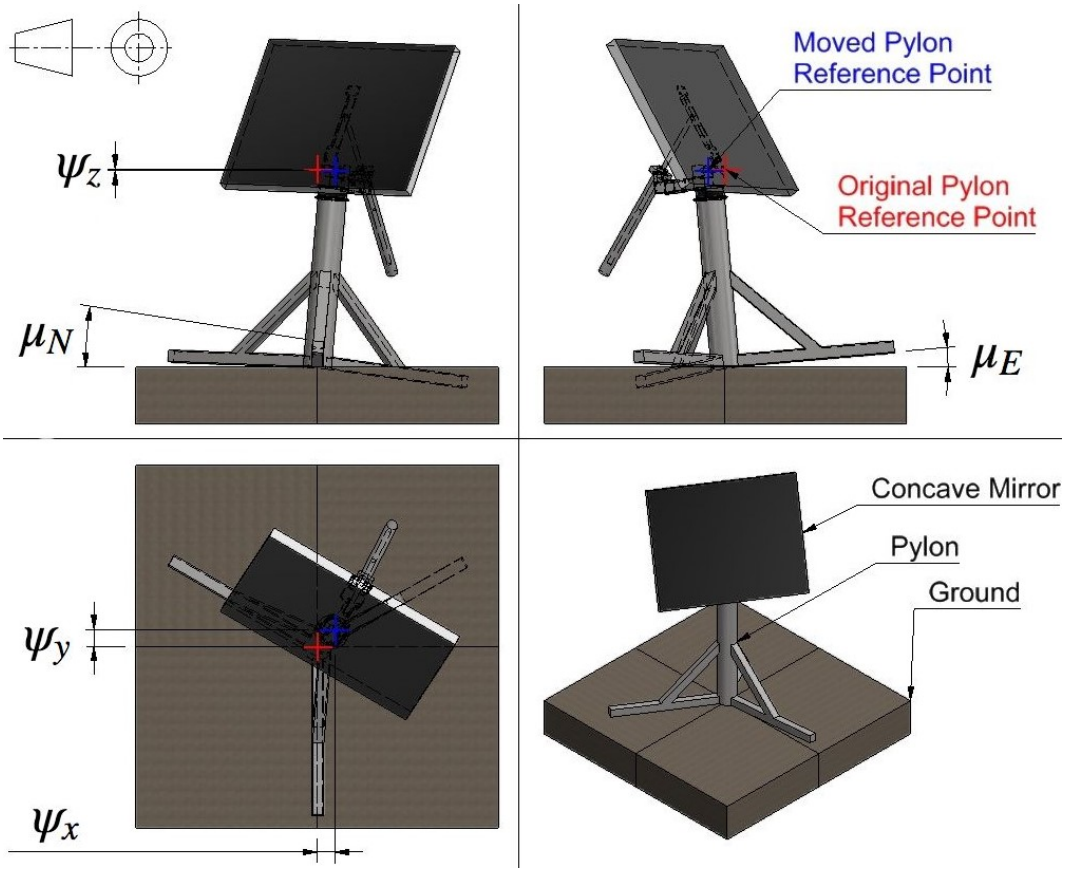

Figure 4.15: Pylon reference point shift due to tilt around Northern axis, μ_N, and tilt around Eastern axis, μ_E. The shift distance caused in each direction can be described by the pylon shift vector, $\underline{\psi} = [\psi_x, \psi_y, \psi_z]$.

during flight.

When a fixed mount for the camera is used, then this factor will not be great. However, when using a gimbal, it is essential to make sure that the centre of the camera must be at a fixed relative position to the RTK-GPS during the design of the gimbal.

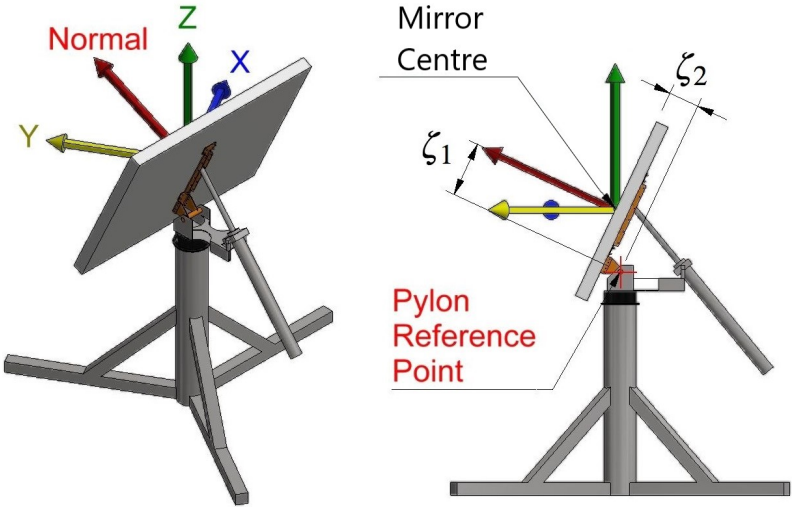

Figure 4.16: Indication of mechanical arm length 1, ζ_1, and mechanical arm length 2, ζ_2, used for the parameters in calibration of the heliostat.

Chapter 5

Calibration

Calibration refers to the process by which the model parameters of a particular heliostat are estimated. Calibration typically requires a set of measurements that contain two types of information: (1) the sun's position at various times; and (2) the angles of the heliostat for which the heliostat reflects those solar rays to the target.

The model parameters that best fit the measured data are considered to be the calibration constants for that particular heliostat. The calibration constants can be found by means of optimisation by viewing the problem as a regression problem.

5.1 Calibration points

The optimisation process was used to estimate the calibration parameters of the virtual heliostat model to test the theoretical calibration of a drone. The true value of each parameter was selected beforehand. Thereafter calibration was done using 2, 5, 10, 25, 50, 100, 200 and 240 points retrieved from the artificial drone positions.

The sun is also used with the matching number of points used for the drone, but spread equally throughout a day (10th of January). The drone is not limited to an arc such as the sun.

The points that were used to calibrate the heliostat with the drone were randomly generated. With a random generation of drone positions, it was possible for the point to lie behind the heliostat in line with the target or at an angle that the heliostat cannot reach, due to mechanical limitations. These points would not be usable in the real world as well. The programme knows the exact properties of the virtual heliostat, therefore it would pick up that at the specified drone position, the heliostat would not be capable of reflecting onto

the target. Therefore, in the programme the drone positions would also be thrown out and a new point generated until it could verify that it reflected onto the target.

The method used in the real world would be very similar. When the drone is placed at some position and the heliostat does not reflect the target, then the drone would not save that point as a calibration point, but would move to a different location, until it identifies the target and then saves that point for calibration.

5.2 Cost functions description

When two calibration points are used then the cost function consists of the sum of two functions that require minimisation. Each of these functions describes the norm of the calculated difference between the reflection's position on the target caused by the vector of the drone with the estimated parameters of the heliostat and the target's centre. Of course, when these parameters are estimated correctly then the difference in the target's centre and the reflection on the target would be zero. In this way, the optimisation would find the best suitable parameters with which to describe the heliostat which caused these differences to be as small as possible.

One reason why these parameters are not being estimated correctly every time is due to the number of parameters. When there are 10 parameters, then 10 equations need to be solved simultaneously in order to arrive at the correct answer. Therefore, the cost function combines the number of calibration points provided, and adds all these norms of differences in the target together to create a simultaneous solution effect. Therefore, if 2 and 5 points are used for calibration, and the system has 10 variables, it will not be able to calculate all 10 variables, but one could estimate what they might be. When using 10 calibration points for the 10 variables, the problem becomes trivial for a computer and it will solve the parameters of the heliostat with computer error accuracy.

The second reason why all of the parameters calculated by the computer are not always accurate to computer error accuracy when more than 10 points are used is due to fact that the calibration points given are not perfect. Each calibration point received from the drone is corrupted by random noise in each direction caused by the RTK-GPS. This was simulated by forcing in random noise into each point and each direction with the corresponding standard deviation of that direction. Thus, when the optimisation of the cost function tries to minimise the cost function, it would never be able to perfectly minimise the cost function to zero, because the points of the drone do not allow it.

5.3 Heliostat model

This section follows the procedure to calculate the elevation and azimuth angles of a heliostat to reflect an incoming ray towards the centre of the target.

The estimated displaced target position $\underline{T}^*$ calculated by using the target position $\underline{T}$ and adding the estimated displacement of the heliostat $\underline{\delta}^*$:

$$\underline{T}^* = \underline{T} + \underline{\delta}^* \tag{5.1}$$

Calculating the final estimated rotational matrix $\mathbf{\Phi}^*$ from the estimated rotational matrix around the northern $\mathbf{R}_N^*$ and eastern $\mathbf{R}_E^*$ axis caused by the tilt μ:

$$\mathbf{R}_E^* = \begin{bmatrix} 1 & 0 & 0 \\ 0 & \cos(\mu_E^*) & -\sin(\mu_E^*) \\ 0 & \sin(\mu_E^*) & \cos(\mu_E^*) \end{bmatrix} \tag{5.2}$$

$$\mathbf{R}_N^* = \begin{bmatrix} \cos(\mu_N^*) & 0 & \sin(\mu_N^*) \\ 0 & 1 & 0 \\ -\sin(\mu_N^*) & 0 & \cos(\mu_N^*) \end{bmatrix} \tag{5.3}$$

$$\mathbf{\Phi}^* = \mathbf{R}_E^* \mathbf{R}_N^* \tag{5.4}$$

Calculating the estimated mechanical arm's angle ζ_a^* and radius ζ_r^*:

$$\zeta_a^* = \tan\left(\frac{\zeta_2^*}{\zeta_1^*}\right) \tag{5.5}$$

$$\zeta_r^* = ||\zeta^*|| \tag{5.6}$$

Pylon shift $\underline{\psi}^*$ caused by the tilt μ and the length of the pylon L_P:

$$\underline{\psi}^* = \mathbf{\Phi}^* \begin{bmatrix} 0 \\ 0 \\ L_P \end{bmatrix} - \begin{bmatrix} 0 \\ 0 \\ L_P \end{bmatrix} \tag{5.7}$$

Variation between the centre of the mirror and the pylon's reference point caused by the angles of the heliostat's mirror with the mechanical arm and the pylon shift:

$$\underline{\upsilon}^*(\alpha, \gamma) = \mathbf{\Phi}^* \begin{bmatrix} \sin(90 - \alpha - \zeta_a)\zeta_r \sin(\gamma) \\ \sin(90 - \alpha - \zeta_a)\zeta_r \cos(\gamma) \\ \cos(90 - \alpha - \zeta_a)\zeta_r \end{bmatrix} + \underline{\psi}^* \tag{5.8}$$

The adjusted-estimated-relative target vector from the centre of the mirror, $\underline{T}^{*\prime}$, caused by the variation of the offset of the mirror's centre:

$$\underline{T}^{*\prime}(\alpha, \gamma) = \underline{T}^* - \underline{\upsilon}^*(\alpha, \gamma) \tag{5.9}$$

Calculating relative distances from the target and sun or drone to the centre of the mirror:

$$\underline{s}^{*\prime}(\alpha,\gamma) = \underline{s}^{*} - \underline{v}^{*}(\alpha,\gamma) \tag{5.10}$$

Normalised projected sun vector:

$$\underline{s}^{*\prime\prime}(\alpha,\gamma) = -\frac{\underline{s}^{*\prime}(\alpha,\gamma)}{||\underline{s}^{*\prime}(\alpha,\gamma)||} \tag{5.11}$$

Calculating the heliostat vectors that describe the mirror plane:

$$\underline{h}_1^{*}(\alpha,\gamma) = \begin{bmatrix} \cos(\gamma) \\ -\sin(\gamma) \\ 0 \end{bmatrix} \tag{5.12}$$

$$\underline{h}_2^{*}(\alpha,\gamma) = \begin{bmatrix} -\sin(\gamma)sin(\alpha) \\ -\cos(\gamma)sin(\alpha) \\ \cos(\alpha) \end{bmatrix} \tag{5.13}$$

Adjusting the heliostat vectors due to tilt μ:

$$\underline{h}_1^{*\prime}(\alpha,\gamma) = \mathbf{\Phi}^{*}\underline{h}_1^{*}(\alpha,\gamma) \tag{5.14}$$

$$\underline{h}_2^{*\prime}(\alpha,\gamma) = \mathbf{\Phi}^{*}\underline{h}_2^{*}(\alpha,\gamma) \tag{5.15}$$

Calculating normal of the mirror plane by using the two orthogonal vectors of the heliostat:

$$\underline{n}^{*}(\alpha,\gamma) = \underline{h}_1^{*\prime}(\alpha,\gamma) \times \underline{h}_2^{*\prime}(\alpha,\gamma) \tag{5.16}$$

Calculating the normal projection matrix:

$$\mathbf{P}_{n^*}^{*}(\alpha,\gamma) = \frac{\underline{n}^{*}(\alpha,\gamma)\ \underline{n}^{*}(\alpha,\gamma)^{T}}{\underline{n}^{*}(\alpha,\gamma)^{T}\underline{n}^{*}(\alpha,\gamma)} \tag{5.17}$$

Calculating the householder matrix:

$$\mathbf{H}^{*}(\alpha,\gamma) = (\mathbf{I} - 2\ \mathbf{P}_{n^*}^{*}(\alpha,\gamma)) \tag{5.18}$$

Calculating the target vector $\underline{t}^{*}$ by using the householder matrix $\mathbf{H}$ and the incoming sun vector $\underline{s}$:

$$\underline{t}^{*}(\alpha,\gamma) = \mathbf{H}(\alpha,\gamma)\underline{s}^{*\prime\prime}(\alpha,\gamma) \tag{5.19}$$

Normalising the target vector:

$$\underline{t}^{*\prime}(\alpha,\gamma) = \frac{\underline{t}^{*}(\alpha,\gamma)}{||\underline{t}^{*}(\alpha,\gamma)||} \tag{5.20}$$

Calculating relative target distance multiplier:

$$L_T^{*}(\alpha,\gamma) = \left| \frac{T^{*\prime}{}_y(\alpha,\gamma)}{t_y^{*\prime}(\alpha,\gamma)} \right| \tag{5.21}$$

Calculating reflection's position on the target:

$$\underline{R}^*(\alpha,\gamma) = \underline{t}^{*\prime} L_T^*(\alpha,\gamma) \tag{5.22}$$

Optimisation cost function is then used to calculate the estimated elevation α^* and azimuth γ^* angles of the heliostat:

$$f^*(\alpha,\gamma) = ||\underline{R}^*(\alpha,\gamma) - \underline{T}^{*\prime}(\alpha,\gamma)|| \tag{5.23}$$

$$\alpha^{*\prime} = \alpha^* + \epsilon_\alpha^* \tag{5.24}$$

$$\gamma^{*\prime} = \gamma^* + \epsilon_\gamma^* \tag{5.25}$$

5.4 Testing accuracy with given altitude and azimuth angles

The following section calculates the reflection position on the target with given calibration parameters and other input values. The schematic of the program can be followed in figure 5.1.

The true displaced target position $\underline{T}$ calculated by using the true target position $\underline{T}$ and adding the true displacement of the heliostat $\underline{\delta}$:

$$\underline{T}' = \underline{T} + \underline{\delta} \tag{5.26}$$

Calculating the bias elevation α' and azimuth γ':

$$\alpha' = \alpha^{*\prime} - \epsilon_\alpha \tag{5.27}$$

$$\gamma' = \gamma^{*\prime} - \epsilon_\gamma \tag{5.28}$$

Calculating the final rotational matrix $\mathbf{\Phi}$ from the rotational matrix around the northern $\mathbf{R}_N$ and eastern $\mathbf{R}_E$ axes caused by the tilt μ:

$$\mathbf{R}_E = \begin{bmatrix} 1 & 0 & 0 \\ 0 & \cos(\mu_E) & -\sin(\mu_E) \\ 0 & \sin(\mu_E) & \cos(\mu_E) \end{bmatrix} \tag{5.29}$$

$$\mathbf{R}_N = \begin{bmatrix} \cos(\mu_N) & 0 & \sin(\mu_N) \\ 0 & 1 & 0 \\ -\sin(\mu_N) & 0 & \cos(\mu_N) \end{bmatrix} \tag{5.30}$$

$$\mathbf{\Phi} = \mathbf{R}_E \mathbf{R}_N \tag{5.31}$$

Calculating the mechanical arm's angle ζ_a and radius ζ_r:

$$\zeta_a = \tan\left(\frac{\zeta_2}{\zeta_1}\right) \tag{5.32}$$

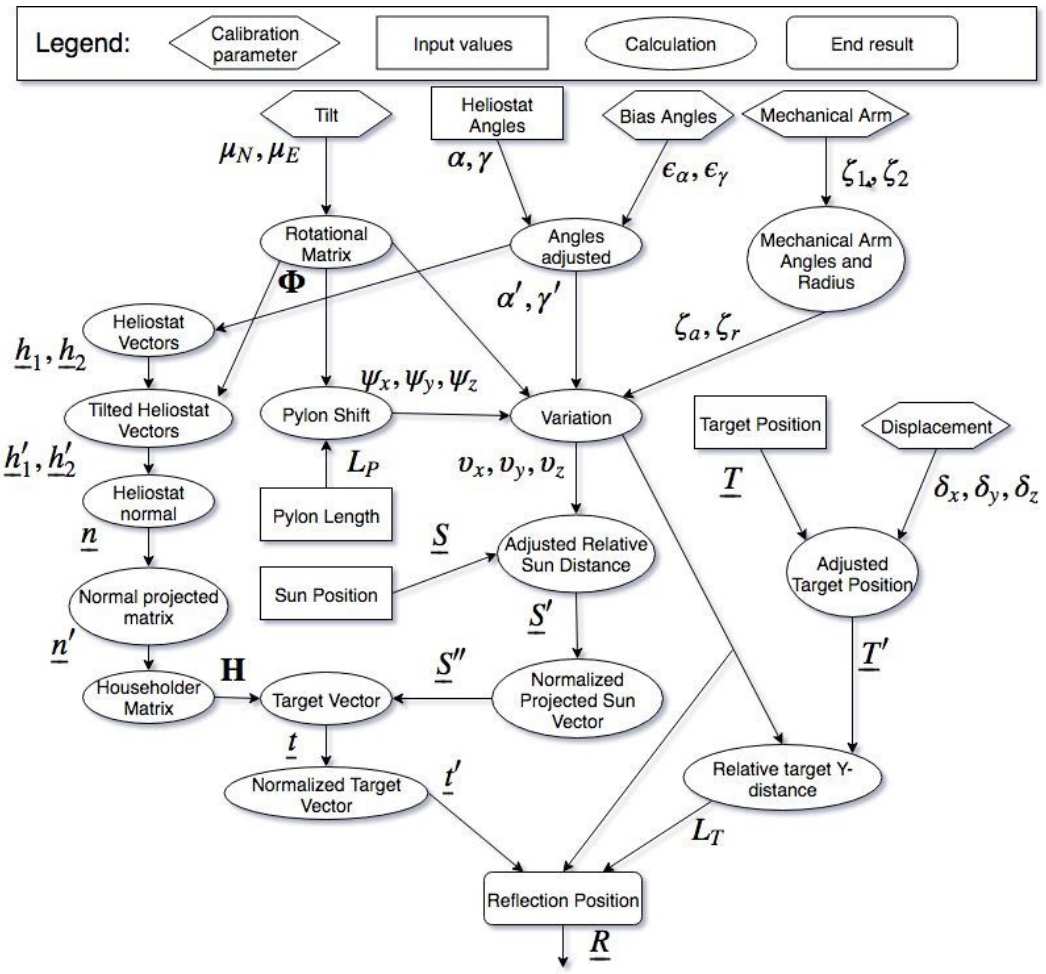

Figure 5.1: Schematic representation of code

$$\zeta_r = ||\zeta|| \tag{5.33}$$

Pylon shift $\underline{\psi}$ cause by the tilt μ of the pylon and the pylon's length L_P:

$$\underline{\psi} = \mathbf{\Phi} \begin{bmatrix} 0 \\ 0 \\ L_P \end{bmatrix} - \begin{bmatrix} 0 \\ 0 \\ L_P \end{bmatrix} \tag{5.34}$$

Variation between the centre of the mirror and the pylon's reference point caused by the angles of the heliostat's mirror with the mechanical arm and the pylon shift:

$$\underline{v} = \mathbf{\Phi} \begin{bmatrix} \sin(90 - \alpha' - \zeta_a)\zeta_r \sin(\gamma') \\ \sin(90 - \alpha' - \zeta_a)\zeta_r \cos(\gamma') \\ \cos(90 - \alpha' - \zeta_a)\zeta_r \end{bmatrix} + \underline{\psi} \tag{5.35}$$

Relative sun distance:

$$\underline{s}' = \underline{s} - \underline{v} \tag{5.36}$$

Normalised projected sun vector:

$$\underline{s}'' = -\frac{\underline{s}'}{||\underline{s}'||} \tag{5.37}$$

Calculating the heliostat vectors:

$$\underline{h}_1 = \begin{bmatrix} \cos(\gamma') \\ -\sin(\gamma') \\ 0 \end{bmatrix} \tag{5.38}$$

$$\underline{h}_2 = \begin{bmatrix} -\sin(\gamma')sin(\alpha') \\ -\cos(\gamma')sin(\alpha') \\ \cos(\alpha') \end{bmatrix} \tag{5.39}$$

Adjusting for tilt:

$$\underline{h}_1' = \mathbf{\Phi}\underline{h}_1 \tag{5.40}$$

$$\underline{h}_2' = \mathbf{\Phi}\underline{h}_2 \tag{5.41}$$

Calculating Normal:

$$\underline{n} = \underline{h}_1' \times \underline{h}_2' \tag{5.42}$$

Calculating the normal projection matrix:

$$\mathbf{P}_n = \frac{\underline{n}\ \underline{n}^T}{\underline{n}^T\underline{n}} = \underline{n}(\underline{n}^T\underline{n})^{-1}\underline{n}^T \tag{5.43}$$

Calculating the householder matrix:

$$\mathbf{H} = (\mathbf{I} - 2\ \mathbf{P}_n) \tag{5.44}$$

Target Vector:

$$\underline{t} = \mathbf{H}\underline{s}'' \tag{5.45}$$

The normalised target vector:

$$\underline{t}' = \frac{\underline{t}}{||\underline{t}||} \tag{5.46}$$

Calculating relative target distance:

$$L_T = \frac{T_y' - \upsilon_y}{t_y'} \tag{5.47}$$

Calculating target reflection position:

$$\underline{R} = \underline{t}' L_T + \underline{\upsilon} \tag{5.48}$$

Cost function:

$$f = ||\underline{R} - \underline{T}'|| \tag{5.49}$$

5.5 Constraints

For the position of the target a 50 mm displacement north, east, south, west, up and down was provided creating a range of 100 mm - far greater than that of the expected accuracy with a safety factor of 1.66.

Assuming a digital leveller is used during installation to ensure that the pylon is perpendicular would not guarantee that the pylon does not tilt due to ground erosion or other factors that could cause the ground to give away under the weight. Thus, a tilt of 2.5 degrees was given for both the northern and eastern axis in the clockwise and anti-clockwise directions.

The elevation and the azimuth angles of the facet were both given a 10 degree uncertainty in both directions.

Considering the limitations of error in the facet's normal direction, the error was limited to 10 millimetres inward or outward to compensate for the bulge. But due to the greater range of possible centres of the concave mirror, combined with the attachment height of the mechanical arm to the facet, a 100 millimetre distance was created for upward and downward movement to ensure it will be compensated for.

To the mounted camera displacement on the drone during the flight a 6 mm uncertainty was given in all directions to compensate for possible movement.

5.6 Possible complications inherent with optimization

Multiple solutions are the greatest downfall of all optimisation. One method to ensure that the problem does not have multiple solutions is to run the programme from multiple starting points. These can be random or selected in a grid. But after inspection, it was noticed that this problem did not have multiple solutions, therefore, it was not necessary to test for each heliostat.

With real-world tests there is always the possibility that the data collected, and the parameters estimated were correctly guessed purely by chance. This could cause the data to give a false interpretation of what actually happened, or what might be true. But when using a computer to optimise the system and to minimise the cost function it can never guess the correct parameters purely by chance: it would always select the parameters that minimised the cost function the most out of all the possible solutions. Therefore, this is not a concern when trying to create something such as a 95 % confidence level graph.

Chapter 6

Simulation

Each heliostat has physical properties with already predefined parameters by which it is described. These parameters were calculated during calibration. Each of these heliostats with specific calculated parameters cause different reflections. Therefore, if these parameters that were calculated were assumed to be the correct parameters, then for a randomly selected day in the year, such as the 10th of October, the heliostat's angles required to track the sun of that day can be calculated. If the required heliostat angles calculated with the optimised parameters of that heliostat were enforced on the real heliostat to reflect the sun onto the target, then the reflection of the sun could be observed. Due to the difference between the predefined parameters and calculated parameters the reflection would not hit the target at its centre, but it would rather cause a spread reflection.

The difference in radius between the zero of the target and its reflection can be calculated. Since the sun is at different positions in the morning to those in the afternoon, as well as the differences in position between winter and summer, many of the sun's positions need to be tested. To ensure a degree of uniformity throughout all the tests it was decided that the 10th day of each month has to be tested. But since some days are shorter than others it was also decided to collect only 35 observations per day. That comes down to one observation every 20 minutes.

6.1 Validation of simulation program

Since a new heliostat model was generated, and different optimisation equations were set up to generate results, it was necessary to validate the programme to ensure that it was free from coding errors.

Therefore the first confirmation test would implement the use of the sun with zero noise to calibrate the heliostat. To enable the confirmation of validation,

the milliradian error of the reflection on the target throughout the year was calculated for each case of 2, 5, 8, 10, 20, 50, 100, 200 and 240 calibration points as shown in Figure 6.1.

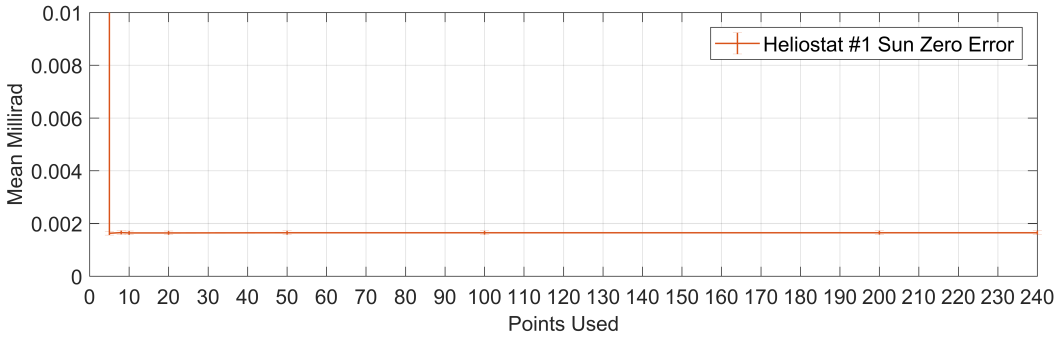

Figure 6.1: Milliradian error with the sun with zero noise in position for simulation code validation

The resulted milliradian error when using the sun was 0.00165 milliradian from 5 points onward. Thus for an ideal system with perfectly known sun positions, the calibration would be able to achieve 0.00165 milliradian due to computer-calculated errors. By comparison the drone would achieve the following as seen in Figure 6.2 for a zero noise system. The reason that the drone achieved worse results than the sun was due to the 10th parameter. This parameter can cause a minor change in the position of the drone, and it influences the final result. However, the milliradian error is still equal or less than 0.005915 milliradian when more than 10 points are used. This confirms that the simulation code is performing adequately. This also shows that it would introduce bias to try and compare the calibration of the sun to that of the drone due to the fact that with zero noise their error in position is not the same.

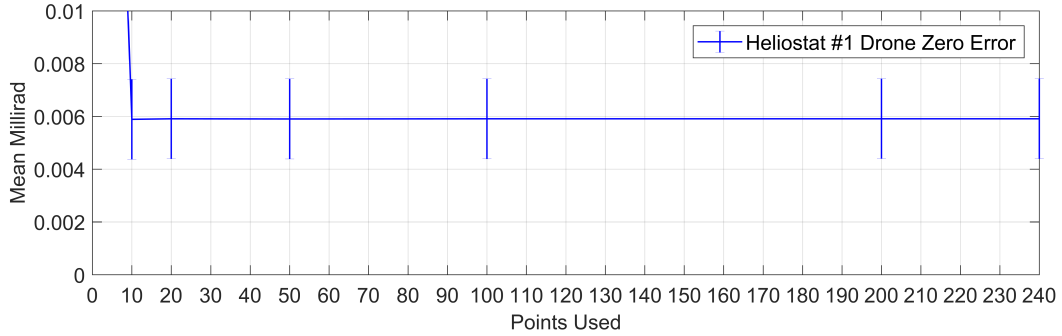

Figure 6.2: Milliradian error on the target with the drone with zero noise in position for simulation code validation

6.2 Test run with sun

The next step is to use the sun to solve all 9 parameters with the error of the sun only being +-0.0003 degrees in its position. This would validate the response of the simulation to noise error introduced into the positions of the sun or drone. These tests incorporated the use of the sun on the 10th of January 2018 to calibrate a predefined heliostat. After these parameters were solved, the reflection of each 10th day of each month of the year was calculated. Firstly the calibration was done using only two points. These points can be seen in Figure 6.3a with the resulting reflection on the target in Figure 6.3b.

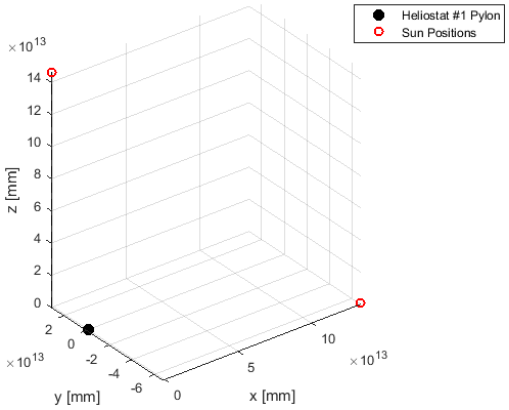

(a) Locations of the 2 calibration points used with the sun on the 10th of January with noise error of +-0.0003 degrees. These points were used to solve Heliostat #1.

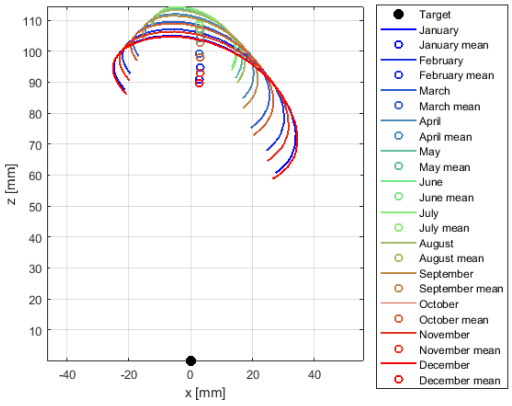

(b) Reflection on target after calibration with 2 points of the sun. The shape, distance and spread give an indication of the performance of the calibration.

Figure 6.3: Heliostat #1 calibrated using 2 points of the sun (a) with the resulting reflection on target (b)

The two points of the sun were used to solve the 9 parameters of the heliostat. However, for a multi-variable equation using two points is far less than the required amount to solve the parameters perfectly, but for the purpose of the research an unrealistic starting amount was chosen to see how the calibration would behave, and it would also create a reference for a worst-case scenario. After the calibration was completed, the reflection of each month was calculated. A graph was generated and colour-coded to distinguish the reflection on the target for each month as shown in Figure 6.3b when a specific heliostat was calibrated with the sun using 2 points.

Figure 6.3b shows the expected trajectory of the reflection of the sun for each month. The pattern is dependent on each specific parameter and therefore

not all the heliostats would cause the same pattern. The size of the spread of the trajectory also influences the efficiency of the heliostat. The closer the reflection is to the centre of the target, the better the concentration of the sun on the target.

The same tests were run with 5, 8, 10, 20, 50, 100, 200 and 240 points. For the purpose of illustrating the results, only an extreme minimum of 2 points, 10 points and a maximum number of points acquired during the day (240) will be shown. The 10 points selected can be seen in Figure 6.4a. These points are also equally spread throughout the day of the 10th of January. The corresponding trajectory of the months in the year is shown in Figure 6.4b.

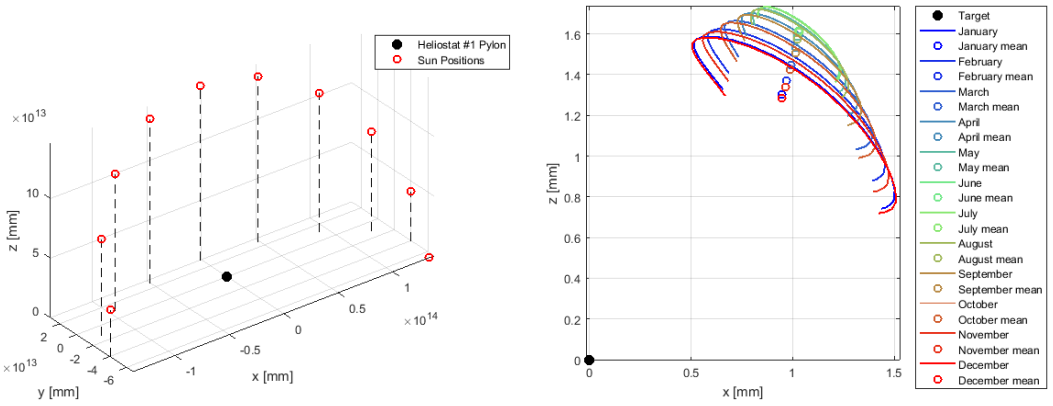

(a) Locations of the 10 calibration points used with the sun on the 10th of January with noise error of +-0.0003 degrees. These points were used to solve Heliostat #1.

(b) Reflection on target after calibration with 10 points of the sun. The shape, distance and spread give an indication of the performance of the calibration.

Figure 6.4: Heliostat #1 calibrated using 10 points of the sun (a) with the resulting reflection on target (b)

With 10 points selected, the 9 parameters can be solved. The reason for using 10 points instead of 9 is due to the fact that the drone uses 10 parameters that requires solving. Figure 6.4b shows the trajectory of the reflection of the sun for the 10th day of each month. To interpolate between each month would not be difficult, but due to the fact that the shape of the reflection stayed consistent, it was deemed unnecessary to calculate the reflection of each single day from sunrise to sunset.

Figure 6.4b shows a significant improvement of the size of the reflection's trajectory as well as the distance from the target centre. It was such a significant improvement that the axis could not be kept for comparison.

The maximum number of 240 points was selected due to the calculated maximum number of drone points that can be collected during one day. It was estimated that roughly for a 12-hour day that every 30 minutes 10 calibration points can be collected. Therefore the sun, which follows an arc trajectory, was divided into 240 calibration points as seen in Figure 6.5a with the corresponding trajectory on the target seen in Figure 6.5b.

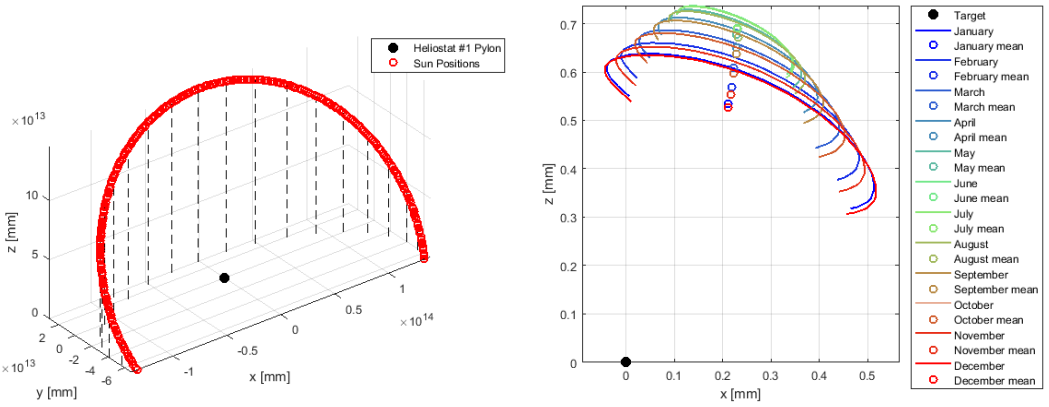

(a) Locations of the 240 calibration points used with the sun on the 10th of January with noise error of +-0.0003 degrees. These points were used to solve Heliostat #1.

(b) Reflection on target after calibration with 240 points of the sun. The shape, distance and spread give an indication of the performance of the calibration.

Figure 6.5: Heliostat #1 calibrated using 240 points of the sun (a) with the resulting reflection on target (b)

6.3 Indication of mean of data

Also, note that these complex reflection lines cannot be described mathematically, and therefore a mean was assigned to each month's line. These means will not always show exactly what happened during each month, but they will enable some comparisons to be made. The mean also gives an indication of the concentration's centre. To demonstrate the complexity of the reflection lines, the figures 6.6a and 6.6b, were chosen to display the different types of reflection lines.

These figures show only a small selection of the varieties of different patterns that can be expected. Since these patterns cannot all be described using one equation, it was decided that the best solution would be to conform to the mean of each reflection. Since the lines were generated by using the 10th day of each month, it can be assumed that these lines are a good representation

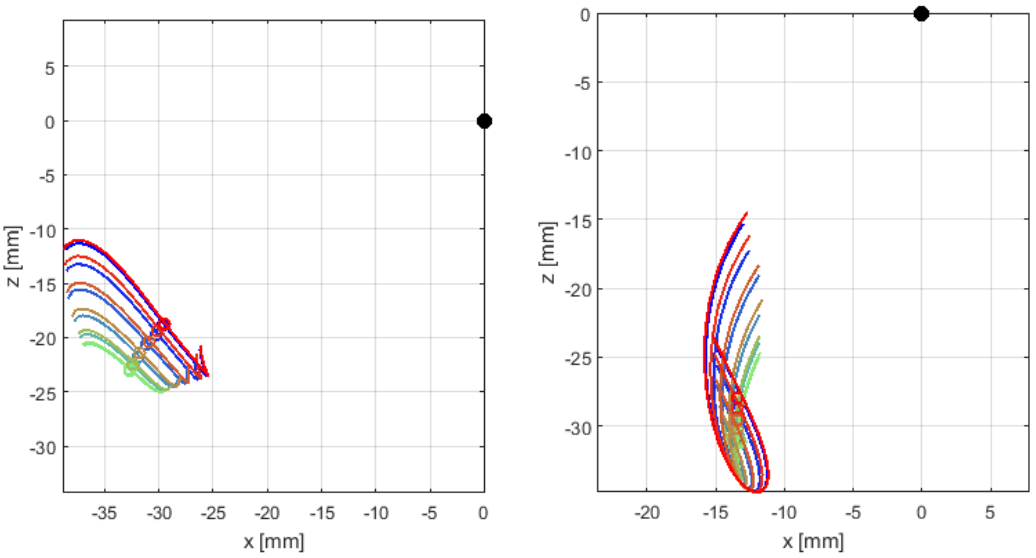

(a) Reflections on the target with 5 calibration points used with the drone

(b) Reflections on the target with 8 calibration points used with the drone

Figure 6.6: Indication of different reflection patterns expected from the same heliostat with different calibrated parameters. These figures should not and cannot be compared, however, they serve the purpose of demonstrating the need for using a mean of the reflection lines.

of what happens throughout the year. It is also important to note that the positions of the January and December lines rejoin, as can be expected with the seasons having gone full circle.

6.4 Simulation results of heliostat #1

The following section will first make use of 1 heliostat and a drone with a distance of 32 metres from the pylon to understand how to represent the data retrieved from the simulation programme. Afterwards, an analysis will be done of the complexity of the data. This will clearly indicate which factors influence the results, such as the noise, or the drone positions used. Thereafter the 9 parameters will be changed one by one to compare the effect of this on the results. Lastly 100 different heliostats will be generated to create a 95 % confidence level graph.

6.4.1 Heliostat #1 detailed review

Comparing the difference between each parameter's optimised value and true value would be one way to present the results. However, for the purpose of this thesis, this will only be shown once, as seen in Table 6.1 for 2, 10 and then when the maximum of 240 points was used. The maximum was calculated

as an approximation of being able to retrieve 10 points every half an hour with the drone. The 10th parameter (Drone offset) is not a parameter that describes the heliostat, however it is shown due to the fact that it influences all 9 parameters calculated using the heliostat. The parameter shows the offset of the camera when taking a picture from the drone.

The reasoning behind not always showing this as a comparable table is that it does not represent how the reflection of the sun would react under these new estimated parameters. To show how well the calibration has performed can be measured by how well the reflection has hit its target. And for each heliostat, each change in parameter has a different effect, therefore knowing the difference between the real and calculated parameter would not be sufficient.

Table 6.1: Parameters estimated using 2, 10 and 240 points of the drone during calibration, compared to the real values set for Heliostat #1.

Parameter	**True**	**2 Points**	**10 Points**	**240 Points**
ζ_1 [mm]	432.500	428.771	440.235	442.295
ζ_2 [mm]	240	271.303	246.513	242.558
T_x [mm]	11000	10977.757	10981.691	10984.489
T_y [mm]	27000	26983.443	26971.171	26969.708
T_z [mm]	4250	4255.782	4252.516	4254.305
ϵ_α [deg]	3	2.887	2.990	2.997
ϵ_γ [deg]	-3	-2.953	-3.001	-3.001
μ_N [deg]	0	-0.084	-0.009	-0.006
μ_E [deg]	0	0.052	0.002	0.006
Drone offset [mm]	0	-0.069	0.997	-0.186

The locations used to calibrate this heliostat relative to the pylon can be seen in Figure 6.7a. To improve on the understanding of the efficiency of the calibration, the following Figure 6.7b was generated using 2 points.

The sun positions will follow the trend of the sun's arc for the 10th of January 2018. However, the drone will not follow any trend, but when the number of calibration points is increased, then the original points are kept, and new points are added to reach the number of required calibration points. This is to ensure that no bias is created when the calibration points are increased.

The number of calibration points was increased to 5 then 8, 10, 20, 50, 100, 200 and finally to 240. The 10 calibration points used can be seen in Figure 6.8a. For each number of calibration points, the reflection lines of that specific heliostat were plotted for a year. Each time the shape of the reflection lines

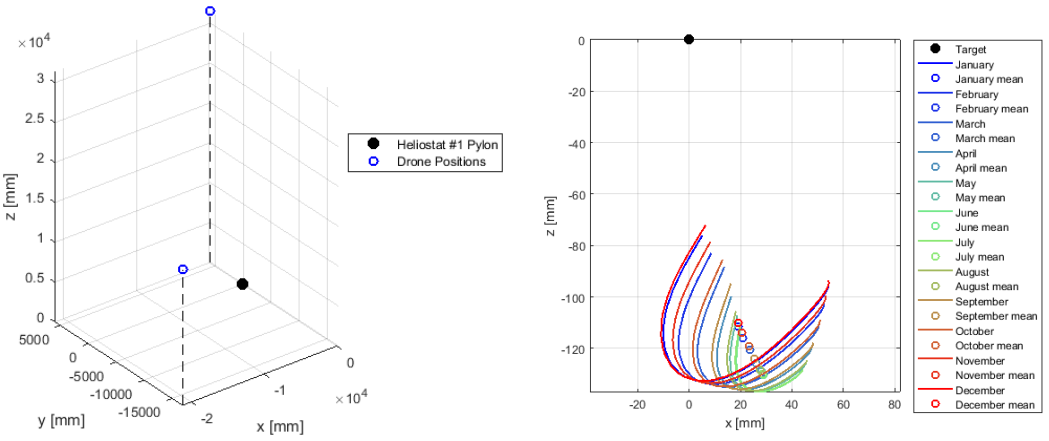

(a) Locations of the 2 calibration points used with the drone with noise error corresponding to the STDev of the logged RTK-GPS data. These points were used to solve Heliostat #1.

(b) Reflection on target after calibration with 2 points of the drone. The shape, distance and spread give an indication of the performance of the calibration.

Figure 6.7: Heliostat #1 calibrated using 2 points of the drone (a) with the resulting reflection on target (b)

would change in an unpredictable matter as seen in Figure 6.8b.

These figures show the exact same heliostat #1 being calibrated using 10 points. This caused the calculated parameters to change that in turn changed the shape of the reflection on the target.

When the calibration is taken to a more extreme example using 240 calibration points as seen in Figure 6.9a, then the effect on the reflection pattern can be seen in Figure 6.9b.

Also observe the shape that is formed when this increased number of calibration points is used. For the sun, the arc can clearly be seen in Figure 6.5a. The drone has a dome-like shape around the centre of the pylon in Figure 6.9a. The range of the drone's points extends far beyond that which the sun will ever reach or what the heliostat possibly needs to do. But this creates the opportunity to calibrate up to the mechanical limits of the heliostat, and that could possibly increase the overall accuracy of the heliostat.

Summing up these figures in the most effective way would be to compare the milliradian error in Figure 6.10. When looking at the shape of the lines created by the drones, then only when using an irrational number of calibration points, in this case, anything below 10, these lines curved and had a bias towards some months rather than towards others. But when observing a ra-

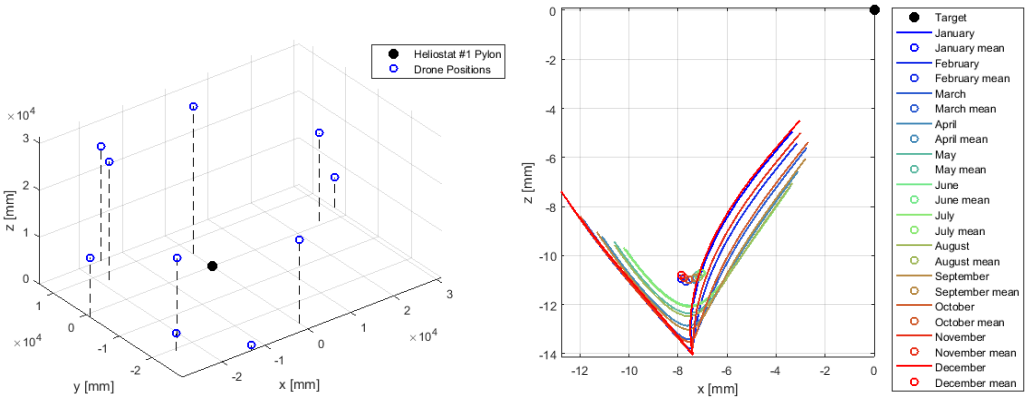

(a) Locations of the 10 calibration points used with the drone with noise error corresponding to the STDev of the logged RTK-GPS data. The previous two points were kept, and 8 more points were selected.

(b) Reflection on target after calibration with 10 points of the drone. The shape, distance and spread give an indication of the performance of the calibration.

Figure 6.8: Heliostat #1 calibrated using 10 points of the drone (a) with the resulting reflection on target (b).

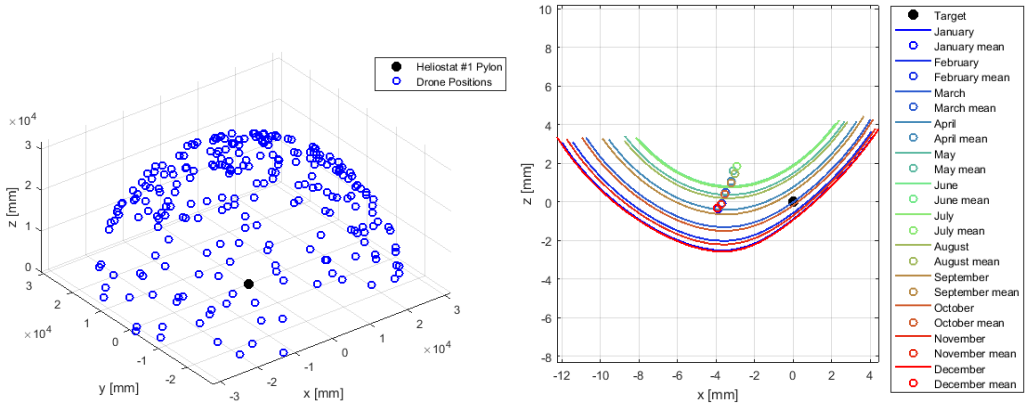

(a) Locations of the 240 calibration points used with the drone

(b) Reflection onto target with calibration with 240 points using the drone

Figure 6.9: Heliostat #1 calibrated using 240 points of the drone (a) with the resulting reflection on target (b).

tional number of calibration points such as 10, then you can observe a straight line caused by the unbiased behaviour in a particular month. Therefore, when using fewer points to calibrate, you could expect irrational, unfamiliar patterns such as when using 2 points of the sun - there is an improved performance on the second month, but it declined sharply after that. That only emphasises the fact that using more calibration points would be beneficial to the system. However, it can also be noted that the sun of 200 calibration points performed

better than 240 calibration points when using the sun. This is not an unlikely occurrence. The reason for this is that the summation of errors created by the uncertainty of the sun's position was not diminished when using more calibration points. Therefore, when running calibration with fewer points you might not calibrate the system correctly, but running with too many points you might run the risk of compiling errors.

The effect of increasing the number of calibration points can also clearly be observed in Figure 6.10. Here the maximum and minimum milliradian error is displayed as well to indicate the range. In this figure, it is very clear that the drone calibrated the heliostat to perform within 1 milliradian error. The drone already stabilized after 5 points were used. However, this is not always the case in these calibrations. There is a possibility that using the drone with different heliostat parameters or different drone positions would be more beneficial than with the selected heliostat parameters, and therefore this was also investigated.

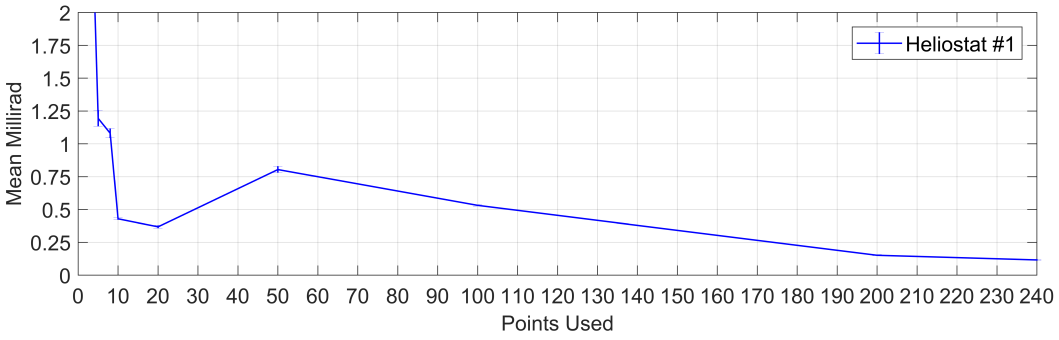

Figure 6.10: The mean milliradian error for heliostat #1 with estimated calibration parameters for 2, 5, 8, 10, 20, 50, 100, 200 and 240 points.

To give a clearer idea of the data collected from the heliostat, a more logical value such as the radius in millimetres would be easier to understand, but if the distance from the heliostat to the target is to change, then it is very difficult to compare one heliostat's performance with another's: a heliostat that was 10 metres away from the target an error of 1 metre means it was off by 5.7 degrees or 99.669 milliradians. While on a heliostat at a distance of 30 metres from the target, with the same error of 1 metre on the target means it was off by 1.909 degrees or 33.321 milliradians. Comparing the milliradians error on the target from the heliostat would ensure that a fair comparison can be made. It will also ensure that there is no bias in favour of the heliostats that are closer to the target, and that the heliostats will be compared on their milliradians accuracy as seen in Table 6.2.

Table 6.2: The mean of the year's milliradian error calculated by each month's reflection on the target.

Points used	Mean milliradian error
2	4.246
10	0.429
240	0.116

6.4.2 Changing the drone points used for calibration

It must be known whether the drone positions used to calibrate the exact same heliostat affects the end result. Therefore, the same heliostat #1 as seen before was calibrated, but this time using different drone points with new noise on each point. All 240 drone positions changed, but due to the high number of drone positions, a specific case using 10 calibration points was used to demonstrate the new drone locations as well as the final resulting reflection on the target as seen in Figure 6.11a and 6.11b.

Figure 6.11b kept the existing results of heliostat #1 for comparison purposes. It is clear that changing the drone positions for calibration has an effect on the pattern of the reflection and the distance from the targets zero. For this specific comparison of 10 points the difference is not significant in the milliradian error. However it can be seen in Figure 6.12 that this trend was not kept.

From this figure it can be seen that changing the drone positions had a greater influence after using 10 calibration points, but by the time 240 points have been reached, the end result was very similar again. This raises the question of whether the result was truly dependent on the position that was chosen, or whether the noise of each of the new points chosen had a greater influence.

It must be remembered that with simulation reaching the mechanical limits of a heliostat, movements do not improve the calibration, but in practice it might. For example, a simulation inserts the exact altitude and azimuth bias to the parameters. Making use of a greater range in the points used with the drone increases the range of what the heliostat should have orientated towards. Therefore, it reaches all the possible combinations of the mechanical limits of the heliostat, while the sun only follows a specific arc that requires only a certain range of the mechanical abilities of the heliostat. It is logical that when a greater range of points is used, then the interpolation error of the heliostat's parameters would be more accurate than when interpolating between a small change in mechanical parameters.

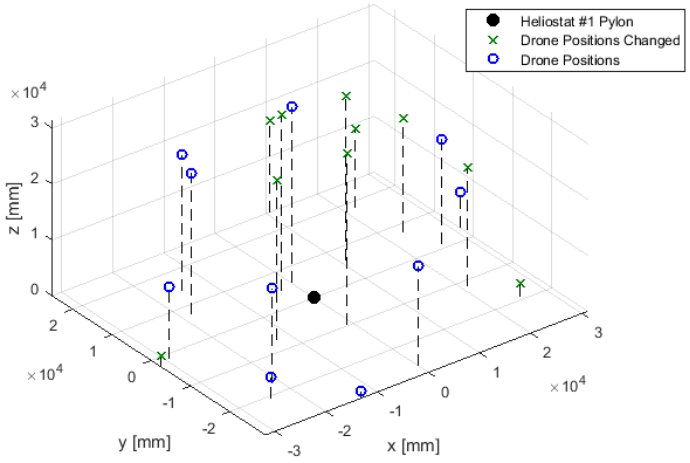

(a) Locations of the new drone positions used to calibrate the heliostat #1. These points were also randomly generated and an error with the same STDev was induced onto the points as the one that was collected using the data from the RTK-GPS setup.

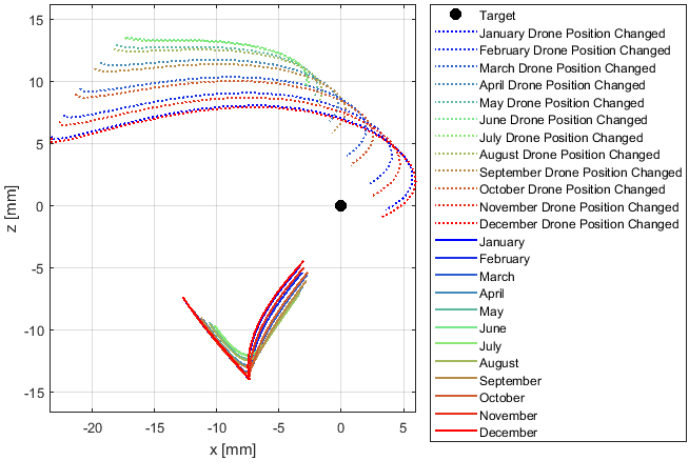

(b) Reflections on the target with 10 calibration points used with the new drone positions with the original case result for comparison. This figure shows a complete change in shape and size that is a result of different calibrated parameters for the exact same heliostat #1.

Figure 6.11: Effect of changing the drone points used for calibration of heliostat #1. (a) Shows new drone postions. (b) Shows new reflection pattern.

6.4.3 Sensitivity to randomly generated noise

In the previous sub-section the question arose of whether the error in drone positions was the actual source of the improvement of the calibration results, or not. To test this thoroughly two scenarios require testing: testing dependency on specific noise and testing dependency on new noise.

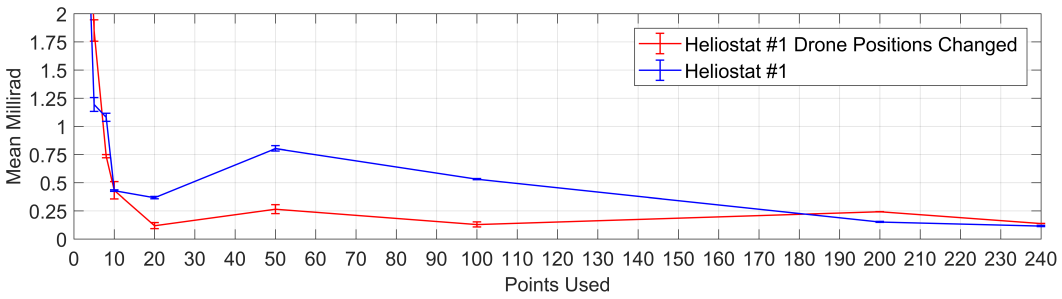

Figure 6.12: Comparison between using different drone points for calibration. The error does not follow the same trend, which shows that the change in position affected the results. However, it is not known if the change in results was solely due to the new positions, or to the noise of those new positions.

6.4.3.1 Testing dependency on specific noise

To prove or disprove the dependency on a specific noise can be done by using the new drone positions generated as seen in Figure 6.11b, but instead of adding different noise to the positions, rather by adding the exact same noise as what was generated in the original case. This would shed light on the first concern of whether the noise was the only factor for the behaviour of the results by comparing the milliradian error. If the error is exactly the same as in the original case, then it would confirm that the error was caused by the noise and not by the positions which were chosen. However, as with the milliradian error observed in Figure 6.13 the values are clearly not the same.

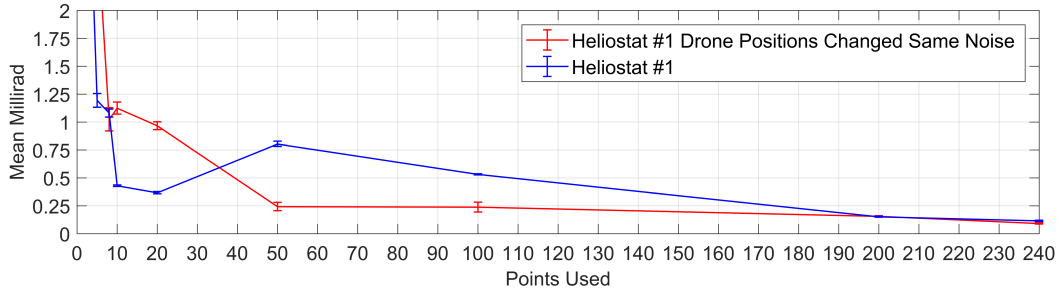

Figure 6.13: Testing dependency on specific noise by using the newly generated drone positions in combination with the original noise added to the drone positions. Seeing that the error of the new case is not the same, it can be said that the error is not solely dependent on the specific noise on the drone positions.

Point number 1 in the original and point number 1 that was used in the new case had the exact same noise error in the position and also the same with each

one of the 240 new points. This means that the behaviour of the milliradian error is not solely dependent on the noise that is used on the points.

6.4.3.2 Testing dependency on new noise

Thereafter, to prove or disprove that the milliradian error was dependent on the new positions rather than on the noise, the exact same positions were chosen as in the original case, but the noise generated on each point was changed to see if the milliradian error would be exactly the same. If the milliradian error were the same, then it could be said that the error was dependent on the drone positions, because new noise did not change the error.

This error was still confined to the STDev of the RTK-GPS logged data, but each point received a different error. To confirm that the exact same positions were chosen, all 240 points were plotted with the original points chosen for the calibration of heliostat #1 as seen in Figure 6.14a. The selection for plotting the reflection results was chosen to be 10 calibration points again, as seen in Figure 6.14b and this was compared again with the original results.
For the 10 calibration points it can be seen that the shape and distance to the centre of the target have changed. This confirms that the parameters were completely different, and because the shape is not similar, it means the ratio between the parameters' differences from ideal was not the same as in the original calibration. It can be noted, however, that due to the fact that the reflection lines are much closer to the centre of the target, that with this new noise the results seemed to improve, and that is confirmed in Figure 6.15.

It is clear that although the exact same points were used, that in some cases the results improved, such as in the case of 50 calibration points. However, due to the fact that the milliradian error did not follow the exact same path or trend it can be said that the positions of the drone chosen were not the sole reason for the improvement of the calibration.

6.4.4 Multi-start extreme case for Heliostat #1

It was stated that the noise was not the sole reason for the improvement in the milliradian error. It was also stated that the drone positions used were not the sole reason either for the improvement of the milliradian error. To ensure that all possible factors influencing the milliradian error were checked, the possibility that a local minimum was the cause of the error should be investigated.

To do this the easiest method is to increase the multiple start from 100 to 1000. If the milliradian error improves, then it means that the absolute minimum was not obtained in the previous iteration of the same case. However, Figure

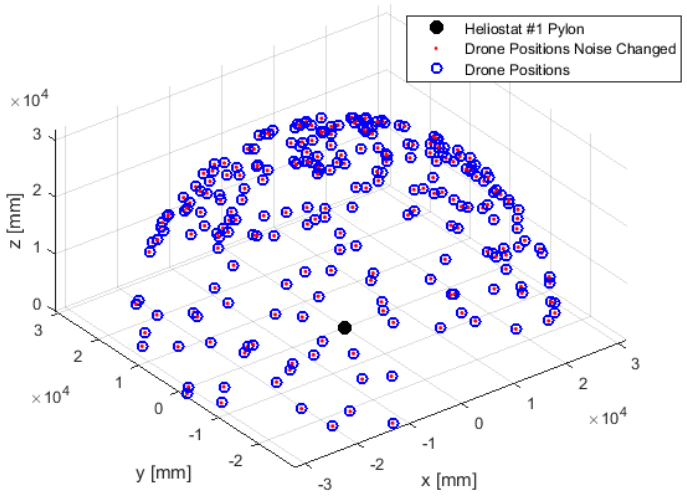

(a) Locations of the new drone positions used to calibrate the same heliostat with new noise

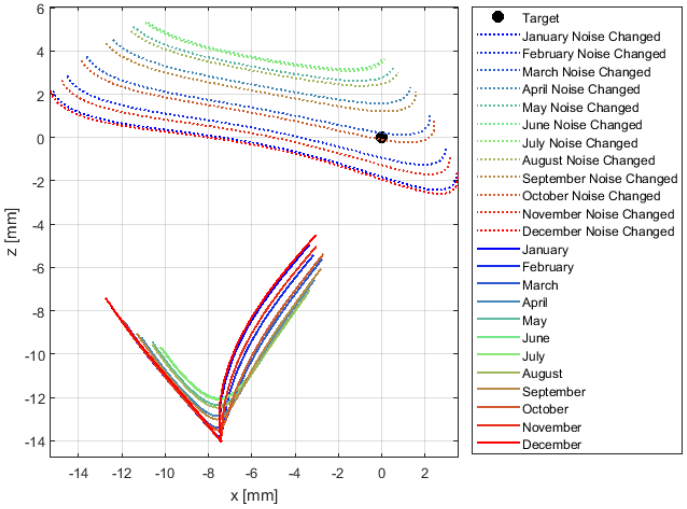

(b) Reflections on the target with 10 calibration points used with the drone

Figure 6.14: Identifying the effect of changing the noise of the selected drone points

6.16 shows almost identical solutions when the final result is compared.This confirms that the source of the errors is not due to the programme running into local minimum solutions. Thus, all results can confidently be seen as the absolute minimum solution for each problem, and that the errors were dependent on the combination of drone position and noise error. Some noise errors increase the milliradian error more when added to certain drone positions rather than other drone positions.

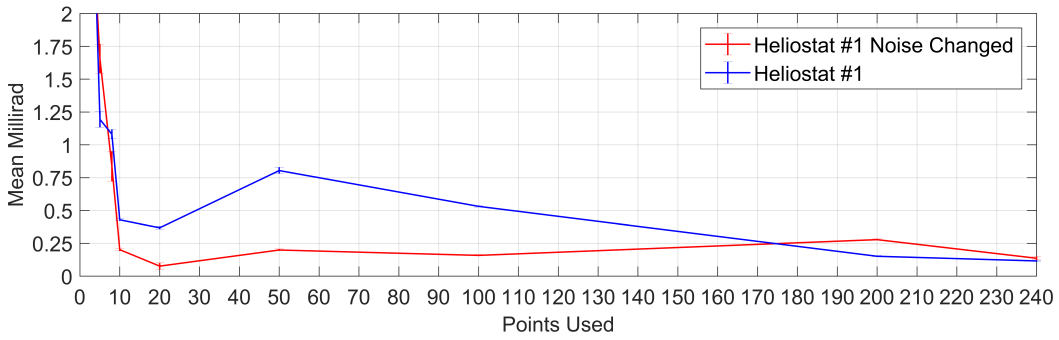

Figure 6.15: Comparison between calibrating heliostat #1 with different noise on each calibration point.

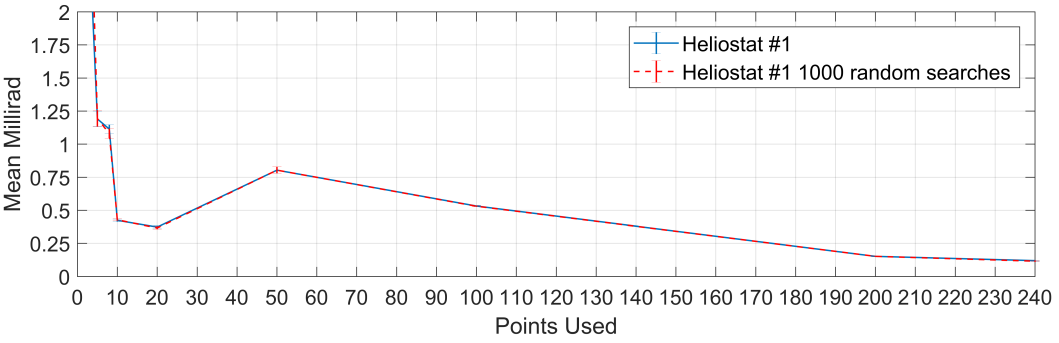

Figure 6.16: Using the same drone positions and the same errors in each position, but during all optimisation procedures 1000 multiple starts were tested before selecting the best solution.

6.4.5 Predicting the result of heliostat #1

Due to the sensitivity of chosen drone positions in combination with noise generated, the single heliostat was calibrated 100 times using 100 different sets of drone positions and noise errors. The resulting Figure 6.17 shows the mean and the standard deviation of the results obtained from the 100 solutions.

6.5 Simulation results for 100 different heliostats

Knowing that the performance of a specific heliostat lies between a certain range shows progress, but what is needed is to be able to predict the performance of any heliostats on the field. Therefore 100 different heliostats should be tested. However, it should first be tested whether certain parameters calibrate with more difficulty than others do.
The following tests will still be using a drone that is located 32 metres away

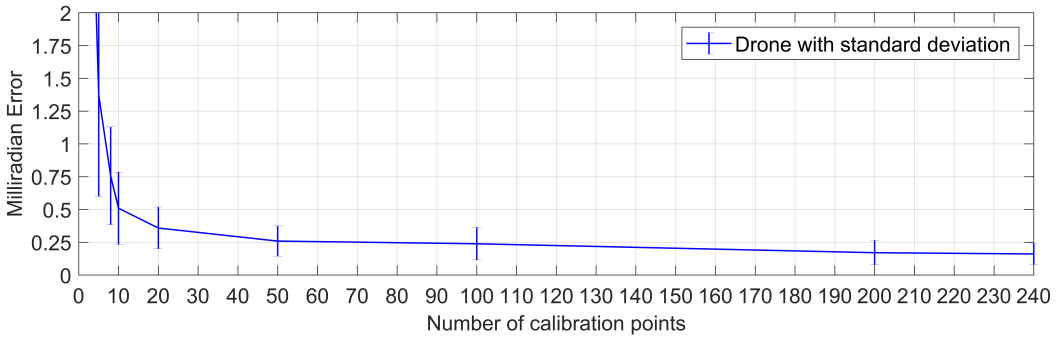

Figure 6.17: The mean milliradian error of heliostat #1 with the standard deviation of 100 tested solutions.

from the pylon.

6.5.1 Comparing a single change in model parameters of heliostat #1

The objective was to prove that some parameters are not more sensitive than others are, or that these would cause the calibration to fail. Therefore it was decided to keep all the parameters of the heliostat constant, and from there only one of the possible 9 parameters was changed. Finally, then all those parameters were changed to previously selected values to generate a completely new heliostat #11 (All parameters changed) as seen in Table 6.3.

Table 6.3: True parameters for Heliostat #1. As well as the true parameter values for the changed heliostat.

Parameter	**Heliostat #1**	**All parameters changed**
ζ_1 [mm]	432.500	300
ζ_2 [mm]	240	300
T_x [mm]	11000	-1000
T_y [mm]	27000	7000
T_z [mm]	4250	3000
ϵ_α [deg]	3	-0.500
ϵ_γ [deg]	-3	1
μ_N [deg]	0	-1
μ_E [deg]	0	1.5

It was decided only to show the end result of the mean milliradian error, due to the fact that it summarises all the information that has been gathered. This can be seen in Figure 6.18.

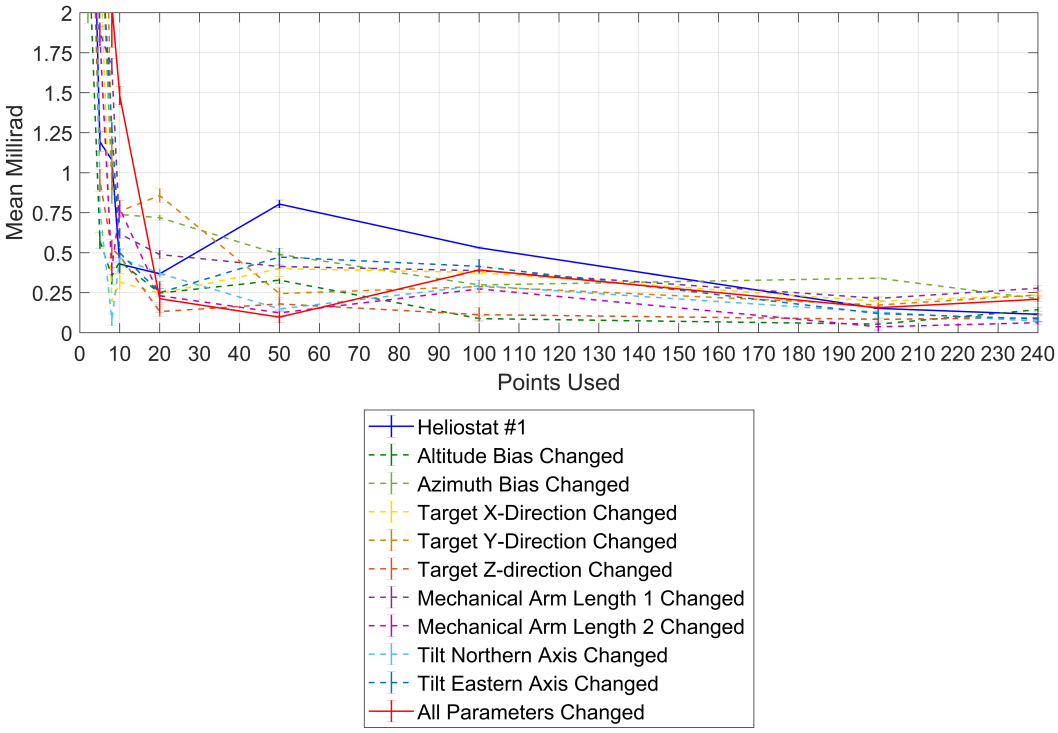

Figure 6.18: Comparison between changing one parameter of heliostat #1 at a time and changing every parameter at once.

Of the 12 heliostats each heliostat used different drone positions with different noise, because due to the changes in parameters of the heliostat these positions could not be kept constant. Because of this, it is difficult to compare these heliostats and to suggest that certain heliostats performed better overall than others did. However, it can be seen that that they all decreased in error from the starting point of 2 calibration points to 240.

During some calibrations an increase in the heliostats milliradian error was present: for example, from 50 to 100 calibration points for the heliostat with all the parameters changed. From the previous section it was derived that the error was dependent on the noise error in combination with the new drone positions added for the calibration. Therefore, it can be said that the increase in errors was only because of the added points position and noise. Therefore, for the chosen example, it can be said that most of these 50 added points were bad points that changed the global minimum of the optimisation problem that effectively influenced the calibration parameters resulting in an increase in milliradian error.

As confirmation for this it can also be noted that during each increase of calibration points selected, the previous calibrated parameters were also a starting point for the multiple-start solutions. Therefore, due to the fact that the pre-

vious solution no longer was the optimised solution, it emphasised that the global minimum of the optimisation changed due to the added points.

Added evidence for confirmation of this would be to see the amount of the increase of milliradian error from one calibration number to another. When observing the original case for heliostat #1 a dramatic increase was seen in milliradian error from 20 calibration points to 50. Thus 60 % of the total calibration points were new drone points that influenced global minimum, and effectively the milliradian error. When comparing it to the increase in milliradian error of the heliostat with all parameters changed from 50 calibration points to 100 points, the error is significantly smaller. This would be due to the fact that only 50 % of the points were new points, but also out of the 50 new drone positions a smaller number of them were badly selected points. When looking at the increase in milliradian error for the same heliostat from 200 to 240 calibration points, it is much smaller. Only 16 % of the total calibration points were new, but even then they can increase the milliradian error if all 40 new drone positions were bad points.

So the increase in milliradian error from using a specific number of calibration points to another is dependent on the ratio of the increase in the number of calibration points, as well as how many of the newly selected calibration points are bad points.

6.5.2 95 % Confidence level graph

In order to create the 95 % confidence graph, a Monte Carlo simulation was generated. In this, all 10 variables were changed with random values within a range that would create a reasonable heliostat for a small-scale heliostat plant.

A side objective is to see if there is any correlation between the parameters chosen and their performance. Due to the high number of parameters, it was decided to confine the investigation to a maximum of 3 parameters at a time, and to group them together with corresponding parameters.

It was also decided to group the data in 3 categories: for the best performing, mid-performing and worst performing. The selection was dependent on the mean of the milliradian error of the heliostat from 10 and 240 calibration points. The behaviour of the error from 2 to 8 calibration points could possibly be irrational, due to the fact that there are 10 parameters, and a recommended value of 10 calibration points should be selected for a rational result. Therefore, the performance of a specific heliostat was only judged on the mean of its performance from 10 to 240 calibration points.

The data was thus divided into 3 categories, best, mid and worst. To start

with, the randomly generated locations of the heliostat are shown in Figure 6.19. Figure 6.19 shows no clear correlation between the milliradian performance and the location of the points.

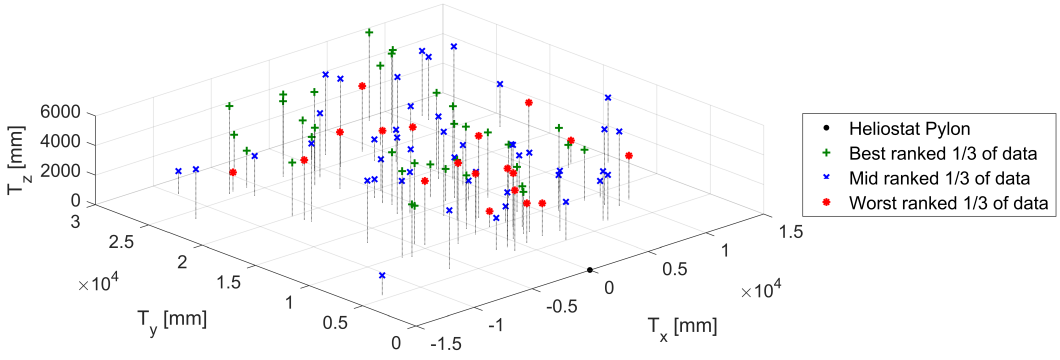

Figure 6.19: Locations of randomly generated heliostats. This figure shows no clear grouping of performance due to the locations selected. It is still possible that there is some correlation in a higher dimension between other parameters.

There are no isolated or grouped points. The bias angles generated for these heliostats are shown in Figure 6.20. The fact that many of the poorly performing heliostats were on the outer rim of the selection range would be a good enough reason to say that extreme bias angles influence the milliradian error. However, there are so many best- ranking points as well right next to those points. Therefore, it can be deduced that there is no correlation between the biased angles and milliradian error.

The tilt for these randomly generated heliostats can be seen in Figure 6.21. The spread of good-, mid- and worst-performing heliostats is scattered again and no distinctive grouping is apparent on the two-dimensional plane. Thus, the combination of tilts does not show any correlation to the milliradian error. The length of the mechanical arm that the heliostat rotates with can be seen in Figure 6.22. The mechanical arm also shows no clear correlation between the two mechanical arm lengths and the milliradian error.

Out of the 100 heliostats generated the following milliradian error between selected intervals was counted as seen in Figure 6.23. This figure shows a clear performance increase when a higher number of calibration points were used. It can be seen that 86 % of the heliostats gave a resulting mean milliradian error of below 0.3 milliradian. And that the maximum milliradian obtained when using 240 points was below 0.6 milliradian.

After these tests were performed, it was possible to generate a 95 % confidence level graph that can predict the performance of a newly generated heliostat

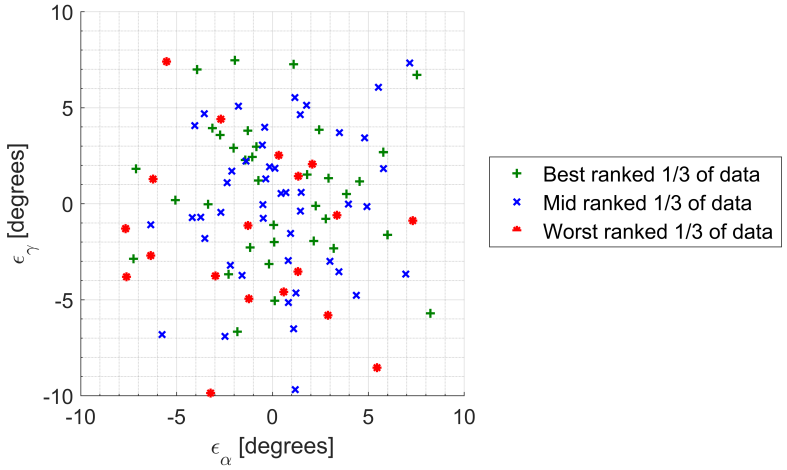

Figure 6.20: The bias in angles of randomly generated heliostats. This figure shows no clear grouping of performance due to the two bias angles selected. Due to the high number of parameters it might be possible that there would be a correlation between some higher dimensional selection of parameters.

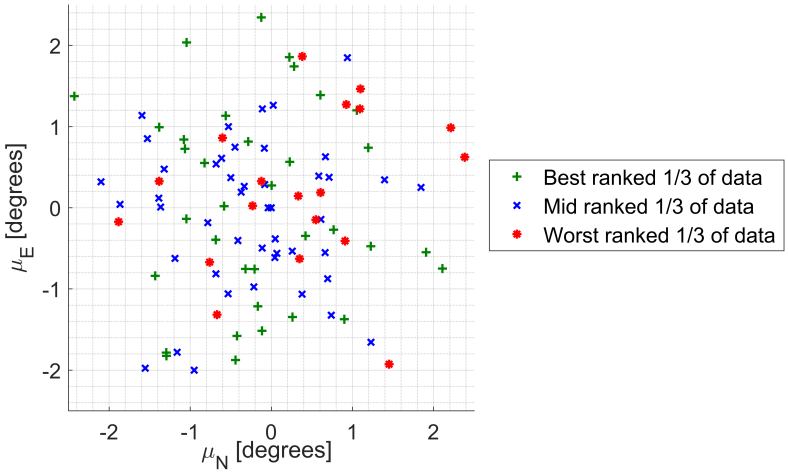

Figure 6.21: Tilt of pylons of randomly generated heliostats. This figure shows no clear grouping of performance due to the two tilt angles selected. Due to the high number of parameters it might be possible that there would be a correlation between some higher dimensional selection of parameters.

when using a selected number of calibration points as seen in Figure 6.24.

6.6 Prediction of milliradian error

It was seen in the previous section that a 95 % confidence level graph can be generated to estimate the possible milliradian performance of a heliostat cali-

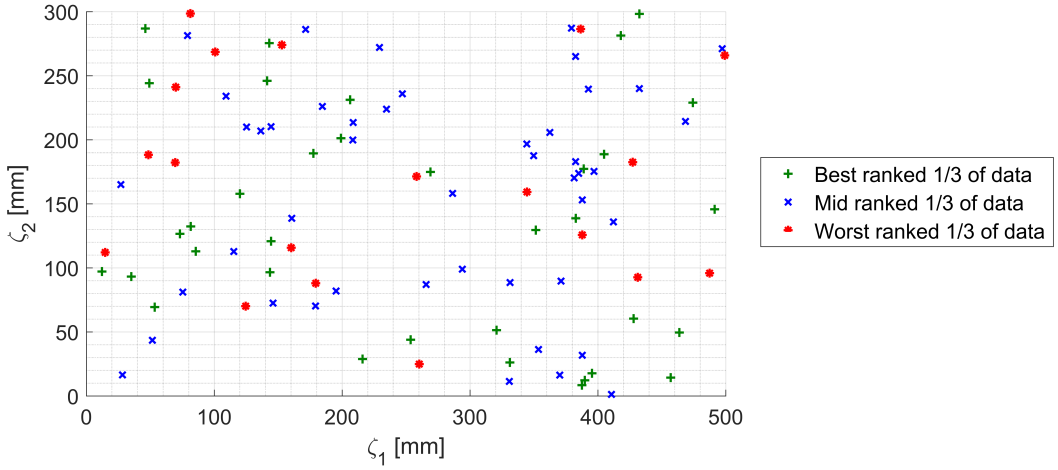

Figure 6.22: Mechanical arm length of randomly generated heliostats. This figure shows no clear grouping of performance due to the two mechanical arm lengths selected. Due to the high number of parameters it might be possible that there would be a correlation between some higher dimensional selection of parameters.

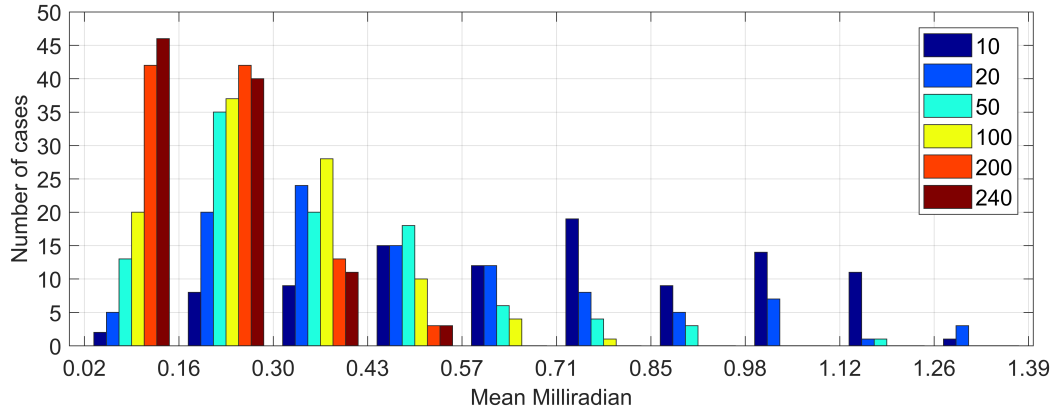

Figure 6.23: Histogram of mean milliradian error for the 100 cases. The spread of the probability can already be seen as when using 10 calibration points compared to using 240 calibration points.

brated by the drone. However, it was stated that these results were generated using a drone that is 32 meters away from the pylon.

The milliradian error prediction is on the noise of the RTK-GPS within combination of the specific drone location. However, it can be assumed that the RTK-GPS noise range will be consistent for any drone distance. With this assumption the noise-to-distance ratio of the drone can increase or decrease depending on the distance of the drone to the pylon. Theoretically increasing the radius of the drone would decrease the error seen by the heliostat, because

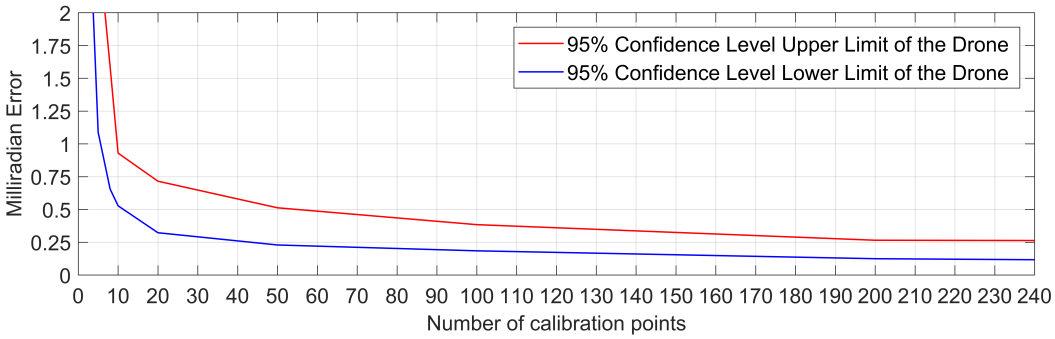

Figure 6.24: The 95 % confidence level graph generated by using 100 random heliostats each with different parameters. These parameters were confined to a logical set of ranges to simulate a small-scale heliostat plant. The drone radius from the pylon was set to a fixed value of 32 metres.

the error seen by the heliostat is that of an angle and not of displacement. Therefore it can be shown and simulated with increased drone radius from the pylon that the predicted upper and lower boundary of the 95 % confidence level graph improves, as seen in Figure 6.25.

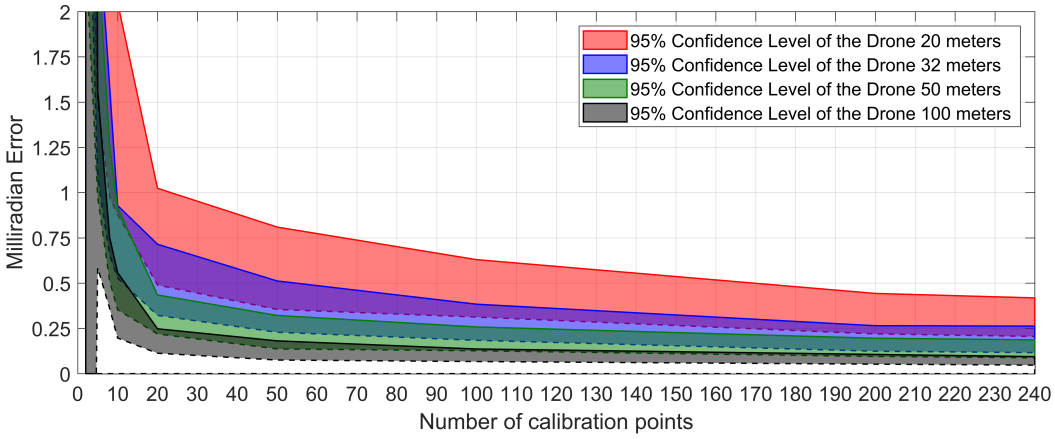

Figure 6.25: 95 % confidence level upper-limit prediction of milliradian error for various drone distances. The upper- and lower-limit would decline as the distance of the drone is increased due to the radius-to-noise ratio increasing, which reduces the uncertainty of the milliradian error.

Chapter 7

Conclusion

In this thesis the objective was to investigate the theoretical feasibility of calibrating heliostats using a drone. Before that could be done, it was first necessary to show that it was possible to identify heliostats using a camera. This was shown to be possible in Chapter 3.1. This resulted in being able to identify each heliostat on the field by isolating the properties of a colour image that could isolate the heliostats. It was possible also to identify the centre of each heliostat's concave mirror from that image.

However, the accuracy of the identified center should be further improved because it was assumed to be perfect for simulation purposes. For practical applications proper investigation should be held on how to accurately pinpoint the centre of the heliostat from the video footage. Greater detail should be spent on the filtering process of the image to identify the sharp edges of the heliostat in order to calculate the centre of the heliostat with pixel accuracy by using blob detection. Other methods can also be used to establish the centre of the mirror such as incorporating the corners of the mirror to draw a cross.

It should be noted that the centre of the concavity would only be in centre of the mirror if the concavity of the mirror is ideal. Further investigation should look at the effect of defects within the mirror towards the accuracy of the result compared to perfectly concave shaped mirrors. During simulation it was also assumed that the mirrors were perfectly concave because if a defective mirror was identified it would have been replaced. This is also an added function of the drone to be able to identify non-ideal concave mirrors. Therefor the assumption that the centre of the mirror is the centre of concavity was a reasonable assumption.

Using this knowledge, the properties of a concave mirror were then researched in Chapter 4.2.2.1. The properties of a heliostat's concave mirror showed that there was a specific minimum required distance that the camera should be away from the mirror in order to identify the complete target in the reflection

for each heliostat. This distance was dependent on the distance that the heliostat was away from the target, as well as its concavity. When this distance was established, it was also shown that by using computer vision, it was possible to establish where the weighted centre of the target was.

The weighted centre of the target should correspond with the centre of the mirror for the drone position to be seen as a calibration point. During simulation it was assumed that such a calibration point obtained without error. However further studies incorporating deflectometry could improve the targets shape to better identify such a centre. It is also possible to confirm the accuracy of selecting such a calibration point with the help of a deflectometry analysis.

Accuracy of the drone's position also had to be confirmed with the accuracy achieved by the RTK-GPS in Chapter 3.3. As such, a static test was implemented to show the uncertainty of the RTK-GPS and to confirm that the performance of the positional accuracy was within 30.5 millimetres from the mean. The data collected also showed the properties of a normally distributed data set.

The calibration equation was fine-tuned to fit the physical model of a heliostat in the laboratory by using 9 variables to describe the heliostat, and 1 variable to describe the drone offset. All 9 calibration parameters are described in Chapter 4.3.2. From there the selected parameters were incorporated into the calibration equation. A simulation tested the theoretical performance of a drone calibrating various heliostats.

It was concluded that the performance of the calibration depended on the specific noise of each selected drone point. It was further noted that calibration using a drone required at least 10 points, and that using fewer points caused erratic and unpredictable behaviour. This is due to the 10 variable equation that was set up requiring 10 data points to solve all the variables.

A final analysis in Chapter 6.6 also shows that the calibration performance is dependent on the distance that the drone is away from the heliostat during calibration, because of the radius-to-noise error of the drone.

Several issues came up during the writing of this thesis that will require further investigation in order to recommend improvements. One of these is the target that is identified within the reflection. The target is rectangular and therefore when an image is taken of the reflection, it would have 4 sharp edges. Thus, when a quadratic equation is applied to the data obtained from the image, it is less accurate, because the data does not have a circular pattern. If the pattern is changed to a circular pattern, then a quadratic fit would perform

better, although distortions would still be present in the shape of the reflection. However, a weighted minimum of the resulting reflection should still be taken.

Another improvement that could be considered is that during the filtering of the aerial view of the heliostat field, the corners of the heliostats are not rounded, but kept as sharp edges for a more accurate identification of the centre of the heliostat mirror.

During the calibration process it is possible for the optimization algorithm to fall into a local minimum solution. The selected 100 iterations take time to be calculated, although it only takes a few seconds using parallel computing. Using a super computer to generate thousands of solutions could be considered, and this would be able to identify a trend in the selection of the starting point of the first iteration of the problem by means of the deep learning process.

Theoretically combining all the sensors on the drone with the RTK-GPS could result in higher positional accuracy, and therefore it could improve the milliradian error.

List of References

Andreas, N., Linus, N., Joschka, T. and Patrick, P. (2013). Detecting deformations of heliostat surfaces using deflectometry with drones. *RWTH-AACHEN University*.

Central Tower Technology (2018). Torresol energy. [Online]. Available: `http://torresolenergy.com/en/gemasolar/`. [2018, August 18].

Constrained Nonlinear Optimization Algorithms (2018). [Online]. Available: `https://www.mathworks.com/help/optim/ug/constrained-nonlinear-optimization-algorithms.html#brnpd5f`. [2018, August 18].

CSP Summary Charts (2018). [Online]. Available: `http://www.irena.org/costs/Charts/CSP`. [2018, August 18].

Floreano, D. and Wood, R.J. (2015). Science, technology and the future of small autonomous drones. *Nature*, vol. 521, no. 7553, p. 460.

FLT (2018). [Online]. Available: `http://www.soltigua.com/flt-introducion/#`. [2018, August 18].

Gheorghiţă, D., Vîntu, I., Mirea, L. and Brăescu, C. (2015). Quadcopter control system. In: *System Theory, Control and Computing (ICSTCC), 2015 19th International Conference on*, pp. 421–426. IEEE.

Kendall, P.C. (2017). *Vector analysis and Cartesian tensors*. Routledge.

Llamas, D. (2018). The first concentrating solar power project to be built in canada. [Online]. Available: `http://helioscsp.com/the-first-concentrating-solar-power-project-to-be-built-in-canada/`. [2018, August 18].

Maricopa solar (2018). [Online]. Available: `http://www.mortenson.com/solar/projects/maricopa-solar`. [2018, August 18].

McCollum, B.T. (2017). Analyzing gps accuracy through the implementation of low-cost cots real-time kinematic gps receivers in unmanned aerial systems. Tech. Rep., Air Force Institute of Technology Wright-Patterson AFB United States.

Monterreal, R. (2013). Calibration and analysis of heliostats. [Online]. Available: `http://sfera.sollab.eu/downloads/Schools/Calibration_of_Heliostats_Rafael_Monterreal_SFERA2013.pdf`. [2018, August 18].

Newman, N. (2016). Journalism, media and technology predictions 2016. *Digital News Project*.

Pardell, R. (2017). Agcfds: Automated glass cleaning flying drone system. US Patent App. 15/301,516.

Ravelli, S., Franchini, G. and Perdichizzi, A. (2018). Comparison of different csp technologies for combined power and cooling production. *Renewable Energy*, vol. 121, pp. 712 – 721. ISSN 0960-1481. [Online]. Available: `http://www.sciencedirect.com/science/article/pii/S0960148118300843`. [2018, August 18].

Real-Time Kinematic (RTK) (2018). [Online]. Available: `https://www.novatel.com/an-introduction-to-gnss/chapter-5-resolving-errors/real-time-kinematic-rtk/`. [2018, August 18].

Reda, I. and Andreas, A. (2004). Solar position algorithm for solar radiation applications. *Solar energy*, vol. 76, no. 5, pp. 577–589.

Richter, P., Frank, M. and Abrahám, E. (2014). Multi-objective optimization of solar tower power plants. In: *ECMI Conference Proceedings*.

Rizvi, A.A., Addoweesh, K., El-Leathy, A. and Al-Ansary, H. (2014). Sun position algorithm for sun tracking applications. In: *Industrial Electronics Society, IECON 2014-40th Annual Conference of the IEEE*, pp. 5595–5598. IEEE.

Sebold, J. and Lacerda, L. (2016). A numerical method for coupled differential equations systems. *Journal of The Electrochemical Society*, vol. 163, no. 13, pp. E344–E350.

Singh, T., Hussien, M.A.A., Al-Ansari, T., Saoud, K. and McKay, G. (2018). Critical review of solar thermal resources in gcc and application of nanofluids for development of efficient and cost effective csp technologies. *Renewable and Sustainable Energy Reviews*, vol. 91, pp. 708 – 719. ISSN 1364-0321. [Online]. Available: `http://www.sciencedirect.com/science/article/pii/S1364032118301515`. [2018, August 18].

Sonka, M., Hlavac, V. and Boyle, R. (2014). *Image processing, analysis, and machine vision*. Cengage Learning.

Sun, F., Guo, M., Wang, Z., Liang, W., Xu, Z., Yang, Y. and Yu, Q. (2015). Study on the heliostat tracking correction strategies based on an error-correction model. *Solar Energy*, vol. 111, pp. 252–263.

t-Table (2018). [Online]. Available: `http://www.sjsu.edu/faculty/gerstman/StatPrimer/t-table.pdf` [2018, August 18].

Zavodny, M., Slack, M., Huibregtse, R. and Sonn, A. (2015). Tower-based csp artificial light calibration system. *Energy Procedia*, vol. 69, pp. 1488–1497.